Scholars' Mine

Doctoral Dissertations

Student Theses and Dissertations

Summer 2017

Dirac surface states of magnetic topological insulators

Seng Huat Lee

Recommended Citation

DIRAC SURFACE STATES OF MAGNETIC TOPOLOGICAL INSULATORS

by

SENG HUAT LEE

A DISSERTATION

Presented to the Faculty of the Graduate School of the

MISSOURI UNIVERSITY OF SCIENCE AND TECHNOLOGY

In Partial Fulfillment of the Requirements for the Degree

DOCTOR OF PHILOSOPHY

in

PHYSICS

2017

Approved

Dr. Yew San Hor, Advisor
Dr. George D. Waddill
Dr. Julia E. Medvedeva
Dr. Cihan Kurter
Dr. Manashi Nath

PUBLICATION DISSERTATION OPTION

This dissertation consists of the following articles:

Paper I, Pages 42-59, will be submitted to Physical Review B with the title of *Dirac Surface State of the Antiferromagnetic Topological Insulator $Fe_xBi_2Se_3$*, with Julie E. Medvedeva and Yew San Hor.

Paper II, Pages 60-74, will be submitted to Journal of Applied Physics with the title of *Multilayered Quantum Hall Effect in Paramagnetic Ordered Topological Insulator $Mn_xBi_2Se_3$*, with Stephen Kraus and Yew San Hor.

Paper III, Pages 75-99, has been published in arXiv: 1512.03519 with the title of *Time-Reversal Symmetry Breaking Superconductivity in Topological Materials*, with Yunsheng Qiu, Kyle Nocona Sanders, Julie E. Medvedeva, Thomas Vojta and Yew San Hor.

Paper IV, Pages 100-110, will be submitted to npj Quantum Materials with the title of *Electric-Field Exfoliation of Layered Crystalline Materials*, with Alexander Mark, Julie E. Medvedeva, Eric W. Bohannan and Yew San Hor.

ABSTRACT

Magnetic topological insulator (TI) has been theoretically proposed to be a platform for inducing magnetic monopole and exhibit fascinating quantum phenomena, whereas topological superconductor can host Majorana fermions, particles that are their own antiparticles, which can be manipulated for topological quantum computing. In this dissertation, we experimentally demonstrated that by intercalation of different transition metals in the van der Waals gaps of Bi_2Se_3 TI, magnetism and even superconductivity can be induced. In $Fe_xBi_2Se_3$, antiferromagnetism is induced with a transition temperature at ~ 100 K. Coexistence of the Dirac surface state with magnetism in antiferromagnetic TI that has been predicted by the theoretical study is verified. We also found the Dirac fermions originate from the bulk acting as many parallel 2D conduction channels on the material. In $Mn_xBi_2Se_3$, paramagnetism is induced. From Shubnikov-de Haas oscillations and quantum Hall effect (QHE) observation, we found the existence of Dirac fermions originate from the bulk, which is similar to the case of $Fe_xBi_2Se_3$. Due to the origin of the QHE in $Fe_xBi_2Se_3$ and $Mn_xBi_2Se_3$ systems is from the bulk acting as many 2D conduction channels, the electric-field exfoliation method is invented. This method is capable of obtaining a clean sample from different layered crystalline materials with the thicknesses in the range of nm and expecting to observe QHE from the surface state on both materials. Superconductivity is also induced in $Nb_xBi_2Se_3$ with a critical temperature of $T_c = 3.2$ K while the Dirac surface dispersion in its normal state is still preserved. The onset of hysteretic magnetization in $Nb_xBi_2Se_3$ below T_c suggests spontaneous time-reversal symmetry breaking in the superconducting state. Superconducting and magnetism mutually assist each other to give rise to a symbiosis state of this two phases.

ACKNOWLEDGMENTS

TABLE OF CONTENTS

LIST OF ILLUSTRATIONS

PAPER II

PAPER III

PAPER IV

1. INTRODUCTION

Human civilization has long been associated with the materials, both natural and synthesized, used in the creation of structures and devices. From the names of the three ages of human prehistory — stone, bronzed, and iron — there is clear indication that the adoption of these materials coincided with the revolutions in society and allowed for mankind to accomplish greater feats of science and engineering. Moving from the Stone Age to today, the age of silicon, materials continue to influence human history, and therefore the drive to invent new substances has remained.

Over the past decade, the growth of condensed matter physics has often been driven by the discoveries of novel quantum materials [1,2]. In particular, one of the quantum materials that has been discovered is called topological insulator [3–9]. Topological insulators (TIs) are characterized by their property of gapless Dirac-like conducting surface states protected by time-reversal symmetry (TRS) and gapped insulating bulk states owing to strong spin-orbit coupling (SOC). Thus, TIs have high-conducting surface states but insulate in bulk [see Fig. 1.1 (c), (f)] [10–12]. These properties suppress backscattering on the surface and have dissipationless spin-polarized current upon the surface. Furthermore, the linear dispersions on the spin-polarized surface state lead the relativistic Dirac fermions to become relevant. From an experimental perspective, this surface state has been directly revealed by angle-resolved photoemission spectroscopy (ARPES) and scanning tunneling microscopy (STM) [12–16].

These behaviors are predicted to vary with the introduction of magnetic impurities into the TIs. For example, magnetically doped topological insulators can break the TRS and make the Fermi level tunable, leading to the opening of a measurable band gap in these

surface states as well as the formation of unique quantum properties. The tunable Fermi level further allows us to control the surface electric transport [17–23]. Therefore, the properties of the magnetically doped topological insulators promise unique quantum phenomena such as the emergence of imaged magnetic monopole induced by a point charge, magnetoelectric effects, anomalous magnetoresistance, and the quantum anomalous Hall effect (QAHE) [17–25]. The latter phenomenon has been experimentally realized due to the massive surface states induced by the broken TRS. These properties of the chemically doped topological insulators are promising and are receiving much attention not only in condensed-matter physics, but also from high-energy physics [26,27].

Indeed, there are currently many experimental challenges in magnetic TI systems that need to be overcomed to unveil the properties of the surface states fully. Various magnetically doped TIs have been discovered by doping with the $3d$-transition metal element, such as Mn doped Bi_2Te_3 [28] and (Fe, Mn, Cr) doped Bi_2Se_3 [17,18,24,25]. However, the magnetic orders are still controversial, and the effective magnetic doping of TIs is still a challenge for the experimentalist. For example, magnetic phase transitions, if present, were only observed at very low temperature. Magnetic TIs with a transition temperature near room temperature may present the most efficient path to manufacture dissipationless spintronic devices. To date, high transition temperature magnetic TIs have not been discovered in the vast majority of experiments. Other challenges that need to be solved include the high density of defects in grown TI crystals and overwhelmingly dominant conduction from the bulk [29].

1.1. TWO-DIMENSIONAL TOPOLOGICAL INSULATORS

1.1.1. Quantum Hall Effect. Beginning from the 1980s, the first observation of the quantum Hall effect was reported in two-dimensional electron gases under strong magnetic fields at very low temperatures [30]. In those experiments, an energy gap was formed due to the electrons following the quantized closed circular cyclotron orbits, also known as Landau quantization, and caused the inside of the quantum Hall system to act as an insulator. The charges, however, are allowed to flow on edge states in one direction, exhibiting a quantized conductance that is characteristic of one-dimensional transport, as shown in Fig. 1.1 (a). Since a single direction of propagation is present on edge states, the quantum Hall edge channels were found to be chiral with the chirality determined by the applied magnetic field direction. Due to the inability of a charge carrier to reverse its direction of motion, backscattering is suppressed on edge states. The charge carriers in the edge states are not only resistant to the scattering event, but can also be transported without energy dissipation. Von Klitzing *et al.* discovered that the Hall conductance σ_{xy} was not directly proportional to the applied magnetic field B as predicted in the ordinary Hall experiment, but exhibits a staircase sequence of wide plateaus at quantized values. Mathematically, the quantum Hall conductance can be expressed as

$$\sigma_{xy} = \nu \frac{e^2}{h}$$

(1.1)

where ν is an integer, e is the electron charge, and h is Planck's constant. From equation (1.1), the Hall conductance is an integer multiplied by a fundamental constant of nature $e^2/h = 1/25812.80759$ regardless of the dimension or the imperfections of the

system. This can be understood by the works of Thouless, Kohmoto, Nightingale and den Nijs (TKNN), which show the link of Hall conductivity to the topology of Bloch wave functions [31]. Although the QHE demonstrates prominent edge states, as shown in Fig. 1.1 (d), it can only be observed under a strong external magnetic field that breaks the TRS.
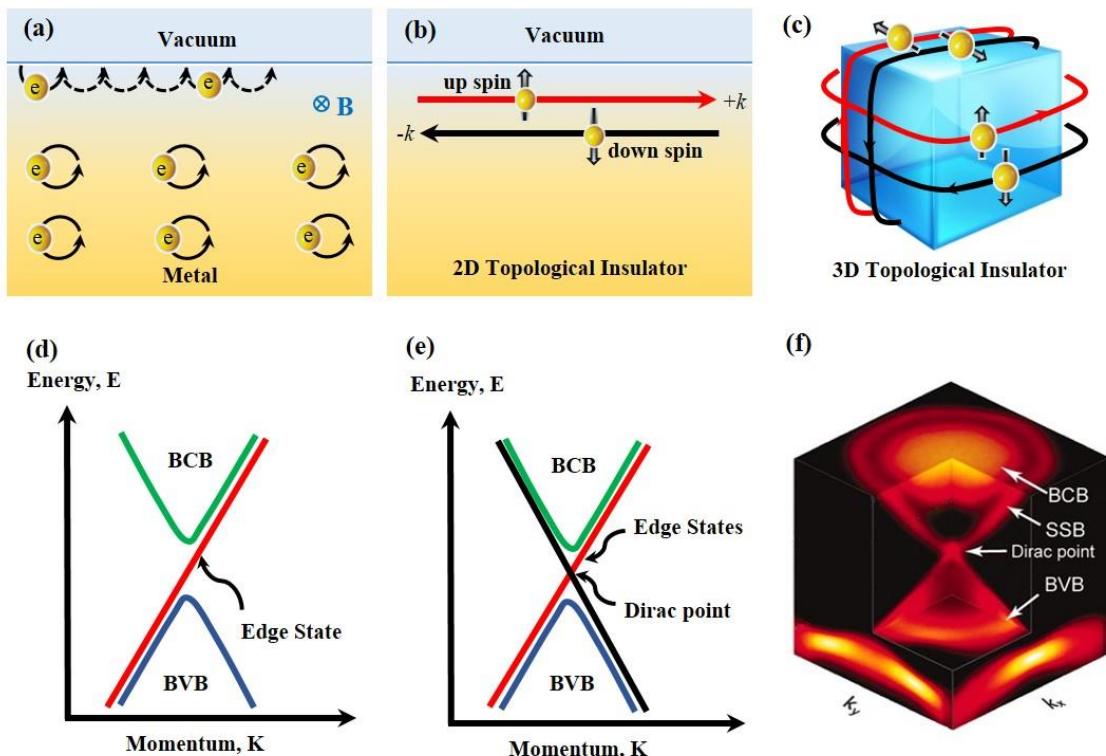
Fig. 1.1. Edge and surface states in quantum Hall and TI systems. (a) In QHE, electrons conduct along the edge state in one direction due to the interruption of the electrons circular motion by the boundary in a magnetic field. (b), (c) Schematic of the edge states and surface states for 2D and 3D TIs system, respectively. (d), (e), (f) Energy dispersion for quantum Hall system, 2D TI system, and 3D TI system. BCB and BVB represent the bulk conduction band and bulk valance band, respectively. SSB is the surface state band. Fig. (f) is adopted from ref. [18].

1.1.1.1 The TKNN Invariant. Quantum Hall effect is topologically robust. The edge state especially is robust against impurities inside the insulating bulk. To explain why the quantum Hall effect is topologically robust, Laughlin [32] proposed a topological treatment based on the principle of gauge invariant, and later TKNN related the physical response of the Hall conductance to a topological invariant in momentum space. The invariant was then used to rewrite the quantized Hall conductance expression in terms of the bulk states.

In an electron in a periodic potential, the eigenfunctions that satisfy the Schrödinger equation $H\psi_{kn}(r) = E_{kn}\psi_{kn}(r)$ are the product of a plane wave and a periodic Bloch function, $u_{kn}(r)$. The eigenfunctions can be expressed as $\psi_{kn}(r) = e^{ik\cdot r}u_{kn}(r)$ where n is band index and $\boldsymbol{k}$ is the wave vector. The expression $u_{kn}(r)$ has the same periodicity as the lattice. By using the Kubo formula, TKNN showed that the Hall conductivity for the two-dimensional electron gas system can be written in terms of the Bloch wave functions and gives

$$\upsilon = \frac{i}{2\pi}\sum\oint_{BZ} d^2\boldsymbol{k}\left(\frac{\partial u^*}{\partial k_x}\frac{\partial u}{\partial k_y} - \frac{\partial u^*}{\partial k_y}\frac{\partial u}{\partial k_x}\right) = \frac{h}{e^2}\sigma_{xy} \qquad (1.2)$$

where the sum is over the occupied electron bands and the integral is performed over the entire Brillouin zone. The periodicity of the Brillouin zone makes it topologically a torus. From equation (1.2), υ only depends on the Bloch wave functions and the integral always evaluates to an integer over the Brillouin zone. Therefore, υ must be an integer provided that no partially filled band exits [33].

1.1.1.2 Berry's Phase and Chern Invariant. To show that v must be an integer,
Berry's phase of the Bloch wave functions needs to be introduced [34]. Generally, the
Berry connection $\mathcal{A}$ for the mth band is defined as

$$\mathcal{A}_m(\boldsymbol{k}) = i\langle u_m|\nabla_{\boldsymbol{k}}|u_m\rangle \tag{1.3}$$

where $\mathcal{A}_m$ is a vector defined in terms of the Bloch wave functions. When $\boldsymbol{k}$ moves on a
closed loop γ, the Berry phase ϕ is then the connection integrated over some loop γ and
can be written as

$$\phi = \oint_\gamma \mathcal{A} \cdot d\boldsymbol{k} \tag{1.4}$$

A closed surface in the Brillouin zone is a torus due to the periodicity in $\boldsymbol{k}$-space. Another
important quantity that may be expressed as a surface integral of the Berry curvature is

$$\mathcal{F}(\boldsymbol{k}) = \nabla_{\boldsymbol{k}} \times \mathcal{A}(\boldsymbol{k}) \tag{1.5}$$

By substituting the equation of (1.3) and (1.5) to (1.2), v can be simplified as

$$v = \frac{1}{2\pi}\oint_{BZ}d^2\boldsymbol{k}\,\mathcal{F} \tag{1.6}$$

and it is satisfied for any continuous states defined in the Brillouin zone. Because of the
single-valued nature of the wave function, v is an integer. From equation (1.6), it is clearly

observed that the Berry flux $2\pi\upsilon = \iint \mathcal{F}d^2\boldsymbol{k}$ for the entire Brillouin zone must be an integer multiple of 2π. This argument was first demonstrated by the TKNN without mathematical work, which was performed by Chern a year later. The integer υ in QHE is then known as the TKNN invariant [31] or Chern number [35]. The Chern number is a topological invariant provided that the Hamiltonian varies smoothly. Therefore, Hall conductance is a measure of total curvature in momentum space, and hence its value is insensitive to details of the samples such as size and geometry.

1.1.2. Quantum Spin Hall Effect. In contrast to quantum Hall systems, there is also a new concept of the quantum spin Hall effect (QSHE) that preserves the TRS and is an analogue of the QHE [36–38]. In QSHE, electrons with spin-up and spin-down propagate in opposite directions to form spin-polarized currents on the edge states due to the SOC, as illustrated in Fig. 1.1. (b). The spin-polarized currents are unaffected by the presence of the disorders and have gapless edge modes by the bulk-boundary correspondence, as shown in Fig. 1.1 (e). Originally, graphene was suggested to be the system that was capable of realizing the quantum spin Hall effect, but the weakness of the SOC of carbon prevented this [37].

To have a strong SOC, heavy elements are needed to realize the 2D TIs since the spin-orbit is a relativistic effect. In 2006, Bernevig *et al.* suggests an experiment that enables one to observe the quantum spin Hall effect: a thin layer of a strong SOC semiconductor material of HgTe sandwiched between two CdTe barriers to form two-dimensional quantum well structures that offer a unique way to tune the electronic structure of the material [39]. Soon after, this prediction was confirmed by an experiment

that successfully observed the quantized conductance of $2e^2/h$ in zero magnetic fields, 30 mK [40]. Therefore, an HgTe quantum well is regarded as the first 2D topological insulator.

Although the quantum spin Hall effect of HgTe was observed, the progress of experimental studies on these two-dimensional TIs is proceeding relatively slow. This is due to the very small bulk band gap, about 10 meV, causing the TI phase detection to be possible only at very low temperatures [41].

1.2. THREE-DIMENSIONAL TOPOLOGICAL INSULATORS

In 2006, theorists predicted that the topology in two-dimensional systems can be extended to three-dimensional systems, provided that the system has a strong SOC that usually presents in heavy elements [3,42,43]. The term *topological insulators* was coined by Moore to describe this type of material [42]. Fu *et al.* predicts that $Bi_{1-x}Sb_x$ is a 3D TI based on the study of the connection between the bulk topological order and the presence of unique conducting surface states [44]. Two years after, Hsieh *et al.* claims the experimental discovery of the first 3D TI by studying the energy dispersion of surface states from the angle-resolved photoemission spectroscopy (ARPES) [45].

Shortly after, the compounds of Bi_2Se_3, Bi_2Te_3, and Sb_2Te_3 were theoretically predicted and experimentally verified as a family of TIs [44,46–48]. Those crystals have the same rhombohedral layered crystal structure with quintuple layers (QL) ordered in an A–B–A–B–A sequence along the *c*-axis. The QLs weakly interact through the van der Waals forces, and therefore those materials cleave easily between QLs. Experimentally, the growth of those materials as single crystals can be achieved by employing the modified Bridgman method. The detail of the TIs crystal growth is presented in Section 3.2. Most of

the experimental studies are based on Bi_2Se_3 because it has a single Dirac surface state with a large energy bulk bandgap of 300 meV, helical spin texture, and no other surface bands. The only problem of this material is the chemistry defection caused by the charged selenium vacancies that act as electron donors, resulting in high *n*-type bulk carrier density [29]. Numerous suggestions were proposed to manipulate these surface states near the Dirac point [4,27] by electrostatic gating or chemical doping. Chemical doping, either by magnetic or non-magnetic dopants, of TIs is one direct approach to tune the Fermi level to the Dirac point [15,18].

1.2.1. Magnetic Topological Insulators. As mentioned earlier, the unusual electromagnetic and magnetotransport effects can be observed in magnetically doped TIs due to the broken TRS. The prominent challenge to realize those novel quantum phenomena is to maintain the strong SOC when the TRS in TIs materials is broken by introducing magnetic dopants. Various TIs that are magnetically doped with $3d$-transition metal elements have been studied theoretically and experimentally [17,18,24,25,49,50]. From the experimental perspective, only Mn bulk-doped Bi_2Te_3 [28] clearly demonstrated the ferromagnetic phase transition at 12K for doping concentration up to 9%. For Bi_2Se_3, Fe doping and Mn doping do not induce the ferromagnetic ordering, but a small surface state gap opened at the Dirac point from the ARPES measurement [18].

A few years later, the QAHE with the quantized conductivity of e^2/h from the Cr and V-doped $(Bi_{0.1}Sb_{0.9})_{1.85}Te_3$ thin film at 30 mK was reported [22,51,52]. Unfortunately, the quantization of Hall conductance can only be achieved at very low temperatures because the topologically nontrivial band gap is extremely small [53–55]. Therefore, it is

essential to synthesize magnetic topological insulators with a large nontrivial band gap for technological applications.

1.2.2. Topological Superconductor. The relativistic dispersion or the Dirac-like behavior of these surface states of TI makes these types of materials excellent platforms in search for exotic particles and phenomena from high-energy physics and astrophysics that can be verified in condensed matter systems. For example, inducing superconductivity in TIs through proximity or other effects can generate Majorana fermions, particles that are their own antiparticles [27,56,57]. Pairs of such particles can be used as building blocks of a fault-tolerant topological quantum computer.

Recent research has focused on unconventional superconductivity that can coexist with spin magnetism. Even in non-TI materials, the presence of both superconductivity and magnetic order may induce rare types of order such as p-wave symmetry or chiral structure to the Cooper pairs. However, only a few promising topological superconductor systems have been observed, such as the recently discovered Cu-intercalated Bi_2Se_3 [58]. There are also only few magnetic doped TI systems available. It may be possible to spontaneously generate the non-abelian Majorana particles in the vortex cores of the material through spontaneous TRS breaking within a superconducting TI. To date, however, there has been no signature of such TRS breaking in $Cu_xBi_2Se_3$ or any other similar superconducting TI. The finding of TIs with coexisting superconductivity and magnetism is of extreme importance and has a long-term impact on the fundamental physics community as well as future applications on quantum computing and spintronic devices.

2. EXPERIMENTAL REVIEW OF 3D TOPOLOGICAL INSULATORS

This chapter will explore the analysis and techniques that are useful in determining the properties of the surface states as well as the observation of unique quantum phenomena such as Shubnikov-de Haas oscillations.

2.1. ANGLE-RESOLVED PHOTOEMISSION SPECTROSCOPY

Three-dimensional TIs can be directly identified by the observation of Dirac cone from the ARPES data [45]. Fig. 2.1 shows the experimental setup of ARPES measurements and its result. In ARPES experiments, a high energy photon is used to eject an electron from a crystal and the surface or bulk electronic structure is determined from the momentum analysis of the emitted electron. Usually the ARPES experiment is conducted in an ultrahigh vacuum environment and the incident photon beam often comes from a synchrotron source, which allows for a tunable monochromatic source with high intensity. Since surface states do not disperse along the direction perpendicular to the surface, isolation of surface states from that of the bulk electronic band structure can be clearly observed. Spin-resolved ARPES can further measure the distribution of spin orientations on the Fermi surface, which can be used to determine the Berry's phase on the surface.

Fig. 2.1 (c) shows the ARPES data on Bi_2Se_3 TI, which can be interpreted as an energy map of the occupied electronic states as a function of momentum along the $K - \Gamma - K$ direction. The gap between the bulk conduction band (BCB) and the bulk valance band (BVB) is 190 meV. While the Dirac point is located at 340 meV below the Fermi level, it connects the upper and lower Dirac cones. The nearly linear Dirac-like dispersion is clearly observed. For magnetic TIs, a gap is expected in-between the Dirac cones of surface states.
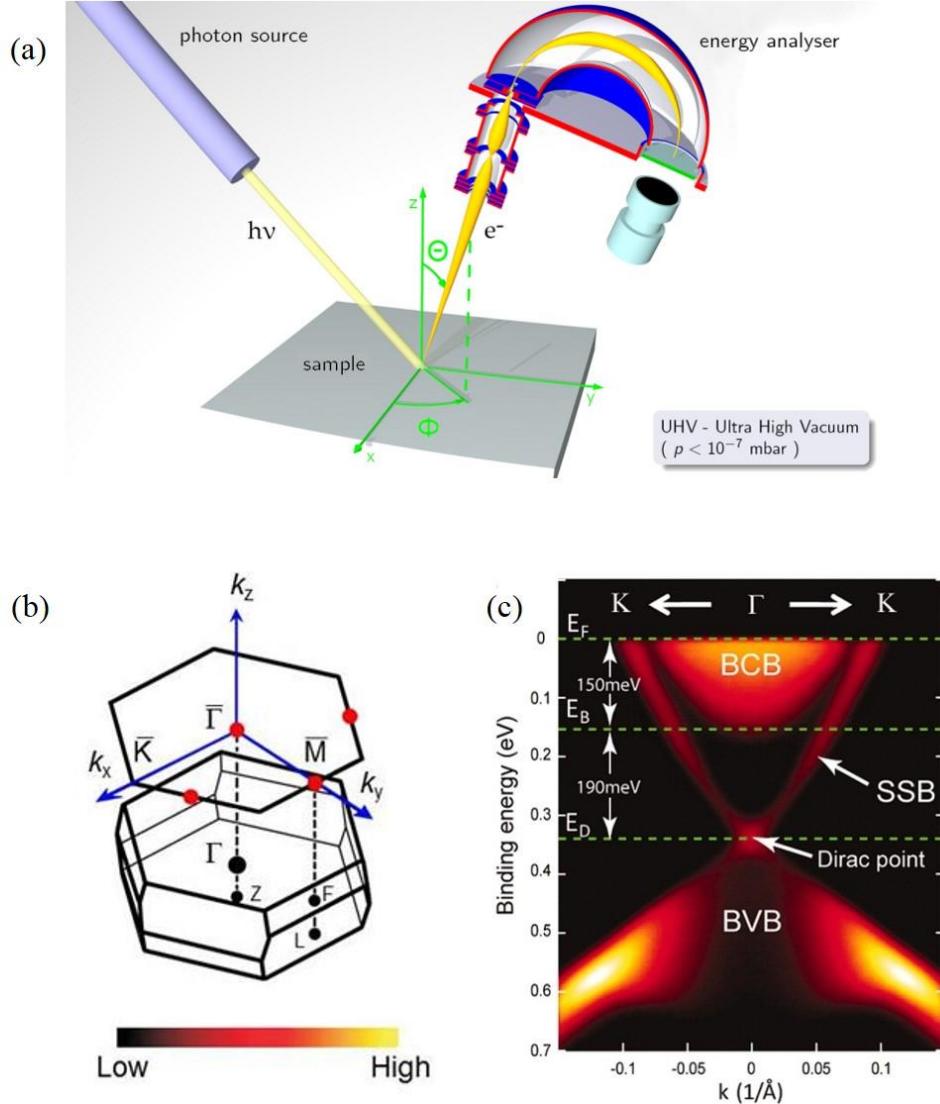
Fig. 2.1. Angle-resolved photoemission spectroscopy (ARPES). (a) A schematic of ARPES experimental setup used to measure the surface and bulk electronic structures of the sample. (b) Three-dimensional bulk Brillouin zone of Bi_2Se_3 TI with the hexagonal surface Brillouin zone, space group $R\bar{3}m$, (c) ARPES data for Bi_2Se_3 TI. EF, EB, and ED represent the Fermi energy, energy at the bottom of the bulk conduction band (BCB), and the energy at Dirac point, respectively. BVB is the bulk valance band, while SSB is the surface state band. Fig. (a) and (c) are adopted from Wikipedia and ref. [18], respectively.

Not all materials are suitable for ARPES studies because they require a clean and flat surface that is usually obtained by cleaving single crystals. ARPES measurement becomes difficult when single crystals are not available. In this case, quantum transport experiments will be another option to confirm the existence of the surface transport provided that the bulk is sufficiently insulating. Carriers with high mobility on their surface are known as Dirac fermions. Those Dirac fermions can be revealed by elucidating the π Berry's phase in the quantum oscillations of longitudinal magnetoresistance measurement from the surface state.

2.2. SHUBNIKOV–DE HAAS OSCILLATIONS

Shubnikov–de Haas oscillation (SdHO) is a quantum oscillation occurring in the longitudinal magnetoresistance measurement at low temperatures with the presence of intense external magnetic fields [59]. The energy levels of free electrons are quantized into bands under a strong magnetic field. That quantized energy level is called the Landau level. The energy gap in-between the Landau levels is separated by the cyclotron energy $\hbar\omega_c$ in a function of the applied magnetic field. The energy of Landau levels can be expressed as

$$E_\upsilon = (N + \tfrac{1}{2})\hbar\omega_c \qquad (2.1)$$

where N is the Landau level and $\hbar$ is Planck's constant, and $\omega_c = eB/m^*$ is cyclotron frequency, where B is applied magnetic field and m^* is the effective mass. The half-integer in equation (2.1) represents the Dirac case where the conduction band and the valence band each contribute half of the states that make up the $N = 0$ Landau level. The Landau levels

can also be presented in an energy map as a function of the density of states (DOS) as presented in Fig. 2.2. When the Landau level passes over the Fermi surface as a result of an increasing applied magnetic field, electrons are depopulated as free electrons. No electron is depopulated if the Fermi energy is in-between two Landau levels, and therefore peak resistance is observed. The resistance changes periodically as the magnetic field is increased, which leads to the observed oscillations in the longitudinal resistance. In practice, the SdHO can only be analyzed after the polynomial background of the resistance signal is subtracted from the magnetoresistance measurement.
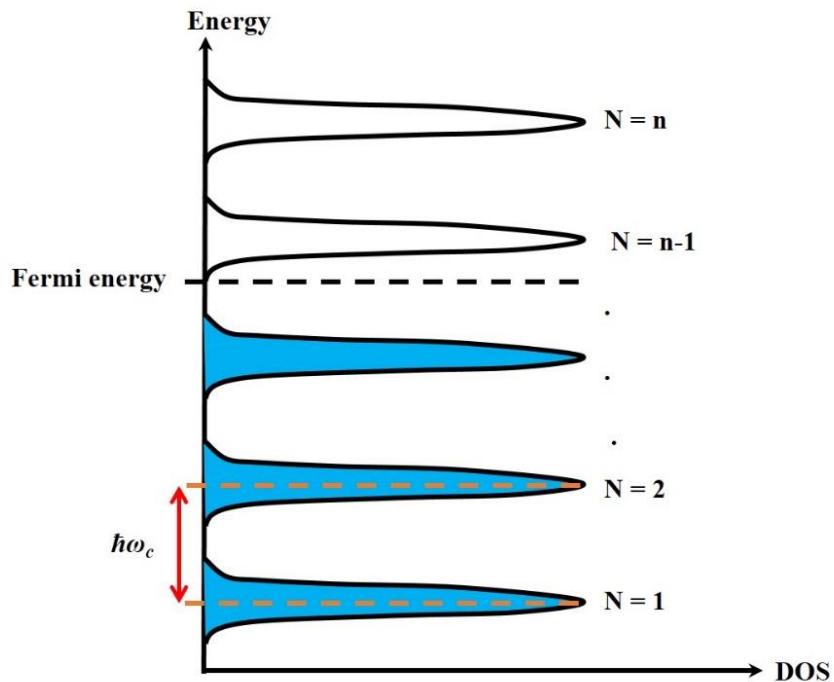
Fig. 2.2. Formation of Landau levels under the influence of external magnetic field as a function of DOS. Landau levels are separated by $\hbar\omega_c$. Since ω_c is directly proportional to B, the energy gap in-between Landau levels increases as B increases. Landau levels below the Fermi level are filled with electrons.

Observation of the SdHO in 3D TIs is particularly important to study the 2D Fermi surface state that coexists with the 3D bulk state. It is also often used to determine the effective mass of charge carriers, Dingle temperature, carrier lifetime, and quantum mobility [59]. Moreover, the phase shift factor of the SdHO directly reflects the existence of Berry's phase and confirms the quantum transport of surface Dirac fermions in TIs.

From the Onsager relation [59], the frequency of the SdHO, B_F, is directly proportional to the Fermi wave vector $\boldsymbol{k}_F$ as

$$B_{\mathrm{F}} = \left(\frac{\hbar}{2\pi e}\right)\pi\boldsymbol{k}_{\mathrm{F}}^2 \qquad (2.2)$$

for a circular external cross section of Fermi surface perpendicular to the magnetic field. B_F can be obtained from the Fourier analysis of the background-subtracted oscillations signal. Based on the Onsager relation, the Fermi wave vector $\boldsymbol{k}_F$ can be calculated and should be consistent with the energy dispersion from the ARPES measurement. Due to the circular shape of the Fermi surface, the 2D carrier density, given as $n_{2D} = eB_F/h$ per spin, can also be extracted directly from B_F. By using the B_F/B, where B is the magnetic field position of each ΔR_{xx} minimum, an integer is obtained. This integer corresponds to the Landau levels index N.

The 2D nature of the SdHO should vary periodically with $1/B$ and depend only on the perpendicular component of the magnetic field $B_\perp = B\cos\theta$, where the angle in-between the magnetic field and the c-axis is defined as the tilt angle θ [60–65]. Therefore, the plot of the magnetic field position for particular Landau levels, B_N, is well fitted by the function of $1/\cos\theta$ if the quantum oscillator exhibits 2D properties of the

SdHO. If the SdHO is due to 3D bulk state, the oscillations do not depend on $B_\perp$ and an oscillation can be observed at all angles. In fact, the observation of the SdHO does not necessarily originate from the surface state transport carriers. It can be due to the bulk of the sample acting as many parallel 2D conduction channels [66]. Therefore, it is important to determine the contributions of carriers in the TI that could give 2D transport features, especially for samples with a high bulk carrier density. One way to identify this is by performing the quantum Hall effect (QHE) measurement. The origin of the SdHO is from the bulk if the step size between adjacent quantized plateaus scales with the thickness of the sample.

Many properties such as the effective mass of the carrier, Dingle temperature, quantum lifetime, and quantum mobility can be determined from the standard Lifshitz-Kosevich analysis by performing a temperature-dependent SdHO measurement. From the Lifshitz-Kosevich formulation, the quantum oscillations can be expressed as

$$\Delta R_{xx}(T,B) = \frac{\frac{\alpha T}{\Delta E_N(B)}}{\sinh\left[\frac{\alpha T}{\Delta E_N(B)}\right]} e^{-\frac{\alpha T_D}{\Delta E_N(B)}} \cos\left[2\pi\left(\frac{B_F}{B} + \frac{1}{2} + \phi_B\right)\right] \qquad (2.3)$$

where ΔR_{xx} is the amplitude of the oscillation as a function of magnetic field and temperature, $\alpha = 2\pi^2 k_B$, k_B is the Boltzmann constant, $\Delta E_N = \hbar eB/m^*$ is the energy gap in-between Landau levels with m^* as the effective mass, T_D is the Dingle temperature and ϕ_B is the phase shift.

In a fixed magnetic field, only the first term of ΔR_{xx} has a temperature dependence with the fitting parameter ΔE_N. The exponential term does not make any contribution to

ΔR_{xx}. Therefore, the fitting parameter of ΔE_N can be extracted from the fitting of the temperature dependence of the oscillation amplitude, which in turn gives the effective mass of the electrons from the slope of ΔE_N versus the magnetic field. This can be explained by the cyclotron frequency, $\omega_c = eB/m^*$, and therefore $\Delta E_N = \hbar eB/m^*$.

In a constant temperature, the Dingle temperature can be determined from the magnetic field dependence of the SdHO amplitude. This method is known as Dingle analysis. Lifshitz-Kosevich formulation in equation (2.3) needs to be rearranged as shown in equation (2.4) to perform the Dingle analysis:

$$ln\left[\frac{\Delta R \hbar eB}{\alpha T m^*}\sinh(\frac{\alpha T}{\Delta E})\right] = -\frac{\alpha T_D m^*}{\hbar eB} + C \tag{2.4}$$

where C is a constant. The Dingle temperature T_D can be extracted from the slope of $ln\ D$ versus $1/B$ by defining D as $\Delta RB \sinh (\alpha T/\Delta E)$. Notice that the plot of $ln\ D$ versus $1/B$ will yield a straight line. The constant parameter of $\hbar e/\alpha T m^*$ in the logarithm function was ignored because the slope of $ln\ D$ versus $1/B$ is not affected by this constant. Once the effective mass of carrier m^* and Dingle temperature T_D are determined, one can calculate the quantum lifetime of the carrier $\tau = \hbar/2\pi k_B T_D$ and the quantum mobility $\mu_q = e\tau/m^*$.

Another important characteristic of TI materials that can be extracted from the observation of quantum oscillation is the Berry phase [34] that protects the surface states against the backscattering event from the presence of impurities inside the bulk. This Berry phase can take the value of zero for parabolic energy dispersion in ordinary metals, while π for linear energy dispersion possesses by the Dirac fermions [34,63,67]. In practice, the phase shift in the quantum oscillations can be determined from the Landau levels fan

diagram. The diagram is done by plotting the $1/B_N$ in the function of Landau level index N. This is strongly due to the phase of the oscillations, which is defined as

$$2\pi\left(\frac{B_F}{B_N} + \frac{1}{2} + \beta\right) = (2N + 1)\pi \tag{2.5}$$

where B_N is the magnetic field position corresponding to the Landau levels index N, and β is the phase shift. Therefore, a straight line is obtained for the plot of $1/B_N$ vs N with a slope of B_F. The phase shift β is determined from the N-axis intercept when a linear fit is extrapolated. The SdHO will be due to the Dirac fermions if $\beta = \frac{1}{2}$ [61,64,65,68,69].

Alternatively, the phase shift can be determined by the fitting method where the fitting equation is based on the modified Lifshitz-Kosevich formulation [65,70–72]

$$\Delta R_{xx} = A e^{-\frac{\pi}{\mu_q B}} \cos[2\pi(\frac{B_F}{B}) + \beta] \tag{2.6}$$

where the quantum mobility μ_q and phase shift β are the fitting parameters and A is a constant. From the fitted ΔR_{xx} with the experimental results, the phase shift can be determined. The Berry phase only exists if $\beta = \pi$.

2.3. QUANTUM ANOMALOUS HALL EFFECT

The Hall effect was first discovered in a non-magnetic conductor under a strong magnetic field [73]. The Hall voltage V_H is directly proportional to the applied magnetic field due to the deflection of the charge carrier by the Lorentz force. The setup of the Hall measurement is illustrated in Fig. 2.3 (a). Soon after in 1881, the Hall effect was also

discovered in ferromagnetic ordered materials without external fields. The measured Hall effect in the zero magnetic field originates from the spontaneous magnetization of ferromagnetic materials; this is called the anomalous Hall effect (AHE) [74,75]. Fig. 2.3 (b) illustrates the Hall resistance measurement for the ordinary Hall effect and the anomalous Hall effect. It is also observed that the quantized version of the Hall effect in two-dimensional electron gases under strong magnetic fields can cause the formation of Landau levels. The quantized Landau levels lead the appearance of dissipationless states at the edge of the two-dimensional electron system [76]. Since the discovery of the QHE, numerous theoretical concepts have been proposed to realize the QHE without the presence of the external magnetic field in ferromagnetic materials. This phenomenon is referred to as quantum anomalous Hall effect (QAHE) [77]. In QAHE, the magnitude of the Hall resistance at zero magnetic fields is exactly same as h/e^2, a fundamental constant of nature. The realization of QAHE is particularly important for the development of dissipationless spintronic devices.

QAHE has been predicted to occur in a magnetic topological insulator [4,78]. The introduction of magnetic impurities into the TIs system would open a gap at the Dirac point in the surface states induced by the broken TRS. This surface gap has been experimentally observed by ARPES. Moreover, the magnetic ordering also serves as its spontaneous magnetic moment and leads to the realization of QAHE. Previously, Mn doped on two-dimensional TI of HgTe quantum wells was predicted to be characterized by QAHE [78], but it still required external magnetic fields to align the Mn moments. In 2013, the first quantized Hall conductance at zero magnetic fields was observed in Cr doped $(Bi_{0.1}Sb_{0.9})_{1.85}Te_3$ thin film at the temperature of 30 mK [22]. New discoveries of magnetic

doped TIs exhibiting QAHE are strongly sought after. Nonetheless, tremendous interest

has been focused on understanding the nature of the quantum anomalous Hall state.
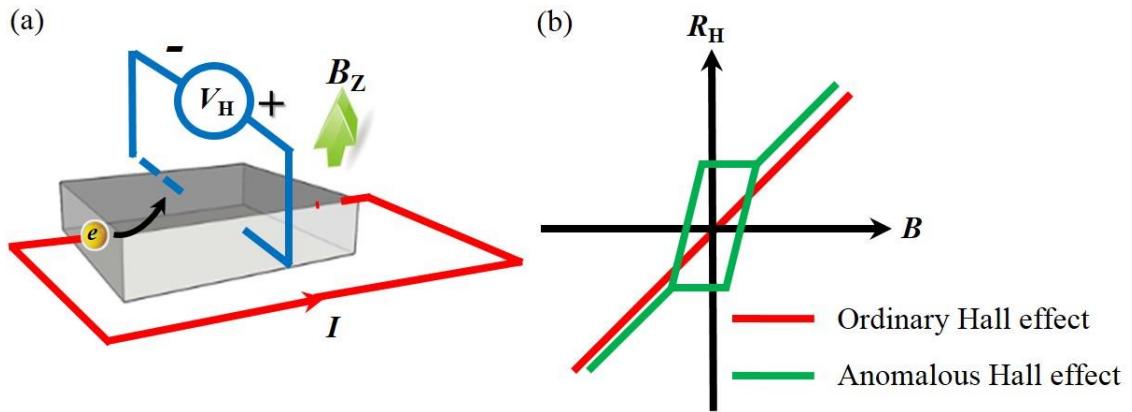
Fig. 2.3. Hall measurement. (a) Hall effect measurement setup. (b) Magnetic field dependence of Hall resistance, R_H in ordinary Hall effect (red line) and anomalous Hall effect (green line).

3. SYNTHESIS OF TOPOLOGICAL INSULATORS

A high quality single crystal of 3D TIs is essential to observe the unique quantum phenomena that arise from the surface state. However, these surface properties are difficult to observe due to the overwhelming contribution of carrier transportation in the bulk state compared to the surface state. Therefore, there has been a rising interest in perfect single crystal growth processes of TIs where the Fermi level of the system lies within the bulk band gap region. Without the perfect single crystal, it would be difficult to observe the interesting unique quantum effects in the laboratory.

3.1. MOLECULAR BEAM EPITAXY

Crystal growth techniques can range from simple, inexpensive processes to complex, expensive ones. There are two primary techniques employed for growing single crystal of TIs: molecular beam epitaxy (MBE) and the modified Bridgman technique.

MBE is a single crystal fabrication technique that produces atomically thin films of crystal deposited on the substrate in an ultrahigh vacuum environment. The absence of impurities, as well as the ultrahigh vacuum environment, results in high purity films grown on the substrate. Other important factors for growing high quality crystals through MBE are precisely controlled substrate temperatures, the lattice matching between the substrate, and the grown material [79,80]. The main advantage of the MBE technique in TI research is that it can deposit a smooth, high quality thin-film of TI materials with a large surface area to volume ratio. This allows for the suppression of bulk transport characteristics relative to the surface and enhancing the surface carrier mobility for detailed transport studies of the topological surface state [81]. Therefore, MBE-grown thin films have been

useful in research [82] for engineering the band structure of TI. Despite the advantages of using this technique, there are challenges in depositing low enough defect density that allows the Fermi level to exist within the bulk band gap. In addition, this technique requires a complicated, expensive setup to operate.

3.2. MODIFIED BRIDGMAN METHOD

In contrast to the MBE technique, the modified Bridgman method is simple, easy and inexpensive. In the modified Bridgman method, all precursor materials of the TI are mixed in a stoichiometric ratio and placed in a 10 mm inner diameter quartz tube. Since the TIs are sensitive to moisture and oxygen, all of the sample preparation processes must be done in a very clean, low humidity, oxygen-free environment before the quartz tube is sealed under vacuum. A low humidity argon gas filled glovebox, shown in Fig. 3.1 (a) and (b), is used in this work. Without such an environment for the sample preparation, impurities could be present and the outcome ingot might be highly oxidized, as shown in Fig. 3 (c). After placing the sample in a quartz tube, it is transferred from the glovebox to the quartz sealing station for evacuate sealing purposes. Fig. 3.1 (d) shows the quartz sealing station equipped with a torch and a vacuum tube sealing unit that includes a pressure gauge, vacuum line, and argon gas line. It is important to note that the open end of the quartz tube is covered by cellophane that is tightened with a rubber band in the glovebox to prevent other gases from diffusing into the quartz tube before the vacuum seal. A hole is punched on the cellophane to maintain the equilibrium pressure before a constriction is purposely made at the center three inches above the bottom end of the quartz tube with the torch, as shown in Fig. 3.1 (e). The inner diameter of the constricted neck is
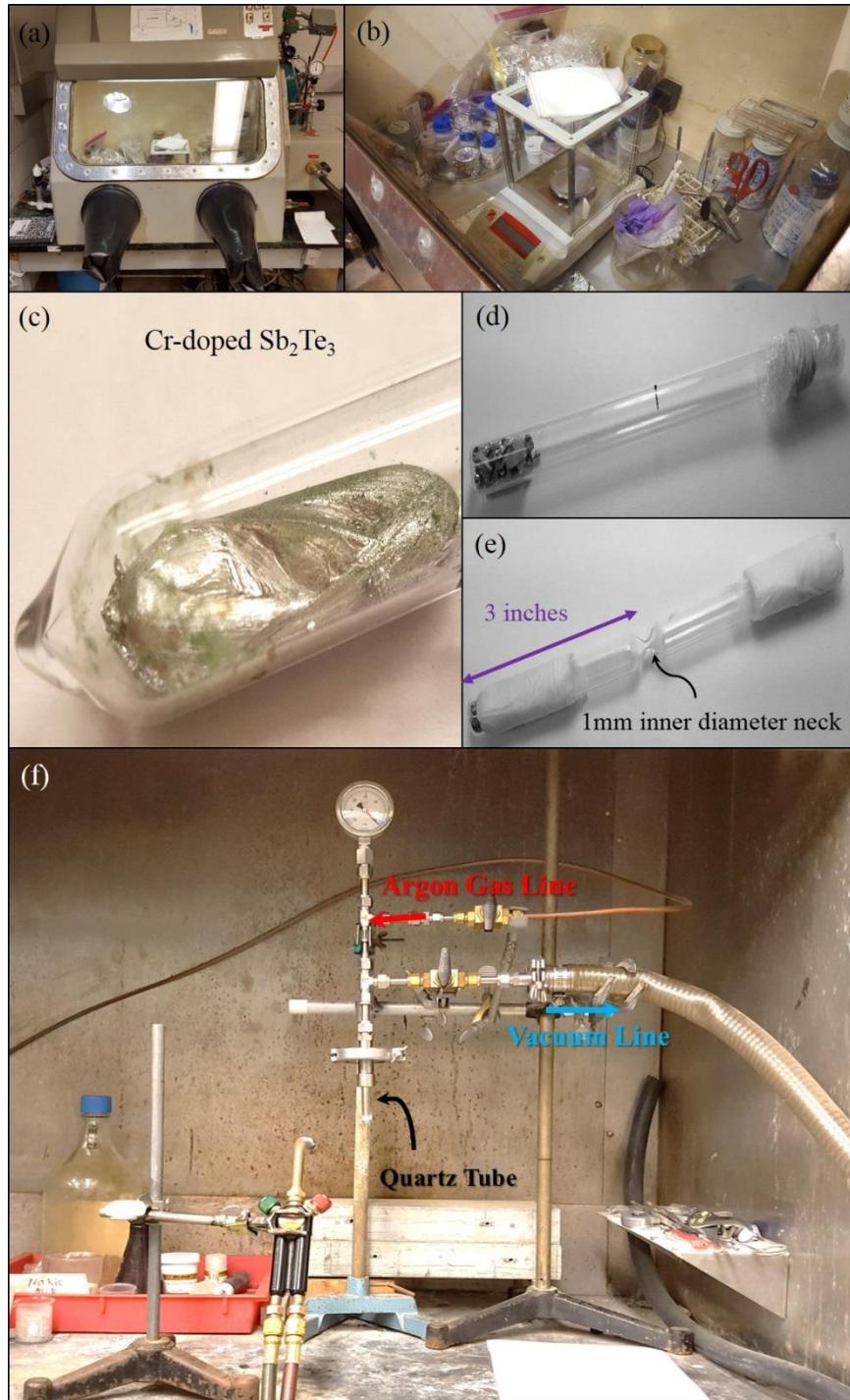
Fig. 3.1. Modified Bridgman method. (a) and (b) show the clean, argon gas filled glovebox used in this work. Desiccant is used to control the moisture inside the glovebox. (c) Green color powder covered over the surface of magnetically-doped TI. This powder is Cr_2O_3 due to the presence of moisture and oxygen inside the ampoule. (d) The open end of the quartz tube is covered by cellophane tightened with rubber band. (e) The starting elements are placed in a quartz tube and a constriction is made at the center of the tube. (f) Vacuum sealing station equipped with torch and vacuum tube sealing unit.

about 1 mm. The small inner diameter of the neck is needed to speed up the vacuum sealing process. This quartz tube is then attached to the vacuum tube sealing unit.

Moisture may be present on the interior wall of the quartz tube. Therefore, a soft bushy flame heats the quartz tube that connects to the vacuum line. The quartz tube is evacuated continuously by the vacuum pump to draw off the moisture and the air for few minutes. The quartz tube is then backfilled with argon gas and re-evacuated. The tube is then reheated to obtain a low partial pressure of oxygen in the tube. These processes are repeated at least three times before sealing the tube at its neck under vacuum conditions at a pressure less than -27 inHg to form an ampoule. The sealed evacuated quartz tube is placed in the box furnace, and the mixture is melted above its melting point. The maximum heating temperature of the box furnace is 1100ºC. The temperature of the box furnace is gradually reduced in order to observe a solidification that will produce a single crystal ingot. The single crystal ingot will go through an annealing process, and then will cool down to room temperature with a constant ramp rate. Fig. 3.2 (a) and (b) show the stoichiometric mixture and its resultant ingot of Bi_2Se_3 inside the sealed evacuated quartz tube, respectively.

On the other hand, to synthesize magnetic TIs and topological superconductors, a thin film of transition metals can be deposited onto the surface of the TI or by chemical doping in TIs. The demonstration of copper intercalated in the van der Waals gaps of Bi_2Se_3, which successfully induces superconductivity at about 3.8 K [58], stimulates the latter approach used to study the effects of the chemically doped TIs system. Intercalation of the Bi_2Se_3 TI with the transition metals of Fe, Mn, and Nb are based on the same approach by the modified Bridgman method, but the quench technique is used to bring the

sample to room temperature. The resultant ingots of $Fe_x Bi_2 Se_3$, $Mn_x Bi_2 Se_3$, and $Nb_x Bi_2 Se_3$ are shown in Fig. 3.2 (c), (d) and (e), respectively. In these systems, not only is magnetism induced, but also superconductivity is observed in $Nb_x Bi_2 Se_3$.
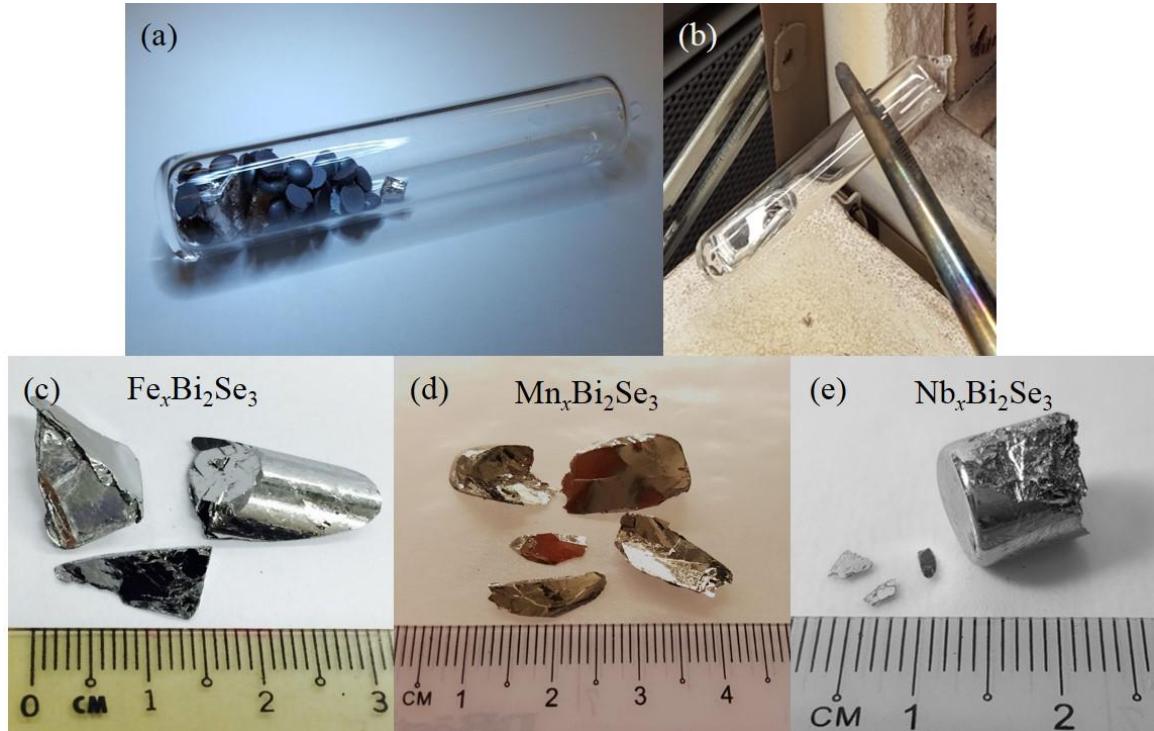
Fig. 3.2. Resultant ingots of chemically doped TIs. (a) A stoichiometric mixture of $Bi_2 Se_3$ inside a sealed evacuated quartz tube. The resultant ingots of (b) $Bi_2 Se_3$, (c) Fe-doped $Bi_2 Se_3$, (d) Mn-doped $Bi_2 Se_3$ and (e) Nb-doped $Bi_2 Se_3$, respectively.

3.3. CHALLENGES IN SYNTHESIZING PERFECT TOPOLOGICAL INSULATORS

The condensed matter physics community is interested in topological materials due to their unusual surface states. For example, in a topological superconductor, the surface state of the materials can host Majorana fermion, whereas in a topological insulator, the

surface state can be a host for the Dirac fermion. Both unusual surface properties can be utilized and fabricated into a dissipationless spintronic device and quantum computation.

To date, the charge transport of TIs is always dominated by the bulk, which arises from the presence of charged structural defects that contribute extrinsic carriers in either the valence or conduction or both bands. This leads to the Fermi level of TI located in the bulk valence band (region (II)) or bulk conduction bands (region (III) instead of in the bulk band gap (region (II)), as shown in Fig. 3.3 (a). The overwhelming contribution of the bulk hampers the investigation and utilization of the Dirac fermions on its surface state. For example, charged selenium vacancies in Bi_2Se_3 TI act as electron donors. This leads to the Fermi level of Bi_2Se_3 located in the bulk conduction band as shown in Fig. 1.2 (c), suggesting the system is n-type material and bulk contribution is always greater than the surface state.

3.3.1. Two-Step Sealing Method. There are two direct approaches to increase the bulk insulating state in Bi_2Se_3. The first approach is through reducing charged selenium vacancies by inventing a new crystal growth method. In reference [83], the p-type Bi_2Se_3 could be achieved if the volume of the reaction space was reduced. Therefore, a two-step sealing method is invented to dramatically reduce the reaction volume for the crystal growth. The details of this method are described in the supplementary materials of Paper III. Fig. 3.3 (b) is the ARPES data of Bi_2Se_3 single crystal grown by this novel method. The Fermi level that lies in the bulk band gap is clearly observed and therefore the bulk is acting as a nearly perfect insulator to exploit the surface transport properties.
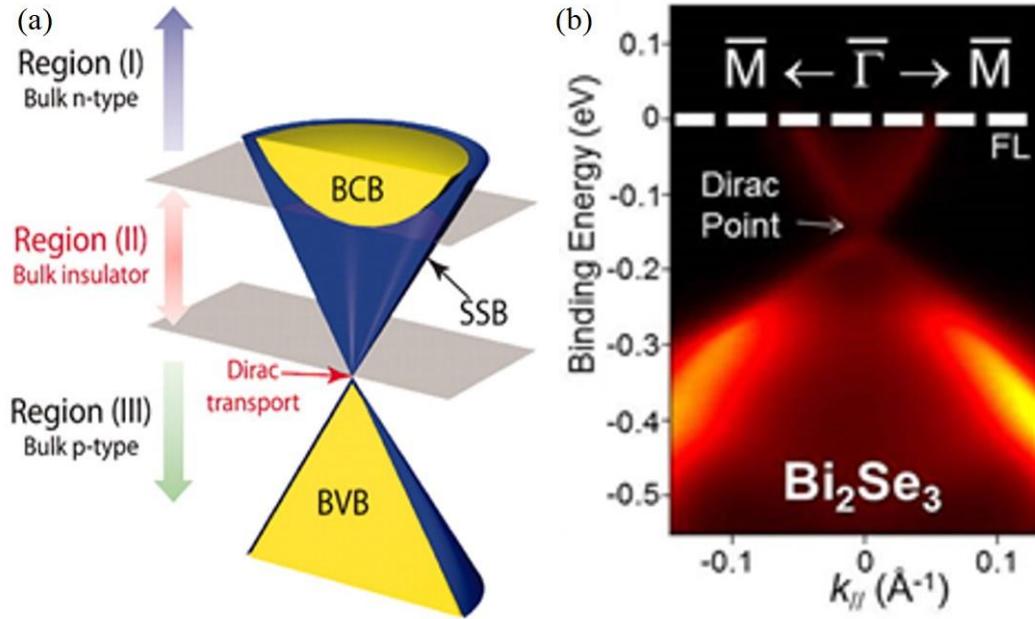
Fig. 3.3. Fermi level in ARPES data. (a) The bulk property of the TI system is defined by the position of the Fermi level. BCB, BVB, and SSB are bulk conduction band, bulk valence band, and surface state band, respectively. For perfect TI, the Fermi level is located in the region (III). (b). ARPES data of Bi_2Se_3 single crystal grown by two-step sealing method. The Fermi level lies in the bulk band gap indicating that the Bi_2Se_3 is a nearly perfect TI. Fig. (a) is adopted from ref. [18].

3.3.2. Electric-Field Exfoliation Method. Another approach to increase the bulk insulating state in Bi_2Se_3 TI is by increasing the surface over volume ratio. This can be achieved by reducing the volume of the system (for example, by exfoliating the bulk material into a thin flake or synthesizing a thin film). Current existing methods in fabricating thin or two-dimensional materials involve expensive and tedious processes such as MBE, as described previously, or inexpensive but unclean mechanical exfoliation (e.g., Scotch tape method). Therefore, the electric-field exfoliation method is invented.

TIs are layered crystalline materials with quintuple layers (QL) ordered in an A–B–A–B–A sequence along the c-axis. These QLs are weakly interacting through the van

der Waals forces, and therefore ultrathin flakes can be exfoliated via an electric field if the exfoliation energy matches with the interlayer binding energy. The exfoliation energy is equal to $\frac{1}{2}\varepsilon_o E^2 A d$, where E is the strength of the electric field, A is the surface area of the crystal, d is the spacing to produce such electric field, and ε_o is the permittivity of free space. Notice that the exfoliation energy is linearly proportional to the square of the electric field, and thus the exfoliation energy is controllable via the simple relation of $E = V/d$ where V is the applied voltage across the conducting plates.

This simple and effective method to obtain clean ultrathin material from the as-grown layered bulk crystals is assembled from a simple apparatus, as shown in Fig, 3.4. The exfoliator consists of homemade conductive plates, glass vacuum chamber, turbo-molecular pump backup by rotary pump, pressure gauge, regulated voltage source and potentiometer. A few tiny as-grown layered materials with surface areas smaller than 1 mm^2 are adhered with a conducting silver paste to one of the conducting plates. An atomically flat substrate is then adhered to the other plate. The plate spacing d was adjusted to the desired distance. Both conducting plates are then placed in a vacuum chamber with the pressure in the range of microTorr. A short DC pulse in the range of 100 volts is applied to the conducting plates. When the electric field is adjusted to match with the binding energy of the layered crystalline materials, the exfoliated ultrathin samples can then be deposited onto the substrate. An atomic force microscope (AFM) is used to determine the topography and height of the exfoliated flakes.

All of the layered crystalline materials possess different interlayered binding energies that cause the determination of the correct electric field to be a challenging task. The correct electric field is essential to obtain an ultrathin sample.
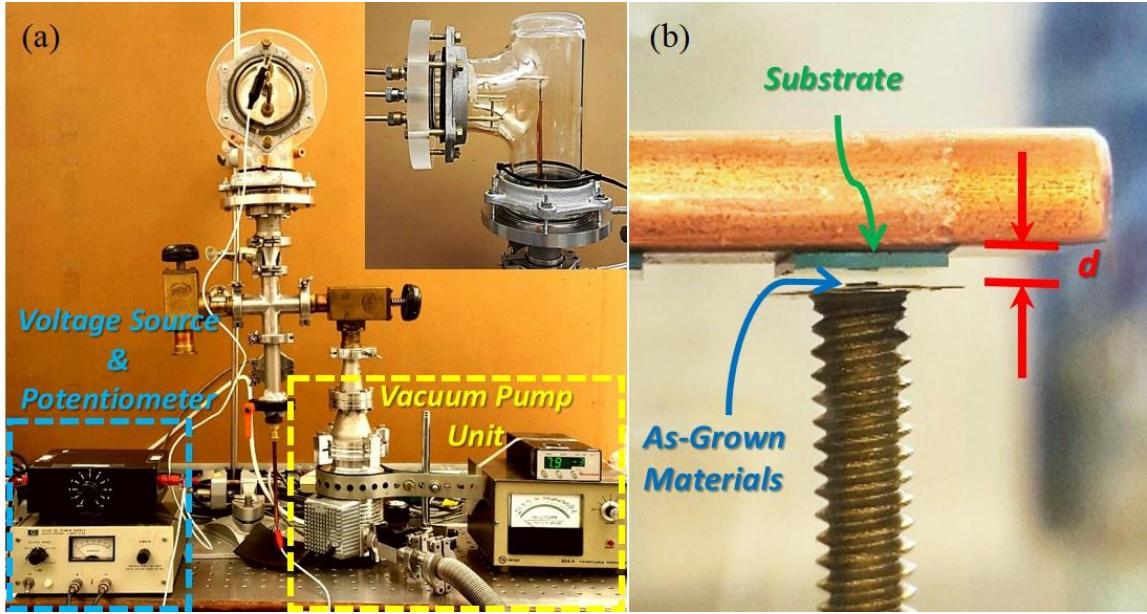
Fig. 3.4. Electric-field exfoliation method. (a) Experimental setup of the electric-field exfoliator. The exfoliator equipped with homemade conductive plates, glass vacuum chamber, turbo-molecular pump backup by rotary pump, pressure gauge, constant voltage source and potentiometer. Inset is the side view of the electric-field exfoliator. (b). A tiny layered crystalline material is mounted on top of one of the conductive plates, whereas the substrate is mounted on another plate.

4. CHARACTERIZATION AND PHYSICAL PROPERTIES MEASUREMENTS

In this work, several tools are employed to study the crystalline structure and physical properties of synthesized crystals. X-ray diffraction (XRD) provides information on the crystallographic structure, chemical composition, phase identification and quantification based on the diffraction pattern of an X-ray beam irradiating a crystalline sample as a function of incident and diffraction angle, 2θ. The physical properties of the samples, such as electronic transportation and magnetism, are studied by employing a commercial system Quantum Design Physical Property Measurement System (PPMS). Sample environment controls in the PPMS including magnetic fields up to $\pm$ 9 tesla and temperature ranges of 1.9–400 K, allows us to probe the phase transition of samples and observe the quantum phenomena at high field and low temperatures. The topography of the exfoliated flake obtained from the electric-field exfoliator is mapped by atomic force microscope (AFM) in tapping mode.

4.1. X-RAY DIFFRACTION

Crystals are periodic arrays of atoms that dictate the physical properties of the material. The crystalline structure of samples can be revealed from neutron diffraction and electron diffraction, but X-ray diffraction is usually the tool of choice. This is because the wavelength λ of the X-rays is typically in the same order of magnitude, in Å scale, with the spacing between planes d in the crystal. In this work, the crystallographic structure and phase identification of TIs were determined by using the horizontal X'Pert Pro Multi-Purpose Diffractometers (MPD) system. Fig. 4.1 (a) shows the setup of the instrument. In XRD measurement, the crystal placed in the sample holder is mounted on a

sample stage. The sample stage is fixed to the goniometer and aligned horizontally. However, the incident X-ray beam monochromator and diffracted X-ray beam detector are movable to make a θ angle. The XRD geometry is shown in Fig. 4.1 (b).
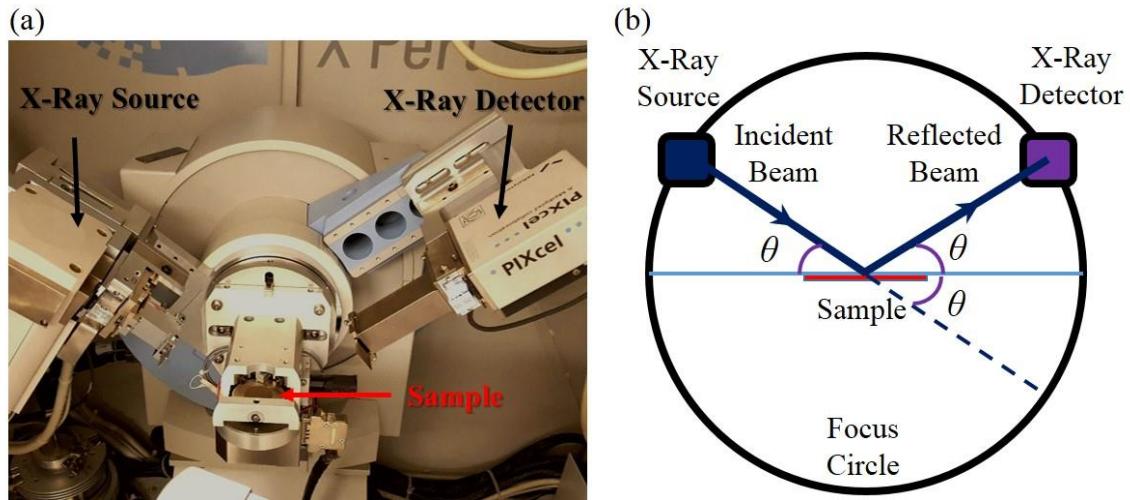
Fig. 4.1. XRD experiment setup. (a) X'Pert Pro MPD Instrument. (b). Powder-XRD geometry used in X'Pert Pro MPD.

When the crystal is illuminated with a finely focused monochromatic X-ray beam, coherent scattering of X-rays at the atoms results in constructive interference at certain well-defined angles as a consequence of the periodically arrays of the atoms in matter. These directions can be determined by Bragg's law:

$$n\lambda = 2d\sin\theta \tag{4.1}$$

where n is the order of the interference, λ is the wavelength of the beam, d and θ are the spacing between diffracting planes and the incident angle, respectively. Fig. 4.2 (a) graphically illustrates Bragg's law. The intensity of the diffracted X-ray as a function of the Bragg angle, 2θ, is therefore yielded. The interplanar spacing d between the different lattice planes is characterized by the Miller indices hkl. The identification of compounds, phases, and Miller indices is achieved by comparing the diffraction pattern of the sample with reference patterns from International Centre for Diffraction Data (ICDD) database. Fig. 4.2 (b) shows a diffraction pattern, also known as diffractogram, of Bi_2Se_3 TI. Based on the diffractogram, it is possible to determine the lattice parameters (a, b, c, α, β, γ) provided that d and the Miller indices of each peak are indexed.
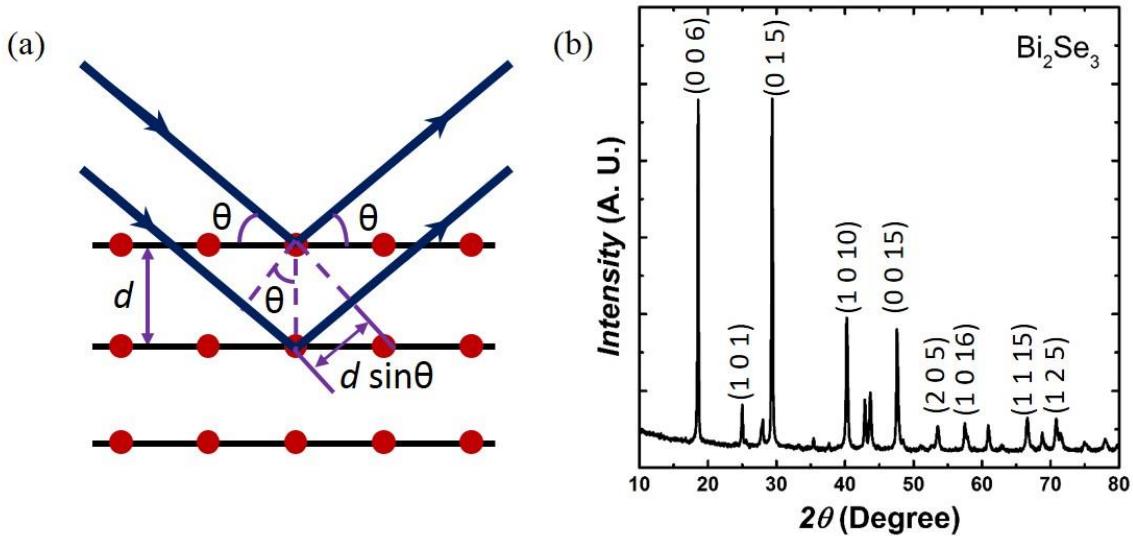
Fig. 4.2. XRD measurement. (a) Graphical representation of Bragg's law. (b). Typical powder-XRD diffractogram of Bi_2Se_3 TI. Selected peaks are indexed with the Miller indices.

4.2. PHYSICAL PROPERTY MEASUREMENT TECHNIQUES

The magnetization and electro-transport measurements presented in this dissertation were all taken using a Quantum Design Physical Property Measurement System (PPMS). The PPMS provides full control of the sample environment, including a magnetic field up to $\pm$ 9 tesla and a 1.9–400 K temperature range. The magnetic field is produced in the vertical direction by a superconducting solenoid composed of a type-II superconductor. The magnitude of the applied magnetic field is based only on the current flowing from the magnet power supply. The whole superconducting solenoid is integrated into the probe that is immersed in a liquid helium bath inside the nitrogen-jacketed dewar. Fig. 4.3 illustrates the PPMS probe. The temperature controlled hardware, sample puck connectors, and the various electrical connections are also incorporated in the probe. All of the measurements are performed in the sealed sample chamber inside the probe under vacuum conditions.

4.2.1. Magnetization Measurement.

The AC Measurement System (ACMS) option in PPMS is capable of performing AC susceptibility and extraction DC magnetization measurements. For both magnetization measurements, the sample is typically mounted inside a plastic straw with a diameter of 5 mm. The sample can be secured inside the straw by sandwiching the sample between two plugs inserted into the plastic straw. These plugs are made of rolled plastic straw. When the magnetic moment of the straw is measured, its diamagnetic moment is very small.

The ACMS contains an insert coil set that fits directly in the PPMS sample chamber and a 7.7 mm diameter sample space that lies within the uniform magnetic field region of the host PPMS. Therefore, DC field and temperature control can be performed in this setup.

The sample is placed within the sample space at the end of a light, rigid sample rod. Fig. 4.4 shows the ACMS coil set schematically.

During DC measurements, the sample is magnetized by a constant magnetic field and translated vertically and quickly through two detection coils by a DC servo motor. The magnetic moment of the sample is measured by the extraction method. According to Faraday's law, the voltage is induced in a set of copper pickup coils by the moving the sample. DC measurements are useful to determine the nature of the magnetic ground state
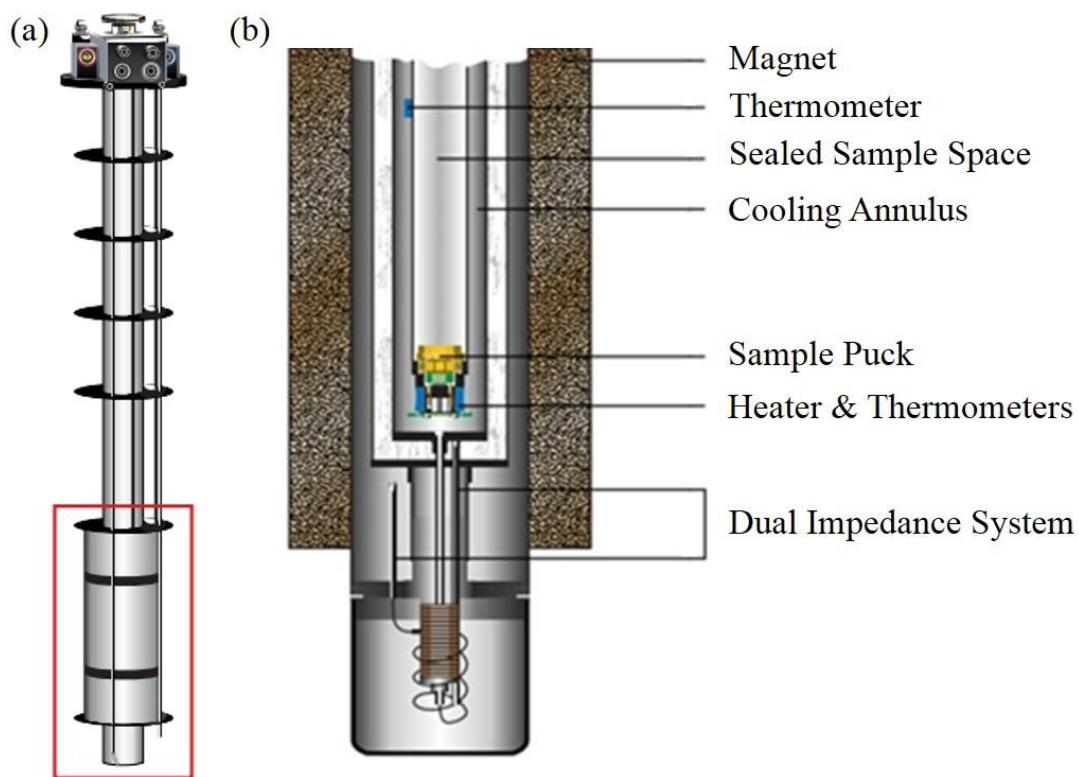
Fig. 4.3. Major components of the PPMS probe. (a) The overall PPMS probe. (b) Magnified view of the PPMS bottom part as red boxed in (a). The superconducting solenoid, the temperature control hardware, the sample puck connector and various electrical connections are incorporated in the probe. Fig. (a) and (b) are adopted from the PPMS product brochure 1070-002.
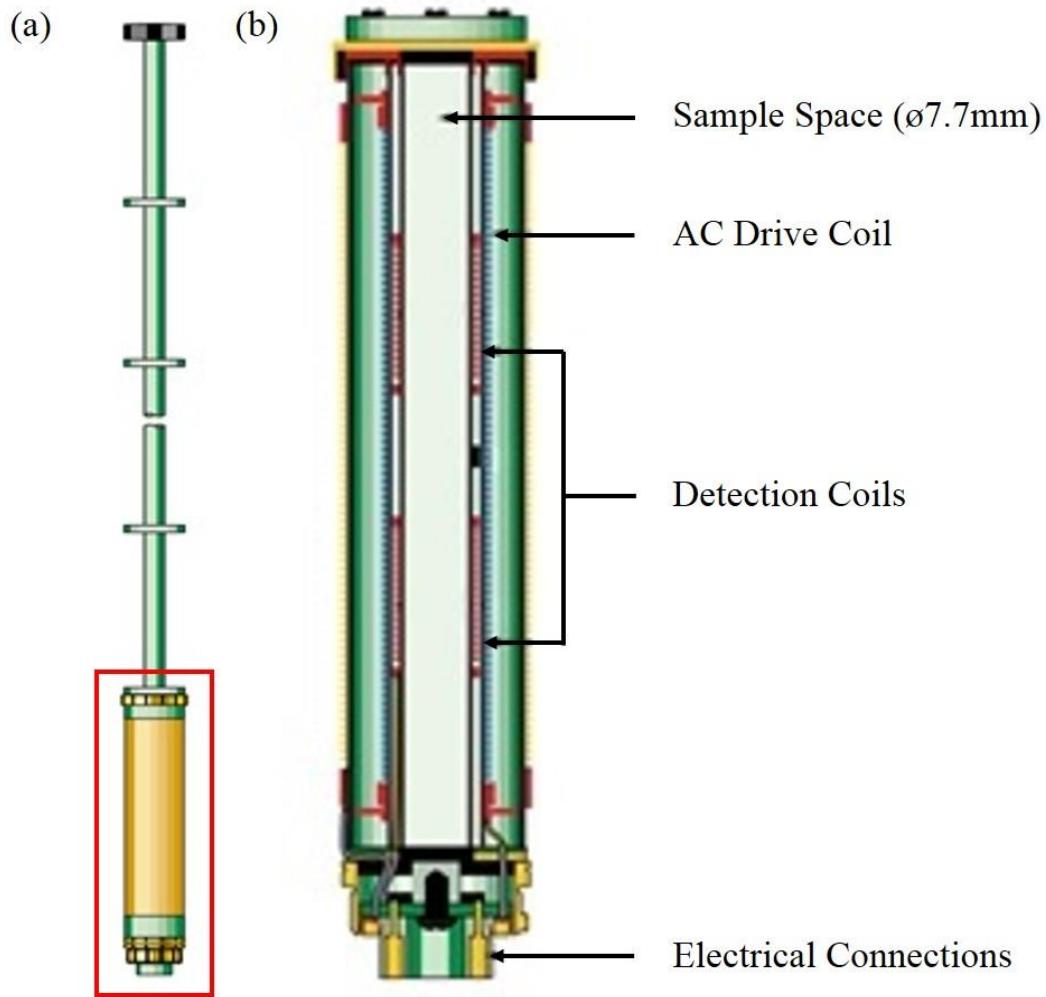
Fig. 4.4. ACMS coil set. (a) The overall ACMS coil set. (b) Magnified view of the ACMS coil set bottom part as red boxed in (a). AC drive coil provides an alternating excitation field and a detection coil set that inductively responds to the sample moment. Fig. (a) and (b) are adopted from the PPMS product brochure mag7-16.

and to examine its magnetic phase transitions, whereas during AC measurements, the sample is positioned in the center of each detection coil and an alternating field is applied to the measurement region. The applied field that is altered by the presence of the sample is detected by the detection coils. Therefore, AC measurement is useful to examine the

Meissner effect in the superconducting state of a superconductor. AC susceptibility yielded

by the AC measurement is also used to characterize the spin-glass behavior.

4.2.2. Resistivity Measurement. When electrons move through a sample, they

encounter resistance to their motion. In order to move electrons against the resistance, a

potential difference between the ends of the sample needs to be applied. Ohm's law states

that to produce a current I through a sample with resistance R, the potential difference V

that required is $V = IR$. The resistance of the sample depends on the particular material

from which it is synthesized. The quantity that characterizes the resistance of a given

material is its resistivity ρ_{xx}. The resistance of a sample is proportional to the length l and

inversely proportional to the cross-section area A that current passed through.

Mathematically, the resistance of a sample can be expressed as $\boldsymbol{R = \rho_{xx} l / A}$.

In order to measure a sample's resistivity, a PPMS equipped with a resistivity

measurement system is employed. The measurements are performed on a rectangular

sample of uniform thickness using a standard four-probe technique between 2 K and 300 K.

Platinum wires are used as contact leads. All of the leads are attached parallelly on a sample

as shown in Fig 4.5. A constant current is passed through a sample from contact $I+$ to

contact $I-$ and the voltage is measured across contacts $V+$ and $V-$. The resistivity of the

sample can be derived with the known sample geometry, the current through the sample,

and the measured voltage drop across the sample. By using the standard four-probe

technique, the contribution of the leads is greatly reduced and the derived sample resistivity

is in a high degree of accuracy. Magnetoresistance of the sample can also be measured in

this experiment setup by applying an external magnetic field at a constant temperature.
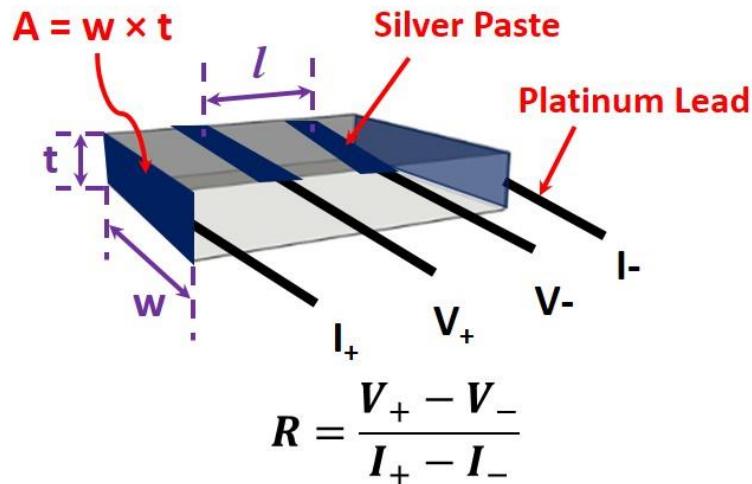
Fig. 4.5. Standard four-probe technique with silver paste cured at room temperature used for the contacts is employed for the resistivity measurement. To prevent the sample from electrical heating, a small direct current is applied from the contact $I+$ to contact $I-$. Two separate leads are used to measure the potential difference across the sample, and Ohm's law is used to calculate the sample resistivity.

4.2.3. Hall Resistivity Measurement. The AC Transport Measurement System (ACT) option in the PPMS incorporates with a precision current source and a precision voltmeter that supports Hall effect measurements. The precision current source and voltage detector have a resolution of 0.02 μA and 0.02 μV, respectively. The ACT option can supply an AC bias current from 1 Hz up to 1 kHz, and can therefore provide a greater measurement sensitivity than DC instruments because signal filtering can be employed.

When the charged particles q move perpendicular to a magnetic field, a Lorentz force $\boldsymbol{F}$ is exerted perpendicularly to both the field and the direction of the particle motion, which will follow $\boldsymbol{F} = q\boldsymbol{v} \times \boldsymbol{B}$. Therefore, the measurements are typically made by passing a known longitudinal current I through a sample and measuring the transverse voltage or Hall voltage V_{yx} at an applied magnetic field B. The sign of the Hall voltage generally

indicates the type of charge carrier dominated in a sample and the magnitude of the Hall voltage is related to the charge carrier density. The Hall coefficient R_h is defined by $R_h = V_{yx}A/IlB$, where A is the sample cross-section area and l is the separation of the transverse voltage leads. It can be shown that $R_h = 1/nq$, where n is the number of charge carriers per unit volume in the sample. The most accurate method of obtaining the Hall coefficient is by measuring the Hall resistivity ρ_{yx} as a function of applied magnetic field. Therefore, a plot of ρ_{yx} versus field in a Hall measurement should yield a straight line with slope equal to R_h. A positive R_h indicates a p-type charge carrier dominated in a sample and vice versa.

The configuration for a four-probe Hall resistivity measurement confirms the premise of the Hall effect. However, the Hall field is superimposed on top of the bias field from the two current leads, so accurately measuring the Hall potential with a four-probe measurement can be difficult. To measure only the potential difference due to the Hall potential, the voltage leads of $V+$ and $V-$ must delineate a perfect perpendicular relationship to the bias field. If this is not the case, longitudinal voltage V_{xx} is greatly contributes to the measured voltage $V_{measured}$, and the precision of the Hall voltage is sacrificed, as shown in Fig. 4.6 (a). Therefore, five-probe Hall measurement is used for all the Hall measurements presented in this dissertation. In a five-probe Hall measurement as shown in Fig. 4.6 (b), a fifth voltage lead is attached and aligns in parallel to one of the voltage leads. An external 100 Ω potentiometer is used in the five-probe Hall measurement to nullify the longitudinal voltage. Hence, the voltage measured between $V+$ and $V-$ only provides the Hall voltage V_{yx} and Hall resistivity $\rho_{yx} = V_{yx}A/Il$ can be obtained. Fig. 4.6 (c) shows the setup for measuring two samples simultaneously.
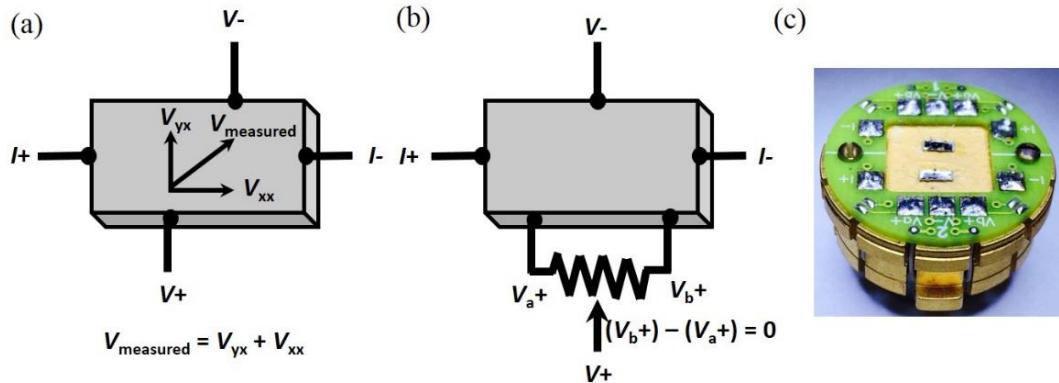
Fig. 4.6. Hall resistivity measurement. (a) Leads attached on bar sample for four-probe Hall resistivity measurements. (b) Offset nulling is performed with a five-probe Hall resistivity measurement. The potential difference between $V+$ and $V-$ is Hall voltage V_{yx}. (c) Five-probe Hall resistivity measurement with samples mounted on ACT sample puck.

4.3. ATOMIC FORCE MICROSCOPE

Atomic force microscopes are one of the powerful microscopy tools for imaging, measuring and manipulating matter at nanoscale. It is capable of generating images at an atomic resolution with angstrom scale resolution height information. AFM uses a cantilever with a very sharp tip at its end to scan over the sample surface. The radius of the curvature of the tip is in the order of nanometers. As the tip is brought into proximity of a sample surface, the forces between the surface and tip cause the cantilever to deflect. Depending on the situation, the forces measured in AFM include mechanical contact force, van der Waals forces, electrostatic forces, magnetic forces, etc. Therefore, AFM can be operated in several modes to map the sample topography and to study the changes in the physical properties arising from the changes in an atomic arrangement through atomic manipulation. In this work, Digital Instrument Multimode^{TM} SPM in tapping mode, as shown in Fig. 4.7 (a), was used to study the topography of the exfoliated flakes obtained from the electric-field exfoliation method.

(a)
Photodiode Adjustment Knobs

Laser Adjustment Knobs

Tip

Tip Holder

X-Y Head Translator

Sample

Retaining Springs

Scanner

Coarse Adjustment Screws

Motor Control Switch

Mode Selector Switch

Base

Output Signals

0.60

(b)

Photodiode

Incident Laser Beam

Cantilever

Lens

AFM Tip

Sample

Height (nm)

Position (nm)
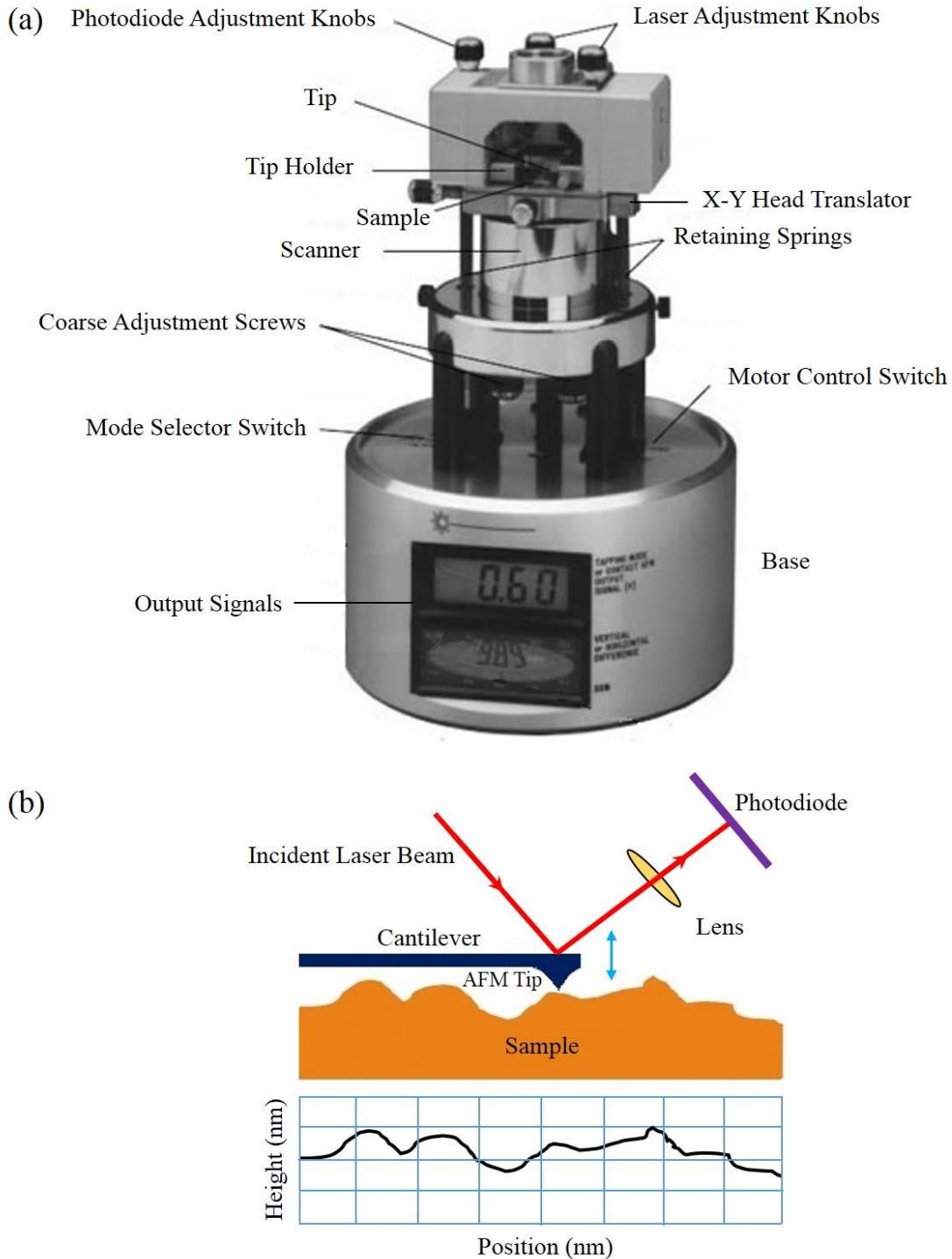
Fig. 4.7. AFM measurement. (a) The instrument is set into the tapping mode and the tip, laser, mirror, and photodiode must be aligned before the measurement. (b) The laser beam is focused on the back of a cantilever that moves vertically on the surface of a sample and the deflections of the beam are detected by a position-sensitive photodiode to track the surface for imaging and measuring. Fig. (a) is adopted from the Digital Instruments Multimode[TM] SPM Instruction manual.

In tapping mode AFM, the tip on the cantilever is modulated through mechanical oscillation at its resonance frequency. This oscillation is oscillated vertically by using a small piezo element in the cantilever holder. A laser beam is focused at the back of the reflective cantilever that moves vertically on the surface of a sample. The laser beam is then reflected from the cantilever onto a detector via a mirror or lens. A position-sensitive photodiode is used as a detector to track the changes.

The signal from the photodiodes is rectified and passed through a feedback loop to control the tip-sample interactions, which are force and tip position. In principle, the damping of the cantilever is held constant by moving the tip in the z-direction as it is simultaneously translated in the x- and y-direction to track the surface for imaging and measuring. Fig. 4.7 (b) schematically illustrates the working principle of AFM in tapping mode. Since an oscillating tip is used in tapping mode, it eliminates shear forces that can damage the samples and reduce image resolution.

PAPER

I. DIRAC SURFACE STATE OF THE ANTIFERROMAGNETIC TOPOLOGICAL INSULATOR $Fe_xBi_2Se_3$

Seng Huat Lee[1], Julie E. Medvedeva[1], Maria Iavarone[2],
Wenhan Zhang[3], Weida Wu[3], William Ratcliff[4] and Yew San Hor[1]

[1]*Department of Physics, Missouri University of Science and Technology, Rolla, MO 65409*

[2]*Department of Physics, Temple University, Philadelphia, PA 19122*

[3]*Department of Physics and Astronomy, Rutgers University, Piscataway, NJ 08854*

[4]*NIST Center for Neutron Research, National Institute of Standards and Technology, Gaithersburg, MD 20899*

ABSTRACT

Magnetically doped topological insulators are essential for exploring exotic quantum phenomena such as quantum anomalous Hall effect. Here we report the observation of the antiferromagnetic topological insulator with a high magnetic phase transition at ~100 K by using iron as bulk dopants into Bi_2Se_3. $Fe_xBi_2Se_3$ is also metamagnetic material with the critical field at about 400 Oe. Angle-resolved photoemission spectroscopy (ARPES) and magnetic susceptibility data revealed the coexistence of topological surface state with antiferromagnetic order. From the angle-dependent Shubnikov-de Haas oscillations accompanied by a quantum Hall effect, the existence of the massive, two-dimensional quantum transport Dirac fermions in the magnetic topological insulator is observed. Berry's phase is also determined. The magnetotransport features indicated that the massive Dirac fermions originate from the bulk of the sample acting as many parallel 2D conduction channels.

I. INTRODUCTION

Topological insulators (TIs) are bulk insulators due to the strong spin-orbit coupling and possess gapless Dirac-like conducting surface states protected by the time-reversal symmetry that gives rise to interesting surface transport phenomena [1–6]. Several schemes have been proposed to search for image magnetic monopole [7], dynamical axion field [8–11] and realize unique quantum effects such as anomalous magnetoresistance [12] and anomalous quantum Hall effect (QAHE) [13–15]. All the proposed schemes depend on magnetic topological insulators where the time-reversal symmetry (TRS) is broken and consequently, gap opening between the Dirac cones of the surface states [5,16,17] and chiral edge state exist on the magnetic domain walls. In fact, the magnetism breaks the topological protection of surface states prevents us from fully utilizing the spin-orbit coupling of the Dirac cones [18]. Fortunately, the coexistence of the Dirac surface state with magnetism is possible in antiferromagnetic TI that has been predicted by the theoretical study [19–22].

Since antiferromagnetic topological insulators only break TRS locally and preserve the topological surface gapless states make it be a promising spin-orbit torque material for fabrication into antiferromagnetic topological spintronic [23–28]. Technologically, topological transport in antiferromagnetic TI is more robust than in the ferromagnetic TI, and the recent demonstration of manipulation the magnetic ordering of antiferromagnets by electric current [28] has shifted its focus from ferromagnetic metal spintronic to antiferromagnetic topological spintronic. At present, however, antiferromagnetic order with the topological surface state remain experimentally elusive.

Chemically doping into the three-dimensional TI system is one of the direct approaches to realize antiferromagnetic TI. As one of the TIs, Bi_2Se_3 has a single Dirac

surface state with a large bulk bandgap of 0.3 eV and the Dirac point residing in the gap [29,30]. Its surface state has been directly revealed by angle-resolved photoemission spectroscopy (ARPES) and scanning tunneling microscopy (STM) [6,29,31,32]. It is widely used as a host material to study the magnetic perturbations and experimentally realize the exotic quantum effects. In this letter, we show that the Bi_2Se_3 can be tuned into an antiferromagnetic order with the presence of the topological surface state by Fe intercalation. Its magnetic phase transition occurs at 100 K with out-of-plane easy magnetization axis. We discovered that $Fe_xBi_2Se_3$ is also a metamagnetic system where the system can be driven into a ferromagnetic phase at 400 Oe. Angle-dependent Shubnikov-de Haas oscillations (SdHO) accompanied by a quantized Hall effect originates from the parallel 2D electron systems in the bulk of the sample were also observed. The high-temperature phase transition of antiferromagnetic TI with such phenomena have not been observed in the previous magnetic doped topological insulators.

II. METHODS

Single crystals of high-quality $Fe_xBi_2Se_3$ were grown by melting stoichiometric mixtures of high purity iron (99.99%), bismuth (99.999%) and selenium (99.999+%) with different nominal x values at 950 ℃ for 55 hours in evacuated quartz tubes. The crystalline samples were furnace cooled to 550 ℃ and annealed for three days followed by quenching the evacuated quartz tubes in water to bring them to room temperature. The crystal surface was studied by using the scanning tunneling microscope (STM) and angle-resolved photoemission spectroscopy (ARPES). The samples for STM and ARPES measurements were cleaved at ultrahigh vacuum environment to expose a pristine surface. ARPES measurements at 12 K were conducted at the PGM beamline of the Synchrotron Radiation

Centre, University of Wisconsin, equipped with a Scienta R4000 analyzer. Commercial system (Quantum Design, PPMS) was employed to perform the DC magnetization, resistivity and magnetotransport measurements. The standard four and five-probe techniques with silver paste cured at room temperature used for the contacts was employed for the longitudinal resistivity, ρ_{xx} and Hall resistivity, ρ_{yx} measurement, respectively. All the electric current was applied in the basal plane *ab* of the crystals.

III. RESULTS & DISCUSSION

Based on the first-principles density functional calculation (DFT) with the association of *ab*-initio calculation, the physical properties of Fe-doped Bi_2Se_3 can be easily understood and its structure is being modeled. The possible favorable sites of Fe atom inside the crystals via intercalation in between two quintuple layers or interstitial inside the quintuple layer (QL) are displayed in Fig. 1 (a). Magnetic moment/Fe atoms in different lattice sites are obtained from the calculation. The magnetic moment is in between 2.08 μ_B to 2.32 μ_B. The largest magnetic moment m_{Fe} occurs for Fe intercalation. Based on the calculated formation energy for different lattice sites of Fe atoms, the intercalation of Fe atom in between QLs is more favorable due to the minimum enthalpy. Thus, Fe intercalation not only maximizes the magnetic coupling to the Bi_2Se_3 but also possess lowest total energy for the entire system.

STM topographies confirm the existence of Fe intercalation in Bi_2Se_3. Bias-independent of bright protrusions are clearly observed, as shown in Fig. 1 (d) and (e), suggesting the protrusions located on the (001) cleaved surfaces. The protrusions are also intercalated in between the quintuple layers beneath the surface due to the observation of the various intensities as compared to the background. These protrusions

(a)

Se
Bi
Se
Bi
Se

z

x

(b)

Fe Site	E_{Total}^{NM} (meV)	E_{Total}^{FM} (meV)	Magnetic Moment, μ_B
Fe_i (1)	+377	0	2.32
Fe_i (2)	+637	+42	2.26
Fe_i (3)	+1024	+365	2.08

(c)

x	n (10^{19} cm^{-3})
0.01	5.11
0.05	6.34
0.15	6.37
0.20	7.58
0.25	8.08

ρ (mΩ cm) vs T (K)

$B = 0$

(d) -1 V, 10 pA High 20 nm

(e) +1 V, 10 pA 20 nm Low
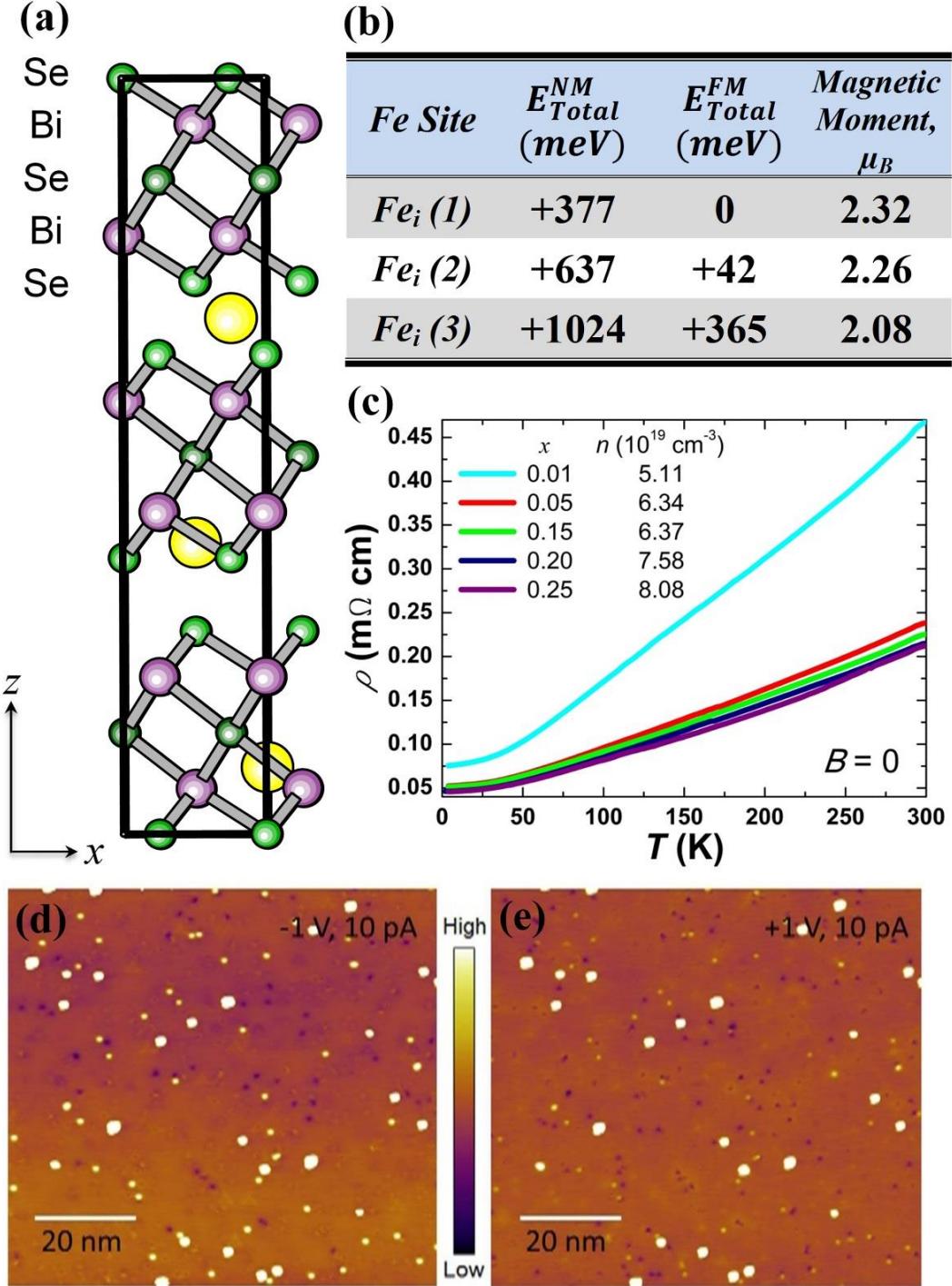
FIG. 1. (a) Side view of $Fe_xBi_2Se_3$ model structure based on first principles DFT. Yellow sphere is Fe atom. (b) Calculated parameters based on DFT. (c) Temperature-dependent resistivity in the *ab*-plane of Fe-doped variants. All stoichiometric iron doped materials are *n*-type, metallic samples. STM topographic images of $Fe_{0.05}Bi_2Se_3$ showing the (d) filled stated at a bias voltage of -1.0 V and (e) unfilled stated at a bias voltage of +1.0 V. The bias-independence of bright protrusions are clearly observed.

could be due to either the Fe cluster or FeSe, as these protrusion are absent in the parent compound of Bi_2Se_3. The defects with a strikingly similar STM appearance have been recently observed for Fe doped on Bi_2Te_3 [33] and Bi_2Se_3 [34,35]. From the powdered X-ray diffraction (XRD) analysis, the crystals have the identical rhombohedral layered crystal structure as host material Bi_2Se_3. As the Fe doping concentration increases, the minority secondary phases BiSe and FeSe are observed. These results are consistent with the STM finding.

ARPES data of host material Bi_2Se_3 along the $\overline{M} - \overline{\Gamma} - \overline{M}$ momentum space in Fig. 2 (b) shows a Dirac surface state with the Dirac point lying about 0.15 eV below the Fermi level (FL) with the FL intersecting the electron-like bulk conduction band. According to the theoretical study, a gap is expected to exits in the surface state if the magnetic impurities are introduced into the system. The ARPES measurements, however, confirm the magnetic TI coexistence with topological surface states without the energy gap opening even up to 25% of Fe doping into the Bi_2Se_3. With the increasing of Fe-doping concentration, the Dirac point is dramatically moved away from the FL. From the Hall measurement, all stoichiometric Fe-doped materials possess n-type charge carrier and exhibit metallic behavior with resistivities saturated in the range of 45.8-75.6 $\mu\Omega$-cm at a temperature of 5 K. As the Fe doping increased, the n-type concentration continues to increase from 5.11×10^{19} cm^{-3} to 8.08×10^{19} cm^{-3}. This is consistent with Fe acting as a highly effective electron donor and caused metallic behavior. The bulk mobility μ_{bulk} about 1778 ± 127 cm^2/Vs is calculated based on the carrier density and the resistivity results at 5 K.
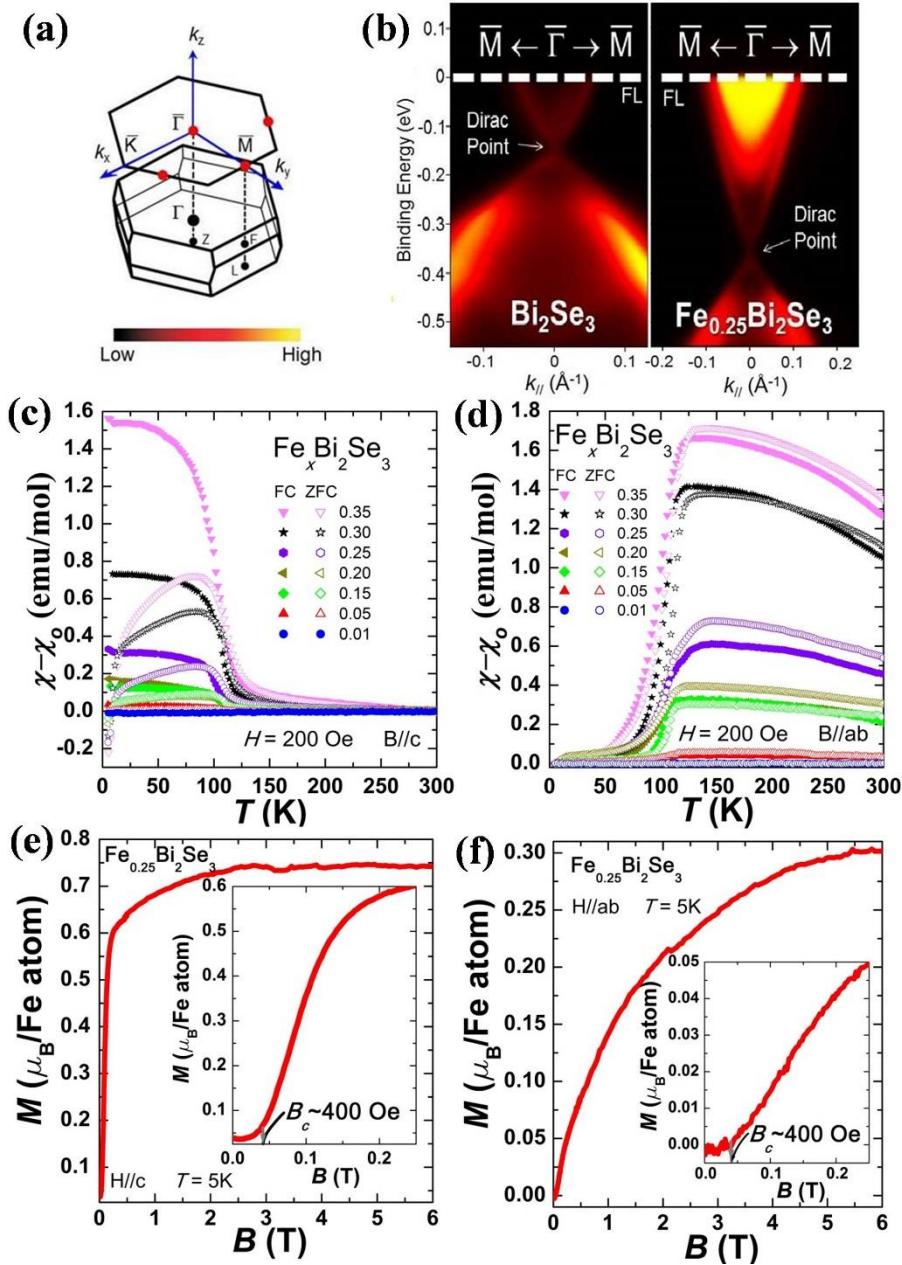
FIG. 2. (a) 3D bulk Brillouin zone of Bi_2Se_3 with the hexagonal surface Brillouin zone, space group $R\bar{3}m$. (b) ARPES spectra for Bi_2Se_3 and $Fe_{0.25}Bi_2Se_3$ along the $\bar{M} - \bar{\Gamma} - \bar{M}$ direction at 12 K. Both have a single Dirac point connecting the upper and lower Dirac cones. Surface bandgap was no observed on iron-doped Bi_2Se_3. (c), (d) Field cooled (FC) and zero field cooled (ZFC) temperature-dependent magnetic susceptibility χ measured at 200 Oe for the crystal aligned with the magnetic field perpendicular ($B//c$) and parallel ($B//ab$) to the basal plane, respectively. The ground state of the Fe-doped crystals is antiferromagnetic. (e), (f) Field-dependent magnetization M for the crystal aligned with magnetic field perpendicular ($B//c$) and parallel ($B//ab$) to the basal plane at 5 K. Inset in (e), (f) Magnetization in the low field regime. The magnetic transition occurs at the critical field about 400 Oe.

For the magnetic properties, the temperature dependence of magnetic susceptibility was performed in a magnetic field parallel to the c-axis of the crystal ($B//c$). The results illustrated in Fig. 2 (c) is subtracted from the temperature-independent term χ_o. Weak diamagnetism is observed at high temperatures for iron concentration lower than 0.15, indicating the weak paramagnetic contribution from the Fe that only becomes significant at low temperatures. For the magnetization measurements, field cooled (FC) and zero field cooled (ZFC) condition are applied. In the ZFC condition, the measurement was performed in the warming up process at 200 Oe applied magnetic field after the sample was cooled down from 300 K to the desired temperature of 5 K in zero fields. Whereas the measurement performed in the cooling process with the field is known as FC condition. For FC condition, when the Fe doping increased to 15% or beyond, the system becomes ferromagnetic as confirmed by the observation of a relatively large susceptibility at temperature $T_c \sim 100$ K. The magnetic of susceptibility tends to be saturated at lower temperatures. The susceptibility of the samples increases as the iron doping increased. Interestingly, the antiferromagnetic phase transition is observed under the zero-field cooled (ZFC) condition. This is confirmed by the magnetic susceptibility decreasing sharply at temperature $T_N \sim 100$K. For the crystal aligned with the magnetic field parallel to the basal plane ($B//ab$), the susceptibility for both FC and ZFC conditions increased monotonically with the decreasing temperature from 300 K as shown in Fig. 2 (d). The susceptibility reaches the maximum at a critical temperature of 100 K. As the temperature continues to decrease, however, both curves show the antiferromagnetic behavior. Both of these results in $B//c$ and $B//ab$ confirmed the Fe doping has an antiferromagnetic ground state. Compared with others magnetic phase transition topological system, $Fe_xBi_2Se_3$ have a

magnetic order with high transition temperature, which is about ten times higher than existing magnetically doped TIs [36]. This phase transition is not due to the magnetic clusters of FeSe that have Curie temperature higher than 100 K [37]. Thus, the observation of this antiferromagnetic ordering may exclude effects from some possible magnetic clusters.

In order to understand the observation of different magnetic phase transitions for $B//c$, magnetization as the function of the magnetic field was performed. Fig. 2 (e) and (f) show the field dependent magnetization at 5 K for a $Fe_{0.25}Bi_2Se_3$ single crystal aligned with the magnetic field parallel to the c-axis and the basal plane, respectively. Both magnetization data were subtracted from the diamagnetic background. In Fig. 2 (e), the magnetization for $B//c$ increases sharply at the very low field about 400 Oe and reaches to its maximum magnetization at 3 T then saturated at 0.75 μ_B/Fe atom. Whereas the magnetization for $B//ab$ increases much more slowly. The inset of both Fig. 2 (e) and (f) emphasize the low field magnetization increase dramatically in the magnetization form both crystal alignments. This suggests two things: First, the easy axis of magnetization is in c-axis with the spontaneously ordered magnetic moments in the ferromagnetic phase aligned parallel to the c-axis. The sharp field-induced phase transition into a state with prominent magnetic anisotropy and explains the observation of ferromagnetism at FC condition for $B//c$ where the antiferromagnetic transition is suppressed by an applied magnetic field along the c-axis. Second, the observation of sharp field-induced phase transition indicating Fe-doped Bi_2Se_3 is a metamagnetic system with the critical field about 400 Oe for both crystal alignments.

The quantum oscillatory phenomena at the high magnetic field were observed in Fig. 3 (a). Magnetotransport dependent on Landau levels of 2D carriers should depend only on the perpendicular component of the magnetic field $B_\perp = B\cos\theta$ and periodically in $1/B$. In order to confirm the origin of the oscillations, the magnetic field is tilted so that the angle between the magnetic field and the c-axis is defined as the tilt angle θ. No oscillatory feature was observed for angle beyond 30° within the field limit. Fig. 3 (b) shows the background subtracted oscillations signal ΔR_{xx} grow with the increasing field, consistent with Shubnikov-de Haas oscillations (SdHO). From the Fourier analysis on ΔR_{xx}, it is found that the obvious dips are periodic in $1/B$ and yield a single frequency of $B_F = 290.3$ T as shown in the inset of Fig. 3 (c). From the Onsager relation $B_F = \hbar A/2\pi e$, where A is the cross-section of the Fermi surface perpendicular to the magnetic field, the Fermi wave vector $k_F = 0.0939$ Å was obtained by assuming the Fermi surface had a circular shape. The k_F is in agreement with the value from the ARPES data. Moreover, 2D carrier density $n_{2D} = eB_F/h$ can also be extracted by using the B_F obtained above. Therefore, the n_{2D} is 7.02×10^{12} cm^{-2} per spin. By using the B_F/B, where the B is the magnetic field position of each ΔR_{xx} minimum, values close to the integers N corresponding to the Landau levels (LL) were obtained. The dashed lines in Fig. 3 (b) represent the LL index N and it drifts from the perfect alignment, this is likely due to the tilt angles not being the exact value it measured. In Fig. 3(c), the B position of the 38th Landau level as the function of θ is well fitted by the $B_{38}(\theta=0)/\cos\theta$, which is evidence of the 2D properties of the SdHO under the perpendicular component of the magnetic field. The origin of the quantum oscillation, however, is not from the surface state transport but from the bulk
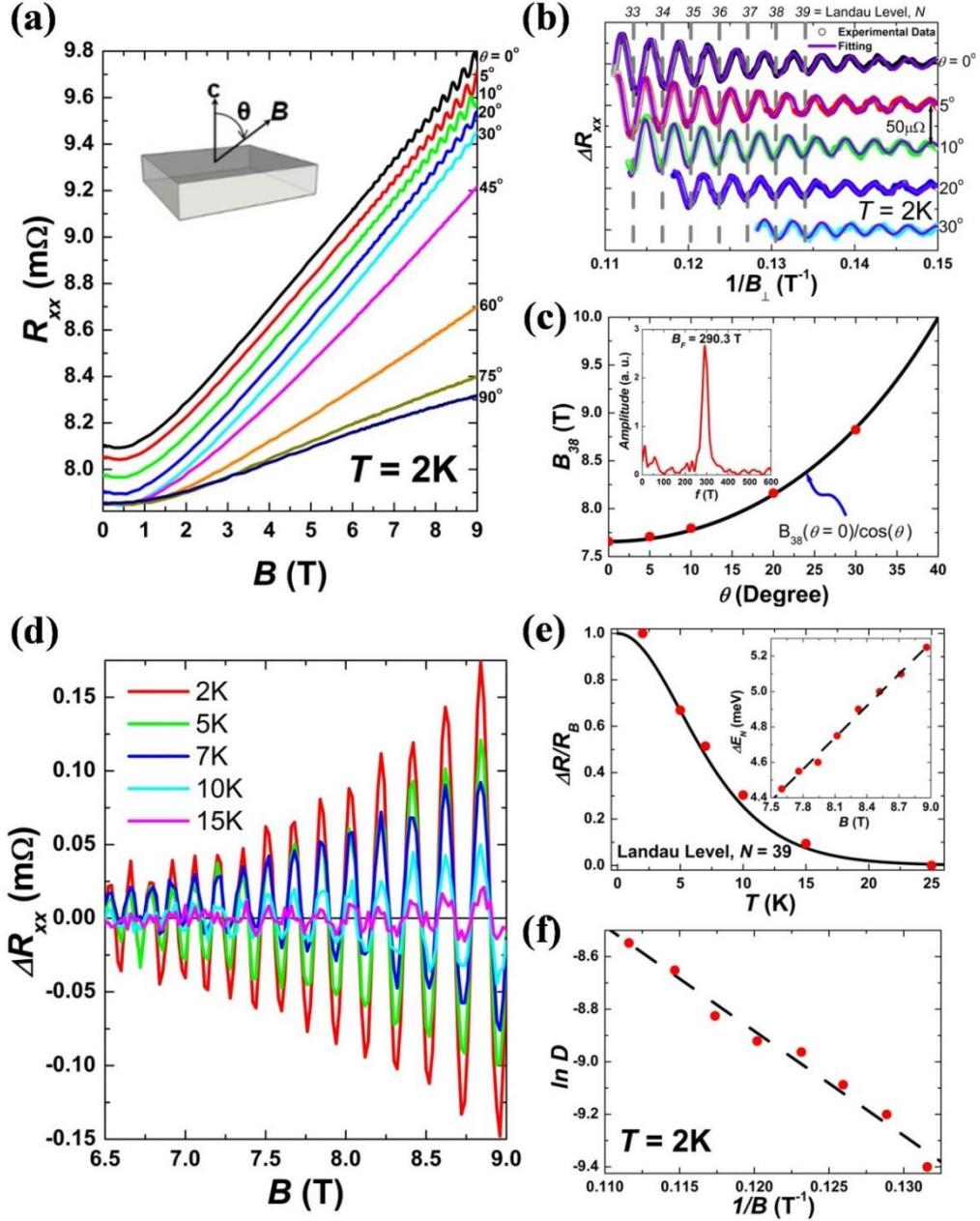
FIG. 3. (a) Magnetic field dependent longitudinal resistivity R_{xx} measurement up to 9 T at 2 K. R_{xx} traces for the tilted angles from 0° to 20° are offset for clarity. No SdHO observed for θ > 30°. (b) Inverse applied magnetic field dependence oscillatory resistance ΔR_{xx} after a subtracting of smooth polynomial background. Dash lines indicate the Landau levels index, N. SdHO are fits well by the ΔR_{xx} described in the text and the phase shift of $\beta \sim \pi$ is extracted. (c) Magnetic field position of minima in ΔR_{xx} (corresponding to 38th LL) as a function of an angle. 2D transport behavior from the charge carrier is revealed. The inset shows the fast Fourier transform (FFT) of ΔR_{xx}. (d) SdHO in ΔR_{xx} at various temperatures. (e) Temperature dependence of the relative amplitude of SdHO for the 39th LL. The inset shows the field dependence of ΔE_{N}, yielding $m^* = 0.194 m_e$. (f) Dingle temperature of 13.5 K is obtained from the Dingle plot and resulting the quantum mobility of 816 cm[2]/Vs.

acting as many parallel 2D conduction channels suggested from the quantum Hall effect (QHE) [38] measurement that shown later in the text.

From the Lifshitz-Kosevich theory, the resistance of a 2D system exhibiting SdHO can be expressed as $\Delta R_{xx}(T, B) \propto \frac{\alpha T/\Delta E_N(B)}{\sinh[\alpha T/\Delta E_N(B)]} e^{-\alpha T_D/\Delta E_N(B)}$ where $\alpha = 2\pi^2 k_B$, $\Delta E_N = \hbar eB/m^*$ is the energy gap in between LL with m^* as the effective mass and T_D is the Dingle temperature. The temperature dependent SdHO in ΔR_{xx} is shown in Fig. 3 (d). The amplitude of the quantum oscillations decreases with the increasing temperature and no oscillation is observed for temperatures beyond 25 K. From Fig. 3 (d), the relative amplitude of SdHO in ΔR_{xx} (B) as a function of temperature for the 39th LL is plotted, where $R_B = \Delta R_{xx}$ (T=2K). The result is shown in Fig. 3(e). The $\Delta R_{xx}/R_B$ is well-fitted by $\frac{\alpha T/\Delta E_N(B)}{\sinh[\alpha T/\Delta E_N(B)]}$ and therefore the fitting parameter $\Delta E_{N=39}$ is extracted. The inset of Fig. 3 (e) shows the ΔE_N for different LL. From the slope of the field dependent ΔE_N, the $m^* = 0.194 m_e$ is determined. By defining D as $\Delta RB \sinh(\alpha T/\Delta E)$, the $ln D$ as a function of inverse field is plotted and yields $T_D = 13.5$ K from its slope. Due to $T_D = \hbar/2\pi k_B \tau$ and $\mu_q = e\tau/m^*$, the corresponding quantum lifetime of carrier τ and the quantum mobility μ_q is 90 fs and 816 cm^2/Vs, respectively. It is found that μ_q is much slower than μ_{bulk} because all scattering events including small scattering takes into account on the quantum mobility, whereas the backscattering events are the main contribution for the bulk mobility. Due to the fact the lowest resolvable LL that can be accessed within the field limit is far from the quantum limit ($N = 1$), thus the LL fan diagram is not useful to determine the Berry's phase. Instead, the Berry's phase can be alternatively determined from the fitting method. The fitting equation is based on the modified Lifshitz-Kosevich formulation $\Delta R_{xx} = A \exp(-\pi/\mu_q B)\cos[2\pi(B_F/B)+\beta]$ where β is the phase shift. From the well-fitted of

ΔR_{xx} as shown in Fig. 3 (b), the $\beta \sim \pi$ implying the existence of Berry's phase π and confirms the quantum transport of surface Dirac fermions in the iron doped TIs.

Quantized plateaus in the Hall resistance R_{xy} for another sample (thinner than the samples for SdHO measurement) in Fig. 4 (a) are interpreted as QHE and are accompanied with the minima in R_{xx}. Based on the XRD measurement, the thickness of one QL is 9.5484 Å. Therefore, $1/R_{xy}$ divided by the number of QLs Z in the function of $1/B$ is plotted. The plot illustrates in Fig. 4 (b) shows the plateaus are separated by approximately 0.8 e^2/h per QL and the magnitude of the R_{xy} plateau is approximately h/NZe^2 where N is the corresponding LL index. On the other hand, several samples with thicknesses in the range of 60 µm to 130 µm also being measured. It is found that the step size $\Delta(1/R_{xy})$ per QL in between the plateaus is approximately constant and average to about 1.1 e^2/h per QL. Therefore, the observation of $\Delta(1/R_{xy})$ scales with a number of QLs Z suggests that the origin of the SdHO is from the bulk acting as many parallel 2D conduction channels and not due to the surface transport, although the quantum oscillatory phenomena show the 2D transport features.

(a)

(b)
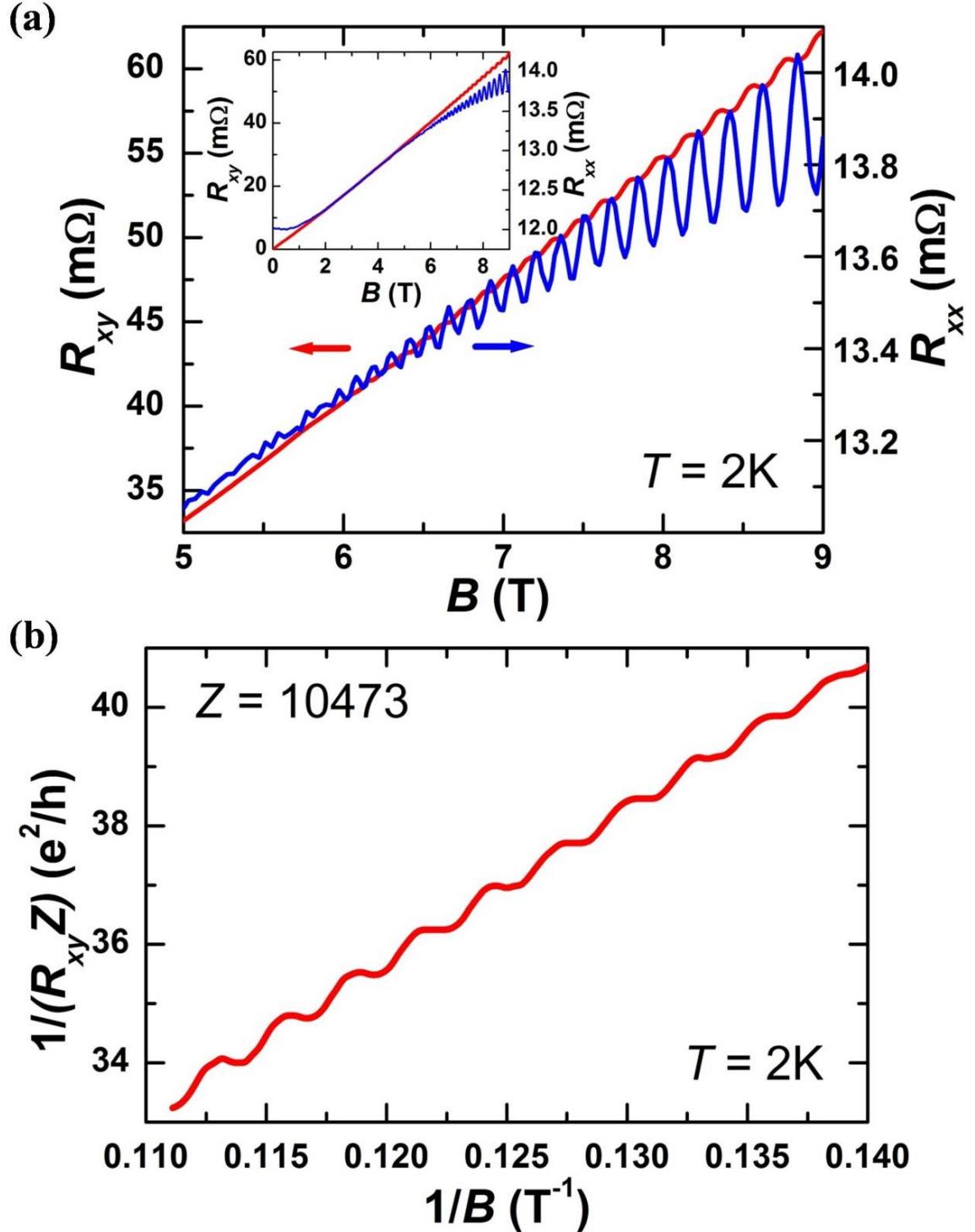
FIG. 4. (a) Magnetic field dependence of Hall resistance R_{xy} and longitudinal resistance R_{xx} for a crystal aligned with the magnetic field perpendicular to basal plane $B//c$ at 2 K. Quantized plateaus are clearly observed. (b) Inverse field dependence of $1/R_{xy}$ divided by the number of QLs, Z displaying the step size $\Delta(1/R_{xy})$ between the plateaus is approximately constant at 0.8 e^2/h per QL. It is revealed that the QHE is due to the bulk acting as many parallel 2D conduction channels.

IV. CONCLUSION

The presence of antiferromagnetic order in Fe-doped TIs did not show an opening gap in the ARPES data. In fact, the topological order coexists with a broken symmetry state. This is likely due to the S symmetry, the product of the time-reversal symmetry ϑ with the primitive-lattice translational symmetry $T_{1/2}$ in the magnetic system is preserved and leads to a $\mathbb{Z}_2$ topological invariant as proposed by Mong [38]. Since the $Fe_xBi_2Se_3$ is metamagnetic material, it is believed that the surface state can have an open gap when a magnetic field larger than 400 Oe is applied. With the transport properties established above, the capability to synthesize antiferromagnetic TIs in a controlled manner is possible. Fe-doped Bi_2Se_3 presented here performed as an attractive material to study the fundamental physics in TIs and opens up a new door for future research in order to unveil its exotic properties.

ACKNOWLEDGEMENTS

REFERENCES

[1] L. Fu, C. L. Kane, and E. J. Mele, Phys. Rev. Lett. **98**, 106803 (2007).

[2] X.-L. Qi, T. L. Hughes, and S.-C. Zhang, Phys. Rev. B **78**, 195424 (2008).

[3] D. Hsieh, Y. Xia, D. Qian, L. Wray, J. H. Dil, F. Meier, J. Osterwalder, L. Patthey, J. G. Checkelsky, N. P. Ong, A. V. Fedorov, H. Lin, A. Bansil, D. Grauer, Y. S. Hor, R. J. Cava, and M. Z. Hasan, Nature **460**, 1101 (2009).

[4] Y. L. Chen, J. G. Analytis, J.-H. Chu, Z. K. Liu, S.-K. Mo, X. L. Qi, H. J. Zhang, D. H. Lu, X. Dai, Z. Fang, S. C. Zhang, I. R. Fisher, Z. Hussain, and Z.-X. Shen, Science **325**, 178 (2009).

[5] D. Hsieh, Y. Xia, D. Qian, L. Wray, F. Meier, J. H. Dil, J. Osterwalder, L. Patthey, A. V Fedorov, H. Lin, A. Bansil, D. Grauer, Y. S. Hor, R. J. Cava, and M. Z. Hasan, Phys. Rev. Lett. **103**, 146401 (2009).

[6] J. E. Moore, Nature **464**, 194 (2010).

[7] X.-L. Qi, R. Li, J. Zang, and S.-C. Zhang, Science **323**, 1184 (2009).

[8] F. Wilczek, Phys. Rev. Lett. **58**, 1799 (1987).

[9] J. Wang, B. Lian, and S.-C. Zhang, Phys. Rev. B **93**, 45115 (2016).

[10] A. Karch, Phys. Rev. Lett. **103**, 171601 (2009).

[11] R. Li, J. Wang, X.-L. Qi, and S.-C. Zhang, Nat. Phys. **6**, 284 (2010).

[12] T. Yokoyama, Y. Tanaka, and N. Nagaosa, Phys. Rev. B **81**, 121401(R) (2010).

[13] R. Yu, W. Zhang, H.-J. Zhang, S.-C. Zhang, X. Dai, and Z. Fang, Science **329**, 61 (2010).

[14] C.-Z. Chang, J. Zhang, X. Feng, J. Shen, Z. Zhang, M. Guo, K. Li, Y. Ou, P. Wei, L.-L. Wang, Z.-Q. Ji, Y. Feng, S. Ji, X. Chen, J. Jia, X. Dai, Z. Fang, S.-C. Zhang, K. He, Y. Wang, L. Lu, X.-C. Ma, and Q.-K. Xue, Science **340**, 167 (2013).

[15] C.-Z. Chang, W. Zhao, D. Y. Kim, H. Zhang, B. A. Assaf, D. Heiman, S.-C. Zhang, C. Liu, M. H. W. Chan, and J. S. Moodera, Nat. Mater. **14**, 473 (2015).

[16] L. A. Wray, S.-Y. Xu, Y. Xia, D. Hsieh, A. V Fedorov, Y. S. Hor, R. J. Cava, A. Bansil, H. Lin, and M. Zahid Hasan, Nat. Phys. **7**, 32 (2010).

[17] Y. L. Chen, J.-H. Chu, J. G. Analytis, Z. K. Liu, K. Igarashi, H.-H. Kuo, X. L. Qi, S. K. Mo, R. G. Moore, D. H. Lu, M. Hashimoto, T. Sasagawa, S. C. Zhang, I. R. Fisher, Z. Hussain, and Z. X. Shen, Science **329**, 659 (2010).

[18]   J. Zhang, J. P. Velev, X. Dang, and E. Y. Tsymbal, Phys. Rev. B **94**, 014435 (2016).

[19]   R. S. K. Mong, A. M. Essin, and J. E. Moore, Phys. Rev. B **81**, 245209 (2010).

[20]   C. Fang, M. J. Gilbert, and B. A. Bernevig, Phys. Rev. B **88**, 85406 (2013).

[21]   P. Baireuther, J. M. Edge, I. C. Fulga, C. W. J. Beenakker, and J. Tworzydlo, Phys. Rev. B **89**, 35410 (2014).

[22]   C.-X. Liu, E-Print arXiv **1304.6455**, (2013).

[23]   A. R. Mellnik, J. S. Lee, A. Richardella, J. L. Grab, P. J. Mintun, M. H. Fischer, A. Vaezi, A. Manchon, E.-A. Kim, N. Samarth, and D. C. Ralph, Nature **511**, 449 (2014).

[24]   S. Ghosh and A. Manchon, Phys. Rev. B **95**, 35422 (2017).

[25]   T. Jungwirth, X. Marti, P. Wadley, and J. Wunderlich, Nat. Nanotechnol. **11**, 231 (2016).

[26]   O. Gomonay, T. Jungwirth, and J. Sinova, Phys. Status Solidi - Rapid Res. Lett. **11**, 1700022 (2017).

[27]   A. Sekine and T. Chiba, AIP Adv. **7**, 55902 (2017).

[28]   L. Smejkal, T. Jungwirth, and J. Sinova, Phys. Status Solidi - Rapid Res. Lett. **11**, 1700044 (2017).

[29]   Y. Xia, D. Qian, D. Hsieh, L. Wray, A. Pal, H. Lin, A. Bansil, D. Grauer, Y. S. Hor, R. J. Cava, and M. Z. Hasan, Nat. Phys. **5**, 398 (2009).

[30]   H. Zhang, C.-X. Liu, X.-L. Qi, X. Dai, Z. Fang, and S.-C. Zhang, Nat. Phys. **5**, 438 (2009).

[31]   S. Kim, M. Ye, K. Kuroda, Y. Yamada, E. E. Krasovskii, E. V. Chulkov, K. Miyamoto, M. Nakatake, T. Okuda, Y. Ueda, K. Shimada, H. Namatame, M. Taniguchi, and A. Kimura, Phys. Rev. Lett. **107**, 56803 (2011).

[32]   Y. S. Hor, A. Richardella, P. Roushan, Y. Xia, J. G. Checkelsky, A. Yazdani, M. Z. Hasan, N. P. Ong, and R. J. Cava, Phys. Rev. B **79**, 195208 (2009).

[33]   Y. Okada, C. Dhital, W. Zhou, E. D. Huemiller, H. Lin, S. Basak, A. Bansil, Y.-B. Huang, H. Ding, Z. Wang, S. D. Wilson, and V. Madhavan, Phys. Rev. Lett. **106**, 206805 (2011).

[34]   T. Schlenk, M. Bianchi, M. Koleini, A. Eich, O. Pietzsch, T. O. Wehling, T. Frauenheim, A. Balatsky, J.-L. Mi, B. B. Iversen, J. Wiebe, A. A. Khajetoorians, P. Hofmann, and R. Wiesendanger, Phys. Rev. Lett. **110**, 126804 (2013).

[35]   C.-L. Song, Y.-P. Jiang, Y.-L. Wang, Z. Li, L. Wang, K. He, X. Chen, X.-C. Ma, and Q.-K. Xue, Phys. Rev. B **86**, 45441 (2012).

[36]   Y. S. Hor, P. Roushan, H. Beidenkopf, J. Seo, D. Qu, J. G. Checkelsky, L. A. Wray, D. Hsieh, Y. Xia, S.-Y. Xu, D. Qian, M. Z. Hasan, N. P. Ong, A. Yazdani, and R. J. Cava, Phys. Rev. B **81**, 195203 (2010).

[37]   Chun-Rong Lin, Yu-Jhan Siao, Shin-Zong Lu, and Chie Gau, IEEE Trans. Magn. **45**, 4275 (2009).

[38]   H. Cao, J. Tian, I. Miotkowski, T. Shen, J. Hu, S. Qiao, and Y. P. Chen, Phys. Rev. Lett. **108**, 216803 (2012).

II. MULTILAYERED QUANTUM HALL EFFECT IN PARAMAGNETIC ORDERED TOPOLOGICAL INSULATOR Mn$_x$Bi$_2$Se$_3$

Seng Huat Lee[1], Stephen Kraus[1], Jixia Dai[2], Weida Wu[2] and Yew San Hor[1]

[1]*Department of Physics, Missouri University of Science and Technology, Rolla, MO 65409*

[2]*Department of Physics and Astronomy, Rutgers University, Piscataway, NJ 08854*

ABSTRACT

Intercalation of manganese into the van der Waals gaps between the topological insulator Bi$_2$Se$_3$ quintuple layers has achieved by using the modified Bridgman method and leads the system to possess paramagnetism behavior. Angle-resolved photoemission spectroscopy verifies the existence of topological surface states in the magnetic topological insulator but does not show the opened surface gap associated with ferromagnetic ordering. Quantum oscillations of Shubnikov-de Haas oscillations are observed from the longitudinal magnetotransport measurement. The quantum mobility of the carriers and the phase shift are extracted, which are 750 cm^2/Vs and 1.2 π, respectively. The phase shift near π reveals the existence of Dirac fermions in this system. The observation of quintuple layer dependent quantum Hall effect reveals the electronic transport is not due to the surface but from bulk acts as multilayered 2D conduction channels.

I. INTRODUCTION

Topological insulators (TIs) have attracted tremendous interest in condensed matter physics since their relatively recent experimental discovery[1–11]. These materials are unique in that they behave as insulators in bulk, yet have conductive surface states that possess spin-momentum locking Dirac fermions. The existence and properties of these surface states are closely tied to their obedience to time-reversal symmetry (TRS). Unlike transport properties in commercial semiconductors, backscattering is prohibited in TIs because of the unique spin transport on the surface. Several theories predict interesting new physics related to the alteration of these surface states and the breaking of TRS[12–17]. Under the influence of magnetic ordering, the TRS of TI surface states is broken. This corresponds to the opening of a measurable band gap in these surface states as well as the formation of interesting unique quantum properties[14,18–25]. For example, quantum anomalous Hall effect has been theoretically predicted and experimentally demonstrated[20,21]. Theories also predicted that an image magnetic monopole may be induced in the presence of a charged particle near to the surface. Hence, the properties of the magnetically doped topological insulator promise novel physics and thus is receiving much attention in condensed matter physics.

One can produce such the novel materials by depositing thin films of transition metals on TIs' surface[12,17,26,27], or by chemical doping in TIs[25,28]. Intercalation of copper in between Bi_2Se_3 quintuple layers has successfully induced superconductivity at a temperature below 3.8 K[29]. This approach has stimulated research on doping TIs with other transition metal elements. The physical properties of Mn-doped Bi_2Se_3, either by intercalation or substitution into the bulk, has been investigated earlier. However, no strong evidence shows that the Mn ion is intercalated into the Bi_2Se_3 system. For the

Shubnikov-de Haas oscillation (SdHO) in the field-dependent longitudinal resistivity, it was only observed in the 0.07 Mn concentration[30]. Furthermore, quantum Hall effect (QHE), a consequence of the formation of Landau levels under strong external magnetic fields that usually accompanied with the SdHO has not been reported in Mn-doped Bi_2Se_3 system.

In this context, we report the magnetism, electronic transport properties, and the SdHO accompanied by the QHE on $Mn_xBi_2Se_3$ system in a wide nominal range ($0 \leq x \leq 0.20$). It shows paramagnetism below 25 K. From the ARPES data, the surface states are coexistence with the magnetic order and no opening surface gap is observed. The observation of Shubnikov-de Haas oscillations in longitudinal magnetotransport measurement reveals the existence of Dirac fermions in this system due to the elucidation of the π Berry's phase from the quantum oscillations. We also demonstrated that the QHE is scaled with the thickness of the sample that attributed by each quintuple layer of Bi_2Se_3 that gives rise to the multilayered quantum Hall state.

II. CRYSTALS GROWTH AND EXPERIMENTAL METHODS

High-quality single crystals of $Mn_xBi_2Se_3$ were grown by modified Bridgman method. The stoichiometric mixtures of high purity of manganese, bismuth, and selenium were heated to 950 °C for 24 hours in evacuated quartz tubes. The melts were stirred at this temperature and then furnace cooled to 550 °C for annealing process. These crystalline samples were quenched in water after 24 hours at the temperature of 550 °C. Since Mn element is highly reactive with the quartz, the Mn concentration is limited to 20% or below. The resultant ingot was easily cleaved to obtain single crystals for the measurements. Phase structure analysis and its chemistry defects were studied by the XRD and STM. In the STM

studied, the clean surface was obtained by in-situ cleaving under UHV condition ($\sim 10^{-11}$ torr) at room temperature. Angle-resolved photoemission spectroscopy (ARPES) measurements at 12 K were conducted at Synchrotron Radiation Centre, University of Wisconsin, Madison. The samples for ARPES were cleaved at ultrahigh vacuum environment to expose a pristine surface. Quantum Design Physical Property Measurement System (PPMS) was employed to perform the magnetization, resistivity and magnetotransport measurements. The standard four-point probe technique with silver paste cured at room temperature was used for the longitudinal resistivity measurement while the standard five-point probe technique was employed for the transverse magnetotransport measurement. All the electric current was applied in the basal plane of the crystals.

III. RESULTS AND DISCUSSION

Crystal structure and its defect were determined from the XRD and STM studies. The XRD scan of the basal plane reflections from a single crystal of Mn-doped Bi_2Se_3 revealed that Mn has been intercalated into Bi_2Se_3 and the crystal has rhombohedral $R\bar{3}m$ crystal structure which is very similar to that of Bi_2Se_3. There are some minority secondary phases BiSe and $MnSe_2$ are also being identified. The crystallography c-lattice parameter is slightly increased from 28.545(8) Å for Bi_2Se_3 to 28.639(8) Å for $Mn_{0.10}Bi_2Se_3$, for example, as shown in Fig. 1. This suggests that the Mn atoms are intercalated in between the Bi_2Se_3 quintuple layer and lead to the increasing of the lattice constant c, as observed on the previous studies of Cu intercalation into Bi_2Se_3. From the scanning tunneling microscopy studied on the (001) surface of the cleaved Mn-doped Bi_2Se_3, several distinct features are identified. Bias-independent of bright protrusions on Fig. 2 (a) and (b) are clearly observed. The magnified image of the bright protrusion is shown in the inset of

Fig. 2 (a). This indicates that these features are formed from the atom above the cleaved surface (adatoms defect) and likely correspond to the intercalated of Mn cluster, as these protrusions are absent in the parent compound of Bi_2Se_3. However, the dark features in the both Fig. 2 (a) and (b) can be due to the substitution of Bi site with Mn. Inset of Fig. 2 (b) is the magnified view of the dark feature. From the XRD and STM studies, it is revealed that Mn atoms are significantly intercalated in between the Bi_2Se_3 quintuple layers by using the modified Bridgman method although partial substitution of the Mn ion onto the Bi site also occurred. This conclusion is contradicted with the observation from ref. 31, in the polycrystalline pressed pellet of $Mn_xBi_2Se_3$, where mostly all of the Mn are substituted onto the Bi site.
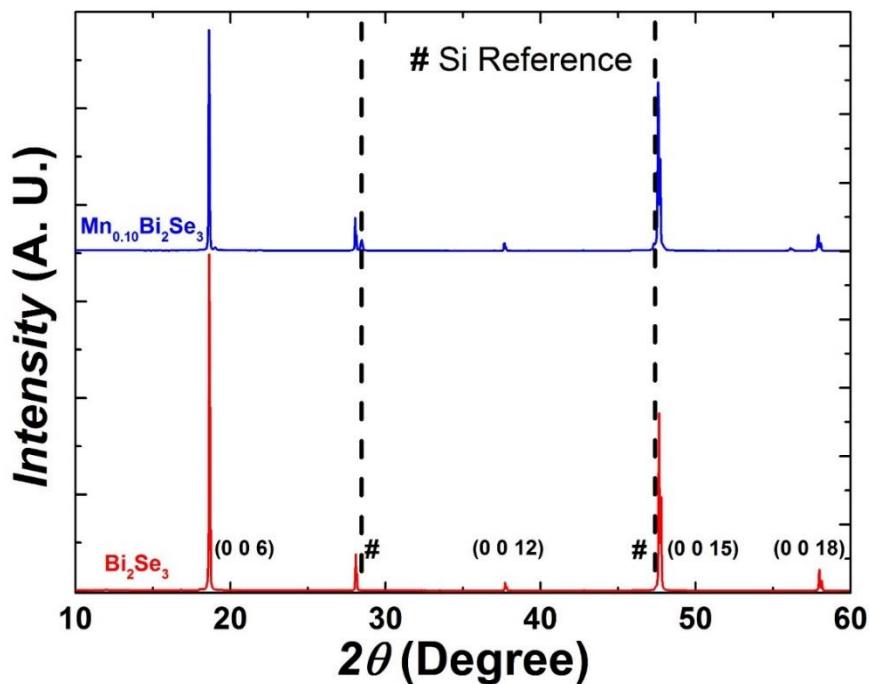
FIG. 1. Comparison of the reflected XRD peaks between the host compound Bi_2Se_3 and Mn-doped Bi_2Se_3 with Si peaks serve as the reference. The XRD peaks of Mn-doped Bi_2Se_3 are shifted to the left, suggesting the increased of the c-lattice parameter.
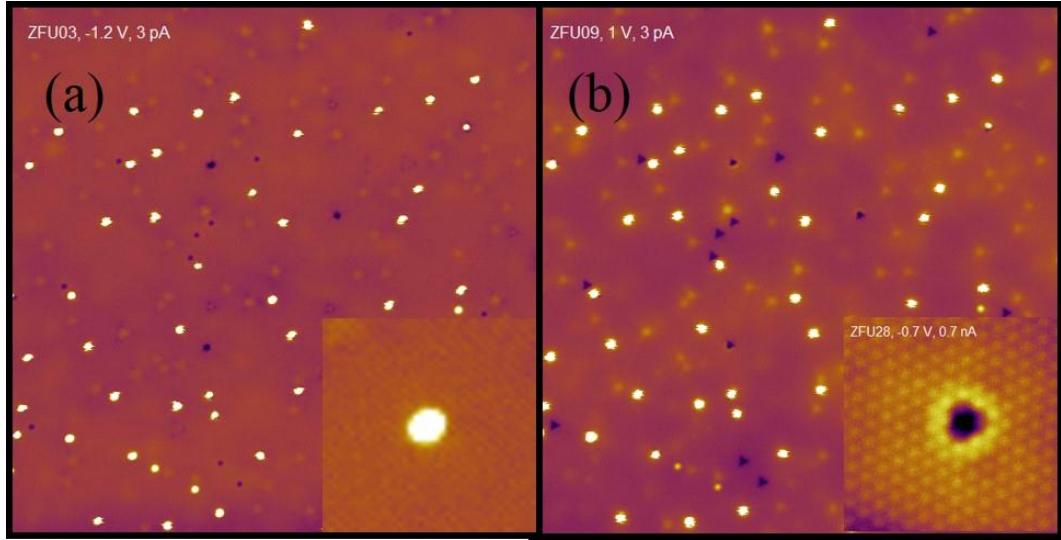
FIG. 2. STM topographic images on 160×160 μm^2 area showing the (a) filled stated at a bias voltage of -1.2 V and (b) unfilled stated at a bias voltage of +1.0 V. The inset of (a) and (b) show the bias-independence of bright protrusions and the Mn-substituted on Bi site, respectively.

The temperature dependent magnetic susceptibilities of $Mn_xBi_2Se_3$ with different nominal x values were measured in an applied magnetic field of 5 kOe perpendicular to the basal plane $B//c$. The data shown in Fig. 3 is subtracted from the temperature-independent term χ_o. The weak diamagnetism is observed as the magnetic susceptibility is in the negative region at high temperatures for the concentration of Mn lower than 0.15. Fig. 3 has revealed the weakness of the paramagnetic contribution from the Mn which becomes significant at low temperatures. The paramagnetic behavior occurs in the magnetic TIs with the concentrations of Mn higher than 0.10 at very low temperatures, starting as high as 25 K. It is consistent with paramagnetic in the STS study that there is no zero bias feature around the Mn dopant. Fig. 3 also indicates a possible ferromagnetic transition in these materials at very low temperatures but this is not conclusive. With the increase of Mn doping, the bulk of the magnetic TIs crystals might become too metallic, thus losing its

desired TI properties. In order to verify this, resistivity measurements were conducted. Fig. 4 illustrates the resistivity results. The resistivity of these materials is decreased along with the Mn doping and exhibits a metallic behavior which is consistent with Mn acting as an electron donor.
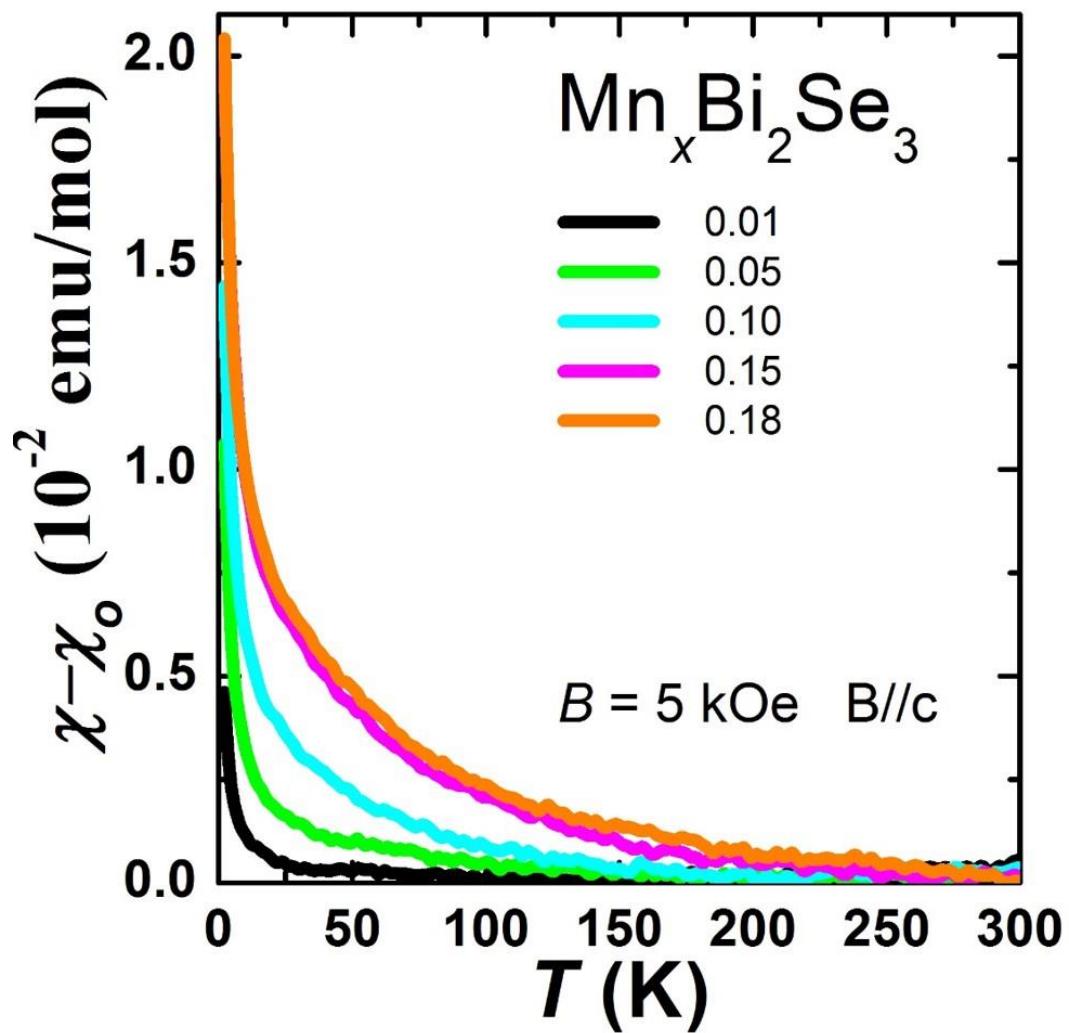
FIG. 3. Temperature-dependent magnetic susceptibility χ measured at 5 kOe for the crystal aligned with the magnetic field perpendicular to the basal plane $B//c$. The ground state of the Mn-doped crystals is paramagnetic.
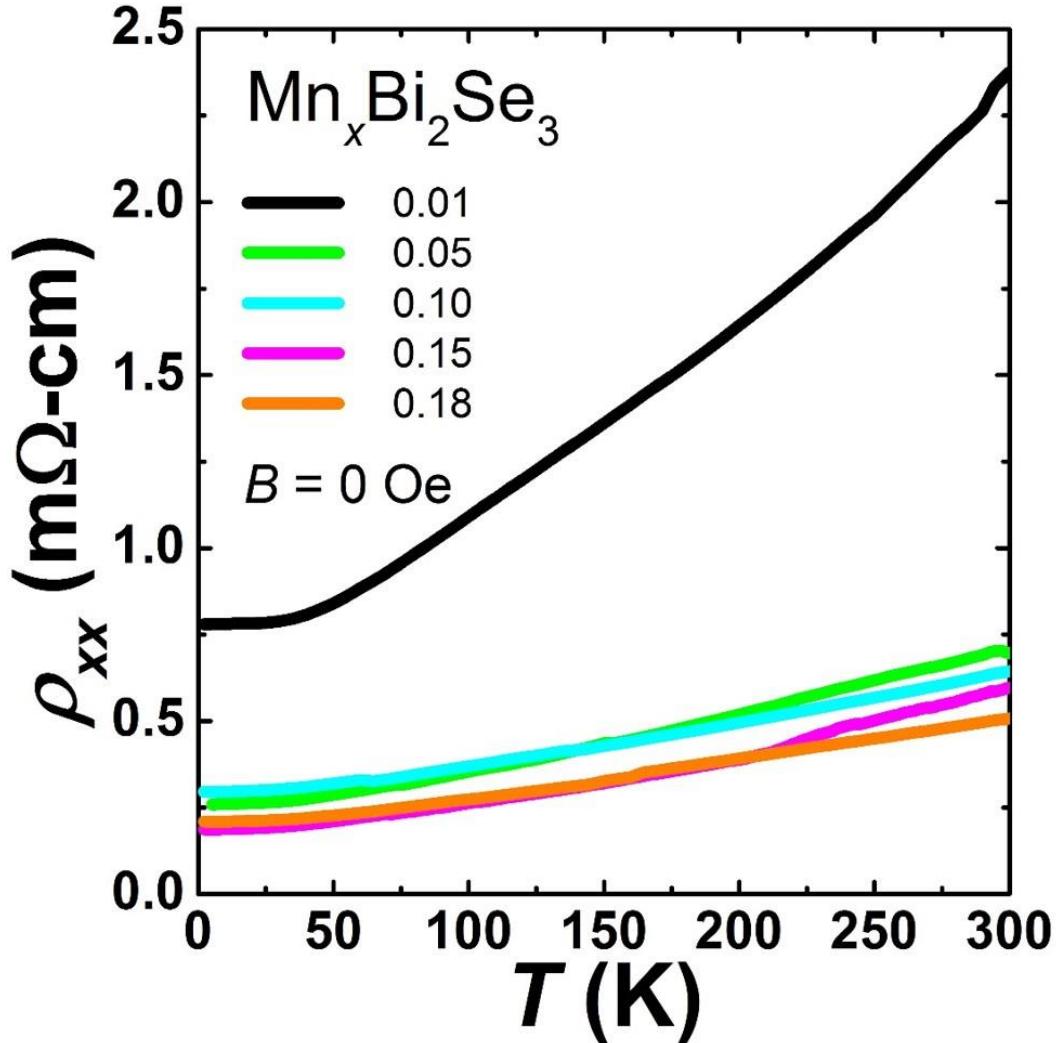
FIG. 4. Resistivity as a function of temperature. All Mn-doped Bi₂Se₃ exhibits a metallic behavior.

According to the theoretical study, a gap is expected to exist in the surface states if magnetic impurities are introduced into the system. The ARPES measurements, however, confirm that the magnetic TI coexistence with topological surface states without energy gap opening for Mn doping into the Bi_2Se_3 due to symmetry property of paramagnetism. ARPES data along the $\overline{M} - \overline{\Gamma} - \overline{M}$ momentum space is shown in Fig. 5. The parent compound, Bi_2Se_3 shows a Dirac surface state with the Dirac point lying about 0.15 eV

below the Fermi level (FL). Compared with the published ARPES data of Bi_2Se_3[32], our Bi_2Se_3 shows semiconducting behavior where the FL lies in the bulk band gap as shown in Fig. 5 (b). Manganese doped Bi_2Se_3 does not destroy the surface state. Even up to 20% doping of Mn in the compound, the surface state of Dirac cone is still observed. With the increasing of the Mn concentration, the FL is moving to the bulk conduction band (BCB) making the compound more conductive, in agreement with the resistivity data. The presence of magnetic order in Mn doped TIs did not show an opening gap in the ARPES data, this is likely due to the fact that the ARPES data can only be taken at a minimum temperature of 12 K. At this relatively high temperature, the Mn-doped Bi_2Se_3 is paramagnetic and does not break the time-reversal symmetry.

Quantum oscillations in longitudinal magnetoresistance measurement, R_{xx} under the applied magnetic field higher than 6 T at a temperature of 2 K were also observed. These quantum oscillations in magnetoresistance are called Shubnikov-de Haas oscillations (SdHO). The results are shown in the inset of Fig. 7 (a). From the observation of SdHO, Fermi surface of the $Mn_xBi_2Se_3$ electronic band structure can be mapped. In Fig. 6 (a), the oscillatory longitudinal magnetoresistance ΔR_{xx} as a function of inverse field $1/B$ was plotted. From the Fourier transform of ΔR_{xx} $(1/B)$, a well-resolved peak at $B_F = 306.0T$ was observed. The result is shown in Fig. 6 (b). Based on the Onsager relation $B_F = \hbar A/2\pi e$, the Fermi wave vector $k_F = 0.0964$ Å is determined by assuming the Fermi surface is a circular shape. This k_F value is consistent with the value obtained in the ARPES data. The 2D carrier density, $n_{2D} = eB_F/h$ can also be extracted by using the B_F obtained above. Therefore, the n_{2D} is 6.96×10^{12} cm^{-2} per spin. By using the B_F/B, where the B is the magnetic field position of each ΔR_{xx} minimum, values close to the
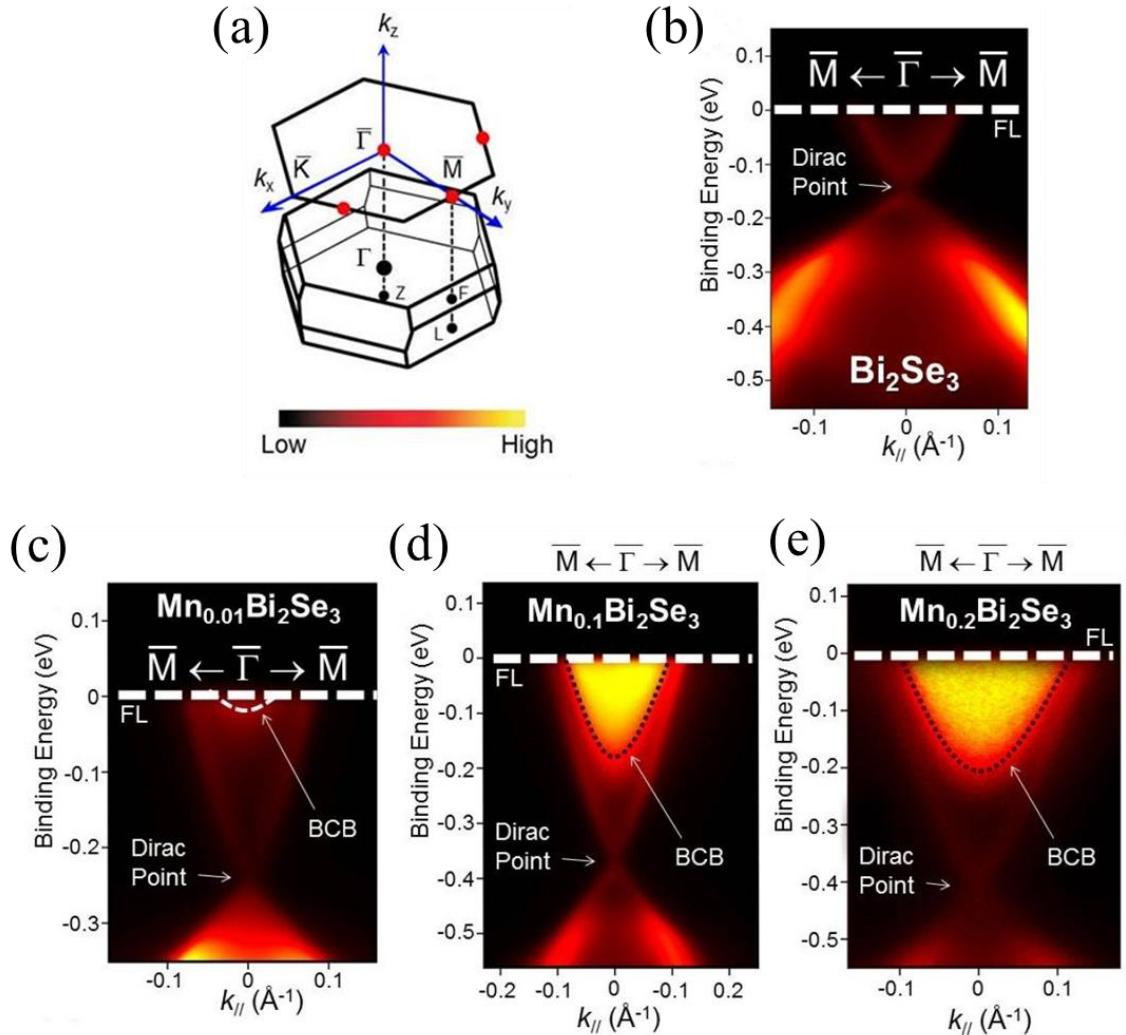
FIG. 5. ARPES data of Mn-doped Bi_2Se_3. A schematic diagram of bulk 3D Brillouin zone (BZ) of Bi_2Se_3 crystals and the 2D BZ of the projected (111) surface. (b) ARPES data taken for a Bi_2Se_3 crystal at 12 K. The Dirac point located roughly 0.15 eV below the Fermi level (FL). The FL lying in the band gap indicates that the Bi_2Se_3 is a nearly-perfect topological insulator. (c), (d) and (e) ARPES data of $Mn_xBi_2Se_3$ for different nominal x values. FL in Mn intercalated Bi_2Se_3 lies in the bulk conduction band. With the increasing of Mn doping concentration, the Dirac point is dramatically moved away from the FL.
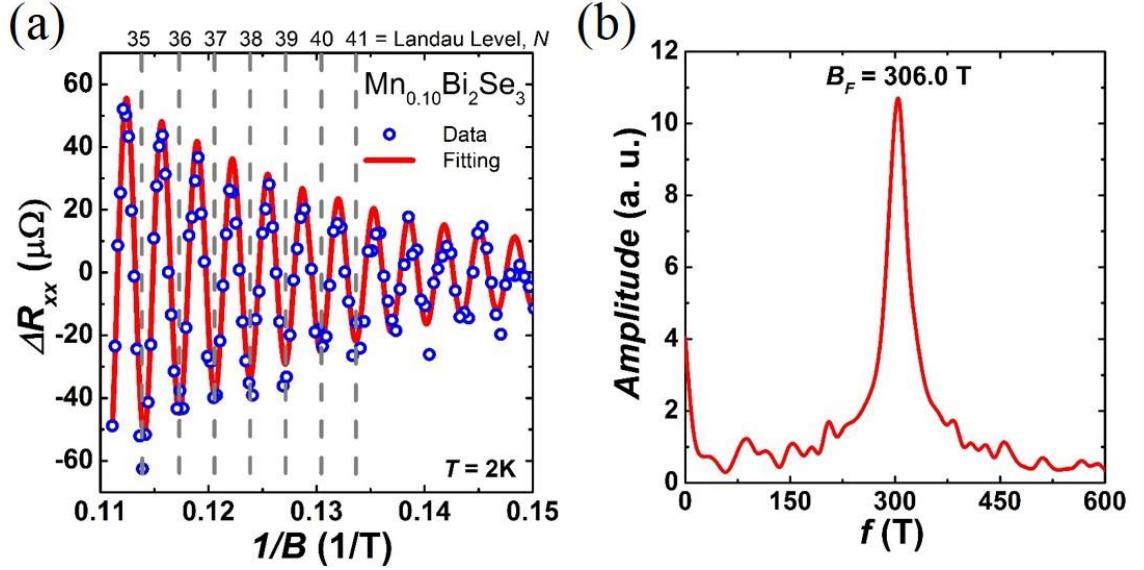
FIG. 6. (a) Shubnikov-de Haas oscillation of Mn-doped Bi_2Se_3. Inverse applied magnetic field dependent oscillatory resistance ΔR_{xx} for $Mn_{0.10}Bi_2Se_3$ after a subtracting of smooth polynomial background. Dash lines indicate the LL index N. The experimental data is well-fitted by the ΔR_{xx} described in the text and the phase shift of $\beta \sim \pi$ is extracted. (b) Fourier transform of ΔR_{xx} $(1/B)$. A well-resolved peak at $B_F = 306.0$ T was obtained.
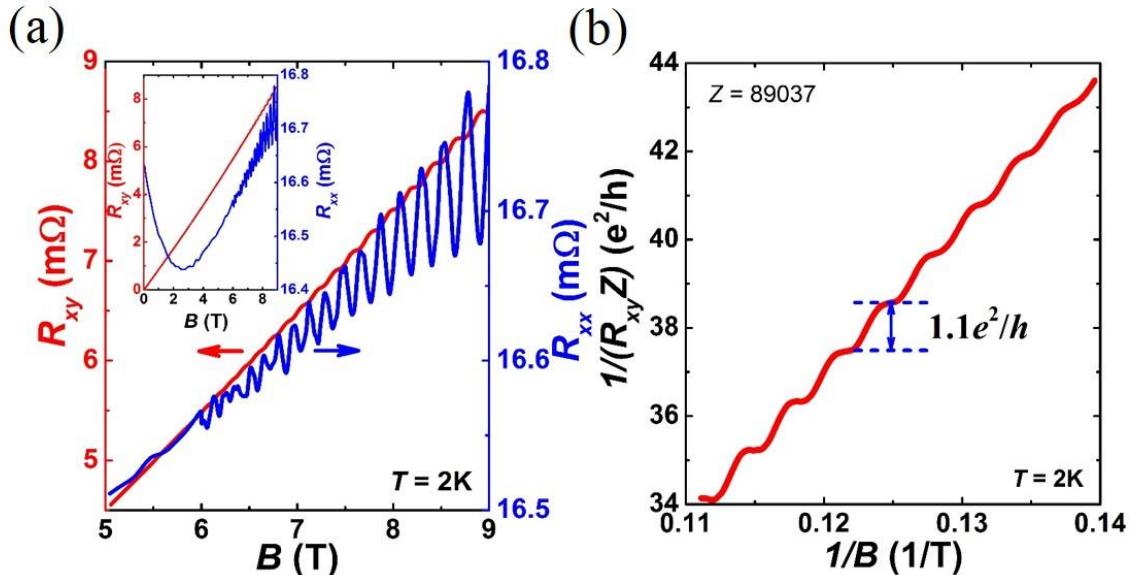
FIG. 7. (a) Longitudinal resistance R_{xx} and Hall resistance R_{yx} as a function of the applied magnetic field that perpendicular to the basal plane $B//c$ at 2 K. Quantized plateaus in the R_{yx} are accompanied with the minima in R_{xx}. (b) $1/ZR_{yx}$ as the function of inverse field. The step size $\Delta(1/R_{xy})$ between the plateaus is approximately constant at $1.1e^2/h$ per QL.

integers N corresponding to the Landau levels (LL) were obtained. The dashed lines in Fig. 6 (a) represent the LL index N. Due to the lowest resolvable LL that can be accessed within the field limit is far from the quantum limit ($N = 1$), Berry's phase is determined from the fitting method based on the Lifshitz-Kosevich formulation. The plot of ΔR_{xx} ($1/B$) in Fig. 6(a) is well-fitted by the Lifshitz-Kosevich formulation $\Delta R_{xx} = A \exp(-\pi/\mu_q B)\cos[2\pi(B_F/B)+\beta]$ with 1.2π phase shift for β. The phase shift near π reveals the existence of Dirac fermions on the surface states of this system. Besides, the fitting parameter of the carrier's quantum mobility can be extracted. From the well-fitted of ΔR_{xx} ($1/B$), the quantum mobility of the carriers is 750 cm^2/Vs.

Quantized plateaus like structure at 2 K in the Hall resistance R_{yx} is clearly observed. In Fig. 7 (a), these quantized plateaus are interpreted as quantum Hall effect (QHE) and the position of which nicely correspond to the minima in R_{xx}. Fig. 7 (b) shows the Hall conductance $1/R_{yx}$ divided by the number of quintuple layer Z as the function of inverse field. The determination of Z is that the thickness of the measured sample divided by the thickness of one quintuple layer of Mn-doped Bi$_2$Se$_3$ that obtained from the XRD result. In Fig. 7 (b), the plateaus are separated by approximately 1.1 e^2/h per QL and the magnitude of the R_{yx} plateau is approximately h/NZe^2, where N is the corresponding LL index. The same finding is also observed for several samples with thicknesses in the range of 60 μm to 110 μm. The step size between the consecutive plateaus in $1/R_{yx}$ scales with Z number suggesting the observed QHE in this magnetic topological insulator is attributable to the bulk acting as multilayered QHE instead of from the surface transport.

IV. CONCLUSION

Manganese has been successfully intercalated into the van der Waal gap of Bi_2Se_3 by using the modified Bridgman method. From the magnetic susceptibility measurement as a function of temperature, paramagnetism has been induced into Bi_2Se_3. In the ARPES data, the surface states of the Mn-doped Bi_2Se_3 system remain present. This is due to the Mn-doped TIs is paramagnetic when the ARPES measurement is taken at the minimum temperature of 12 K. The observation of SdHO reveals the existence of π Berry's phase from the well fitted ΔR_{xx} and confirms the quantum transport of surface Dirac fermions in the Mn-doped TIs. However, the observation of the thickness dependent quantum Hall effect, suggesting each quintuple layer of Bi_2Se_3 acts as 2D conduction channels and not due to the surface transport.

REFERENCES

[1] L. Fu, C.L. Kane, and E.J. Mele, Phys. Rev. Lett. **98**, 106803 (2007).

[2] X.-L. Qi, T.L. Hughes, and S.-C. Zhang, Phys. Rev. B **78**, 195424 (2008).

[3] J.E. Moore, Nature **464**, 194 (2010).

[4] M.Z. Hasan and C.L. Kane, Rev. Mod. Phys. **82**, 3045 (2010).

[5] X.-L. Qi and S.-C. Zhang, Rev. Mod. Phys. **83**, 1057 (2011).

[6] Y. Ando, J. Phys. Soc. Japan **82**, 102001 (2013).

[7] D. Hsieh, Y. Xia, D. Qian, L. Wray, J.H. Dil, F. Meier, J. Osterwalder, L. Patthey, J.G. Checkelsky, N.P. Ong, A. V. Fedorov, H. Lin, A. Bansil, D. Grauer, Y.S. Hor, R.J. Cava, and M.Z. Hasan, Nature **460**, 1101 (2009).

[8] Y.L. Chen, J.G. Analytis, J.-H. Chu, Z.K. Liu, S.-K. Mo, X.L. Qi, H.J. Zhang, D.H. Lu, X. Dai, Z. Fang, S.C. Zhang, I.R. Fisher, Z. Hussain, and Z.-X. Shen, Science **325**, 178 (2009).

[9] D. Hsieh, Y. Xia, D. Qian, L. Wray, F. Meier, J.H. Dil, J. Osterwalder, L. Patthey, A. V Fedorov, H. Lin, A. Bansil, D. Grauer, Y.S. Hor, R.J. Cava, and M.Z. Hasan, Phys. Rev. Lett. **103**, 146401 (2009).

[10] S. Kim, M. Ye, K. Kuroda, Y. Yamada, E.E. Krasovskii, E. V. Chulkov, K. Miyamoto, M. Nakatake, T. Okuda, Y. Ueda, K. Shimada, H. Namatame, M. Taniguchi, and A. Kimura, Phys. Rev. Lett. **107**, 56803 (2011).

[11] H. Zhang, C.-X. Liu, X.-L. Qi, X. Dai, Z. Fang, and S.-C. Zhang, Nat. Phys. **5**, 438 (2009).

[12] L.A. Wray, S.-Y. Xu, Y. Xia, D. Hsieh, A. V Fedorov, Y.S. Hor, R.J. Cava, A. Bansil, H. Lin, and M. Zahid Hasan, Nat. Phys. **7**, 32 (2011).

[13] Y.L. Chen, J.-H. Chu, J.G. Analytis, Z.K. Liu, K. Igarashi, H.-H. Kuo, X.L. Qi, S.K. Mo, R.G. Moore, D.H. Lu, M. Hashimoto, T. Sasagawa, S.C. Zhang, I.R. Fisher, Z. Hussain, and Z.X. Shen, Science **329**, 659 (2010).

[14] X.-L. Qi, R. Li, J. Zang, and S.-C. Zhang, Science **323**, 1184 (2009).

[15] Y. Okada, C. Dhital, W. Zhou, E.D. Huemiller, H. Lin, S. Basak, A. Bansil, Y.-B. Huang, H. Ding, Z. Wang, S.D. Wilson, and V. Madhavan, Phys. Rev. Lett. **106**, 206805 (2011).

[16] J. Zhang, C.-Z. Chang, P. Tang, Z. Zhang, X. Feng, K. Li, L. Wang, X. Chen, C. Liu, W. Duan, K. He, Q.-K. Xue, X. Ma, and Y. Wang, Science **339**, 1582 (2013).

17 T. Schlenk, M. Bianchi, M. Koleini, A. Eich, O. Pietzsch, T.O. Wehling, T. Frauenheim, A. Balatsky, J.-L. Mi, B.B. Iversen, J. Wiebe, A.A. Khajetoorians, P. Hofmann, and R. Wiesendanger, Phys. Rev. Lett. **110**, 126804 (2013).

18 T. Yokoyama, Y. Tanaka, and N. Nagaosa, Phys. Rev. B **81**, 121401(R) (2010).

19 R. Yu, W. Zhang, H.-J. Zhang, S.-C. Zhang, X. Dai, and Z. Fang, Science **329**, 61 (2010).

20 C.-Z. Chang, J. Zhang, X. Feng, J. Shen, Z. Zhang, M. Guo, K. Li, Y. Ou, P. Wei, L.-L. Wang, Z.-Q. Ji, Y. Feng, S. Ji, X. Chen, J. Jia, X. Dai, Z. Fang, S.-C. Zhang, K. He, Y. Wang, L. Lu, X.-C. Ma, and Q.-K. Xue, Science **340**, 167 (2013).

21 C.-Z. Chang, W. Zhao, D.Y. Kim, H. Zhang, B.A. Assaf, D. Heiman, S.-C. Zhang, C. Liu, M.H.W. Chan, and J.S. Moodera, Nat. Mater. **14**, 473 (2015).

22 X. Kou, S.-T. Guo, Y. Fan, L. Pan, M. Lang, Y. Jiang, Q. Shao, T. Nie, K. Murata, J. Tang, Y. Wang, L. He, T.-K. Lee, W.-L. Lee, and K.L. Wang, Phys. Rev. Lett. **113**, 137201 (2014).

23 J.G. Checkelsky, R. Yoshimi, A. Tsukazaki, K.S. Takahashi, Y. Kozuka, J. Falson, M. Kawasaki, and Y. Tokura, Nat. Phys. **10**, 731 (2014).

24 G. Xu, J. Wang, C. Felser, X.-L. Qi, and S.-C. Zhang, Nano Lett. **15**, 2019 (2015).

25 C.-Z. Chang and M. Li, J. Phys. Condens. Matter **28**, 123002 (2016).

26 M.R. Scholz, J. Sánchez-Barriga, D. Marchenko, A. Varykhalov, A. Volykhov, L. V. Yashina, and O. Rader, Phys. Rev. Lett. **108**, 256810 (2012).

27 T. Valla, Z.-H. Pan, D. Gardner, Y.S. Lee, and S. Chu, Phys. Rev. Lett. **108**, 117601 (2012).

28 Y.S. Hor, P. Roushan, H. Beidenkopf, J. Seo, D. Qu, J.G. Checkelsky, L.A. Wray, D. Hsieh, Y. Xia, S.-Y. Xu, D. Qian, M.Z. Hasan, N.P. Ong, A. Yazdani, and R.J. Cava, Phys. Rev. B **81**, 195203 (2010).

29 Y.S. Hor, A.J. Williams, J.G. Checkelsky, P. Roushan, J. Seo, Q. Xu, H.W. Zandbergen, A. Yazdani, N.P. Ong, and R.J. Cava, Phys. Rev. Lett. **104**, 57001 (2010).

30 Z. Wei, L. Lv, M. Zhang, X. Yang, Y. Zhao, S.-H. oscillations, Z. Wei, L. Lv, M. Zhang, X. Yang, and Y. Zhao, J Supercond Nov Magn **28**, 2083 (2015).

31 S.V. Chong, G.V.M. Williams, and R.L. Moody, J. Alloys Compd. **686**, 245 (2016).

32 Y. Xia, D. Qian, D. Hsieh, L. Wray, A. Pal, H. Lin, A. Bansil, D. Grauer, Y.S. Hor, R.J. Cava, and M.Z. Hasan, Nat. Phys. **5**, 398 (2009).

III. TIME-REVERSAL SYMMETRY BREAKING SUPERCONDUCTIVITY IN TOPOLOGICAL MATERIALS

Y. Qiu[1], S. H. Lee[1], K. N. Sanders[1], J. Dai[2], Julie E. Medvedeva[1],

W. Wu[2], P. Ghaemi[3], T. Vojta[1] and Y. S. Hor[1*]

[1]*Department of Physics, Missouri University of Science and Technology, Rolla, MO 65409*

[2]*Department of Physics and Astronomy, Rutgers University, Piscataway, NJ 08854*

[3]*Department of Physics, City College of the City University New York, New York, NY 10031*

Correspondence to: yhor@mst.edu

ABSTRACT

Phases with broken symmetries in the edge states of topological materials have attracted much interest and are expected to realize novel phenomena. On the other hand, the bulk bands of topological materials have not been widely studied as a host of novel states of matter. Here, we report that Nb doping turns the Bi_2Se_3 topological insulator into a bulk type-II superconductor with $T_c \sim 3.2$ K. Nb-doped Bi_2Se_3 features pronounced paramagnetism in its normal phase while preserving the Dirac surface dispersion. In the superconducting state, interplay between the magnetism and superconductivity gives rise to a magnetic ordering and a Hall effect appears even in the absence of a magnetic field, which signals an exotic Cooper pairing that breaks time-reversal invariance.

Fascinating phenomena arise from the Dirac theory of relativistic quantum mechanics (*1*) that describes high energy particles having linear dispersion relations. Electrons in solids move much slower than the speed of light, but their quantum nature can mimic the dispersion of relativistic electrons. The helical surface states of topological insulators are well stablished examples (*2-4*). These edge states provide a unique platform to realize a condensed matter counterpart of novel high energy phenomena such as supersymmetry (*5*), neutrino oscillations (*6*) and Majorana fermions (*7*). Many different types of topological insulators have already been experimentally realized, but despite potential novel application such as topological quantum computing (*8*), a fully confirmed candidate for topological superconductivity is still missing. Coexistence of a magnetism and superconductivity is considered to be an important ingredient of odd-parity spin-triplet pairing for a topological superconductor (*9*). Recent research has focused on unconventional superconductivity that can coexist with spin magnetism; for instance, the uranium compounds UGe2 (*10*), URhGe (*11*) and UCoGe (*12*) have been shown to exhibit superconductivity below 1 K inside the ferromagnetic phase and in proximity to a quantum phase transition.

Similar to topological insulators, topological superconductors are predicted to have topologically protected edge excitations, which are Majorana fermions, exotic particles that are identical to their own anti-particles (*13*); meanwhile, finding them in condensed matter is an active area of current research (*14,15*). A promising candidate for topological superconductivity is Sr_2RuO_4 (*16*), for which experiments suggest chiral *p*-wave spin-triplet pairing, analogous to the A phase of superfluid ^{3}He. This type of pairing can be enhanced by magnetic fluctuations. This Nb-intercalated Bi_2Se_3, $Nb_xBi_2Se_3$ becomes both

a bulk superconductor and a magnetic system (even though Nb is usually considered a non-magnetic cation) indicating the presence of odd-parity spin-triplet superconductivity in $Nb_xBi_2Se_3$.

$Nb_xBi_2Se_3$ crystalizes into a rhombohedral structure, identical to that of Bi_2Se_3 as shown in Fig. 1A, with a slightly increased c-parameter based on the powder x-ray diffraction of single crystals. First-principles density-functional calculations show that the intercalation of Nb in the van der Waals gap between the Se(1)-Bi-Se(2)-Bi-Se(1) quintuple layers is the most favorable (see Supplementary Materials). Moreover, only the intercalated Nb configuration gives a magnetic ground state with magnetic moment of 1.3 μ_B per Nb atom (obtained within the generalized gradient approximation, GGA + U, with a Coulomb repulsion of U = 1 eV for the Nb d-states). For comparison, our calculations predict that intercalated Cu atoms in Bi_2Se_3 have a nonmagnetic ground state, which agrees with the absence of magnetism observed in $Cu_xBi_2Se_3$ (*17-19*).

Figures 1B and C show STM images taken on a cleaved Se surface of a $Nb_{0.25}Bi_2Se_3$ single crystal. The clean surface was obtained by in-situ cleaving under UHV condition ($\sim 10^{-11}$ torr) at room temperature. The images show tall protrusions with apparent heights of about 3 Å. The heights are bias-independent, suggesting that these features are formed by atoms above the cleaved surface. As these protrusions are absent in pure Bi_2Se_3, they likely correspond to intercalated Nb. Their lateral sizes vary, indicating that they are clusters of Nb atoms; however, the clusters may have formed after cleaving. The cloverleaf-shaped three-fold symmetric defects have been identified as Bi_{Se} antisites (*20,21*). The dark three-fold symmetric features shown in Fig. 1B can be attributed to the substitution of Bi with Nb but the substitutional Nb samples in the form of $Bi_{2-x}Nb_xSe_3$ do
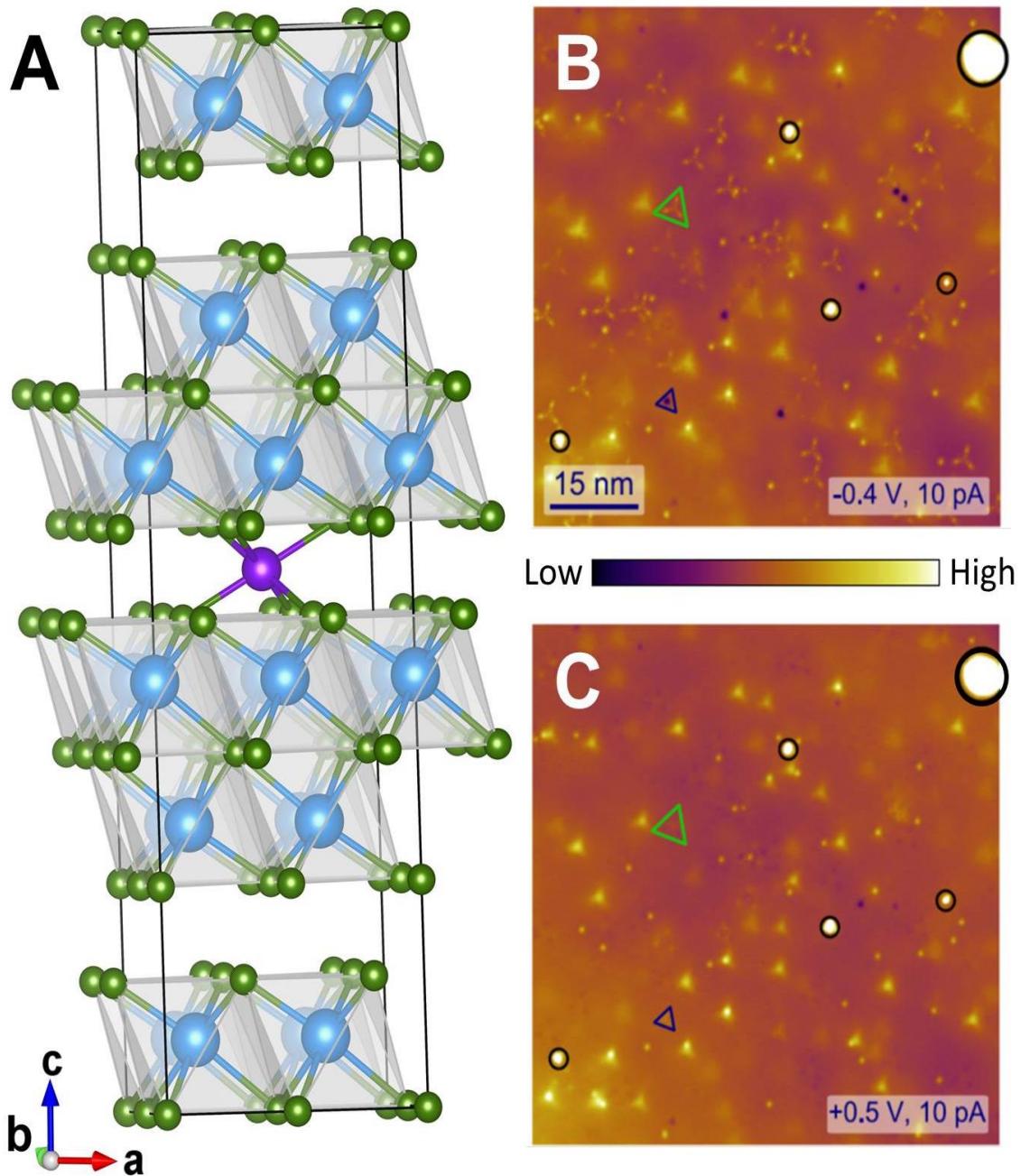
Fig. 1. $Nb_xBi_2Se_3$ crystal structure. (A) Crystal structure of $Nb_xBi_2Se_3$ with a favorable intercalating Nb (the purple circle) site. Light blue and dark green solid circles are Bi and Se, respectively. STM topographic images on a vacuum-cleaved surface of $Nb_{0.25}Bi_2Se_3$ at bias voltages of -0.4 and +0.5 V are shown in (B) and (C), respectively. The black circles mark the protrusions identified as Nb-clusters on the cleaved surface. The green circles mark the Bi_{Se} antisites and the blue triangles mark the substitution of Bi with Nb.

not superconducting at temperatures down to 2 K, which emphasizes the key role played by intercalating Nb atoms.

Dirac surface states are clearly visible in angle-resolved photoemission spectroscopy (ARPES) for both the Bi_2Se_3 topological insulator and the $Nb_{0.25}Bi_2Se_3$ superconductor. Figure 2B shows that the Fermi level of the Bi_2Se_3 is in the bulk band gap, which differs from the ARPES data obtained by Xia et al.(22) because the Bi_2Se_3 crystal studied here was grown by our new method to reduce defects caused by the selenium vacancies (23) (see Supplementary Materials). In contrast, the Fermi level of the $Nb_{0.25}Bi_2Se_3$ is located in the conduction band as both the bulk valence and conduction bands near the Γ point are clearly observed (Fig. 2C).

The longitudinal resistivity ρ in Fig. 2D shows metallic behavior from room temperature to 3.6 K. The superconducting transition starts at 3.6 K and ρ drops to zero at about 3.2 K (Fig. 2E). The field-dependent ρ in Fig. 2F yields the upper critical fields $B_{c2\perp}(2K) = \mu_0 H_{c2\perp} = 0.15$ T for fields parallel to the crystallographic c-axis and $B_{c2\parallel}(2K) = \mu_0 H_{c2\parallel} = 0.31$ T for fields parallel to the ab plane. The temperature dependence of the upper critical fields is plotted in Fig. 2G. Extrapolations to zero temperature give the values $B_{c2\perp}(0K) \approx 0.2$ T and $B_{c2\parallel}(0\,K) \approx 0.4$ T. This implies an in-plane coherence length of $\xi_{ab} = \sqrt{\Phi_0/(2\pi B_{c2\perp})} \approx 40$ nm. Analogously, from $\xi_{ab}\xi_c = \Phi_0/(2\pi B_{c2\parallel})$, we obtain $\xi_c \approx 20$ nm. We conclude that $Nb_{0.25}Bi_2Se_3$ is an anisotropic type-II superconductor with an anisotropy ratio of $B_{c2\parallel}/B_{c2\perp} \approx 2$. The total specific heat coefficient c_p of a $Nb_{0.25}Bi_2Se_3$ multicrystalline sample in zero magnetic field shows an anomaly at the T_c. This indicates that the superconducting transition is a bulk transition (Fig. 2H). In 5 kOe field, the sample remains in the normal state down to the lowest temperatures. Its specific heat follows the
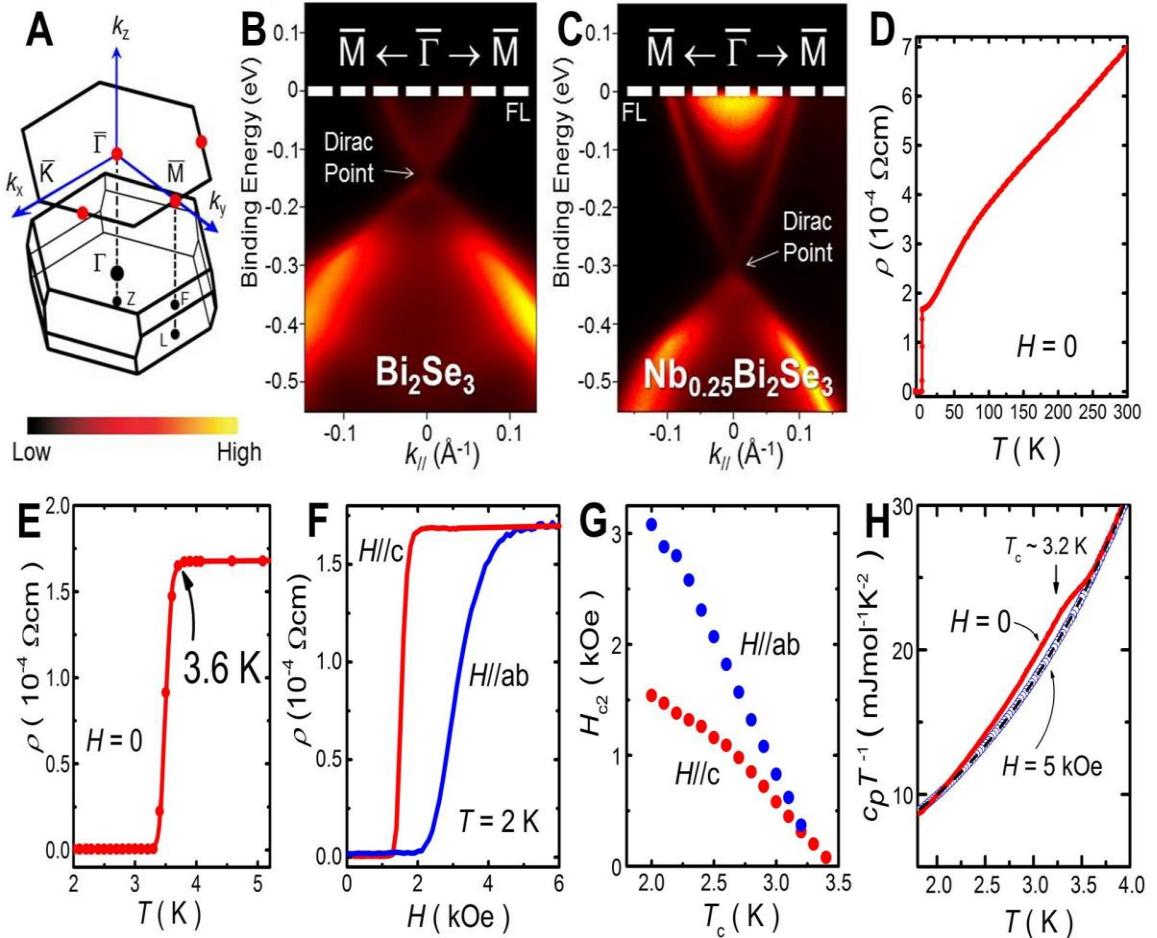
Fig. 2. Dirac surface state of $Nb_xBi_2Se_3$. (A) A schematic diagram of bulk 3D Brillouin zone (BZ) of Bi_2Se_3 crystals and the 2D BZ of the projected (111) surface. (B) ARPES data taken at 12.8 K for a Bi_2Se_3 single crystal grown by the two-step method. It shows the surface state with the Dirac point ~0.15 eV below the FL. The FL lies in the band gap indicating that the Bi_2Se_3 is a nearly perfect topological insulator. (C) FL in $Nb_{0.25}Bi_2Se_3$ lies in the bulk conduction band indicating an *n*-type conductor. The Dirac point is ~0.3 eV below the FL. (D) Temperature-dependent resistivity of $Nb_{0.25}Bi_2Se_3$ at $H = 0$ shows metallic behavior in its normal state identical to that of Bi_2Se_3. (E) The resistivity starting to drop at 3.6 K and becoming zero at 3.2 K. (F) Magnetic-field dependent resistivity of that $Nb_{0.25}Bi_2Se_3$ at 2 K for $H//c$ and $H//ab$. (G) Upper critical field Hc_2 as a function of temperature for $H//c$ and $H//ab$. H_{c2} is defined by 50% of the normal-state resistivity $\rho(H_{c2}) = 0.5\rho(T_c)$. (H) Temperature dependence of specific heat measured in 0 and 5 kOe applied fields. The dashed line is the Debye fitting to the 5 kOe data.

conventional Debye fit, $c_{\mathrm{p}} = c_{\mathrm{h}} + c_{\mathrm{e}} = \gamma T + A_3 T^3 + A_5 T^5$, where c_h and c_e are phonon and electron contributions, respectively, and the normal-state electronic specific-heat coefficient γ is 4.54 mJmol^{-1}K^{-2}.

Superconductivity of Nb$_{0.25}$Bi$_2$Se$_3$ is verified by the magnetization shown in Fig. 3A. Below 3.2 K, we observe diamagnetic shielding with a volume fraction close to 100% (much greater than the 20% observed in Cu$_{0.12}$Bi$_2$Se$_3$ (*17*)) indicating the full sample and not just local patches of Nb has become superconducting. The AC magnetization is reversible, i.e., zero-field cooled (ZFC) and field-cooled (FC) magnetizations are overlapping. In its normal state, Nb$_{0.25}$Bi$_2$Se$_3$ shows paramagnetism as depicted in Fig. 3B. The normal-state susceptibility follows a Curie law with an effective moment of 1.26 μ_{B}/Nb which agrees well with the 1.3 μ_{B}/Nb predicted by the density functional calculations. Figure 3C shows DC magnetization-field (MH) curves at $T = 2$K (the diamagnetic background has been subtracted). The magnetization below H_{c2} is anisotropic. For in plane field H//ab, the MH curve (the right inset of Fig. 3C) features the hysteresis loops of a strongly pinning type-II superconductor that follows the Bean's model (*24*); for the field perpendicular to the plane H//c, the MH curve (the left inset of Fig. 3C) strongly deviates from the Bean's model. As H increases from zero, the sample develops diamagnetism due to the Meissner effect. Increasing H above H_{c1} leads to a mixed state in which magnetic vortices penetrate the material. From the low-field magnetization maxima, we find $H_{c1\perp} \sim 23$ Oe and $H_{c1\parallel} \sim 50$ Oe reflecting the anisotropic character of the superconductivity. However, the magnetization of the normal state is isotropic and reversible. It shows saturation moment of ~ 0.3 μ_{B}/Nb which is smaller than the effective
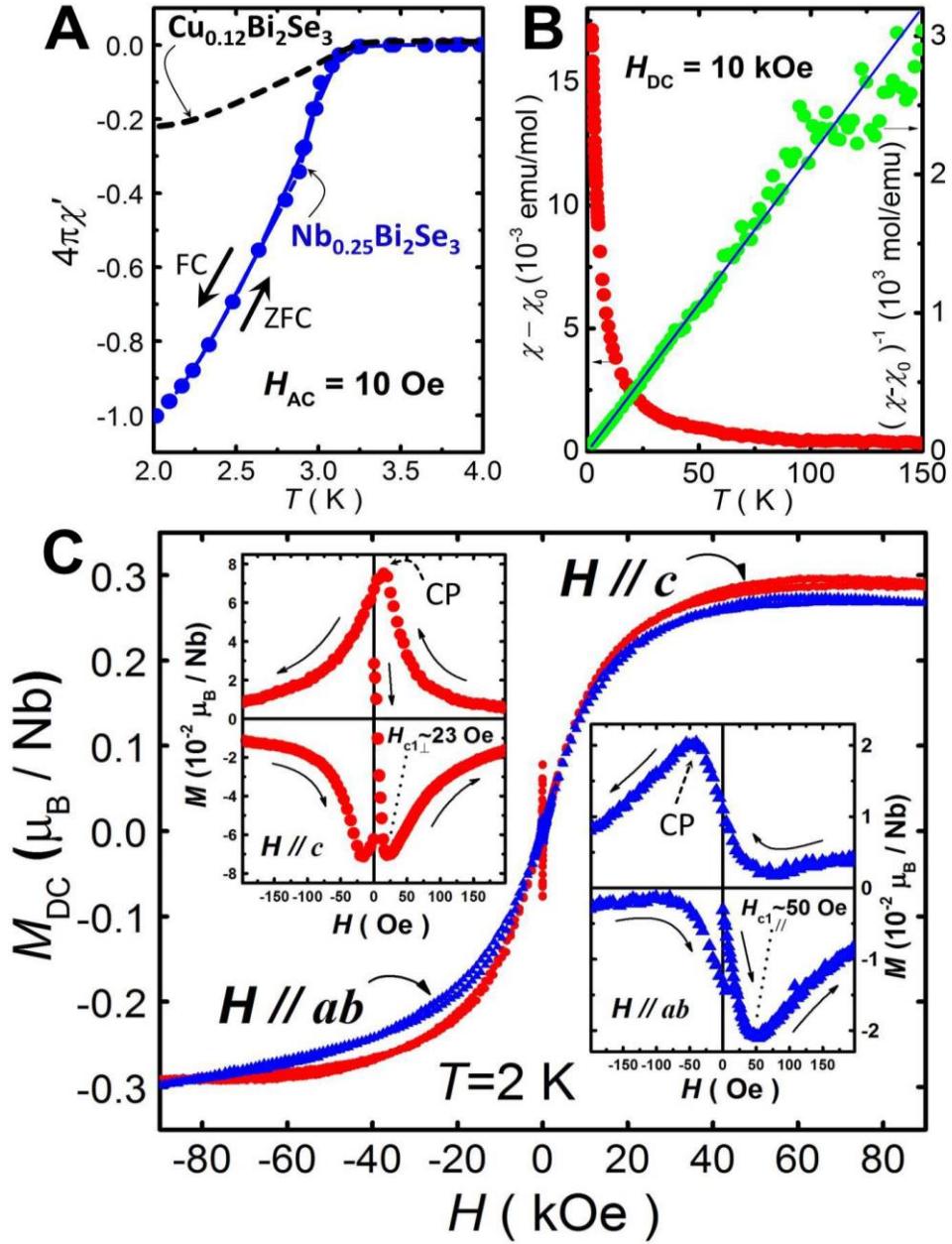
Fig. 3. Magnetic properties of $Nb_xBi_2Se_3$. (A) AC magnetization as a function of temperature for a sample consisting of 15 tiny $Nb_{0.25}Bi_2Se_3$ single crystals. The crystals are stacking up with their c-axes oriented parallel to each other. H is parallel to the c-axes of the crystals ($H//c$). (B) Temperature-dependent magnetic susceptibility (red circles) of the sample at 10 kOe DC applied magnetic field H. The susceptibility is diamagnetic background-subtracted which is $\chi - \chi_0$. The inverse molar susceptibility (green circles) of the sample shows paramagnetic behavior that follow Curie's law. (C) Field-dependent DC magnetization (MH) for $H//c$ (red circles) and $H//ab$ (blue triangles) at 2 K. The left inset (right inset) shows the low-field region of the $H//c$ ($H//ab$) MH curve. Arrows show ascending and descending field branches. The location of the central peak (CP) is indicated by the dashed arrow.

moment of 1.26 μ_B/Nb determined from the inverse susceptibility in Fig. 3B, suggesting an itinerant magnetism (*25*).

The MH curve for *H//c* displays an unusual feature. The position of the central peak, i.e., the maximum of the low-field MH curve, in the descending field branch of the *H//c* hysteresis loop is anomalously shifted to a positive field value while it is expected at a negative field within critical state models of strongly pinning type-II superconductors (*24*). We believe that the feature can be attributed to an interplay between superconductivity and the magnetic Nb ions. The Nb moments create inhomogeneous internal magnetic fields which the superconductor tries to expel. Flux pinning and compression then lead to a nonzero magnetization. Analogously, the normal position of the central peak stems from the fact that, normally, the internal magnetic field lags behind the external one. This anomalous position of the central peak in $Nb_{0.25}Bi_2Se_3$ implies that the internal field is ahead of the applied one. This may be explained by additional internal magnetic fields due to the Nb moments, similar to what was seen in ferromagnet/superconductor/ferromagnet trilayered thin films (*26*). In addition, screening currents flowing on the surfaces of the small crystals making up our sample may provide further internal magnetic fields.

Consistent with the ARPES, Hall conductivity of $Nb_{0.25}Bi_2Se_3$ in the normal state confirm the *n*-type conductivity. The transverse resistivity ρ_{yx} at 3.8 K is a linear function of the applied magnetic field suggesting that a single type of electron carriers dominates the transport. The carrier density n_e, calculated from the Hall coefficient R_H is about 1.5×10^{20} cm^{-3}. Below T_c, the Hall measurement provides one of the most striking features of $Nb_{0.25}Bi_2Se_3$ i.e. the spontaneous Hall effect as seen in Fig. 4. Upon entering the superconducting phase, ρ_{yx} jumps to a much larger value that is roughly independent of the
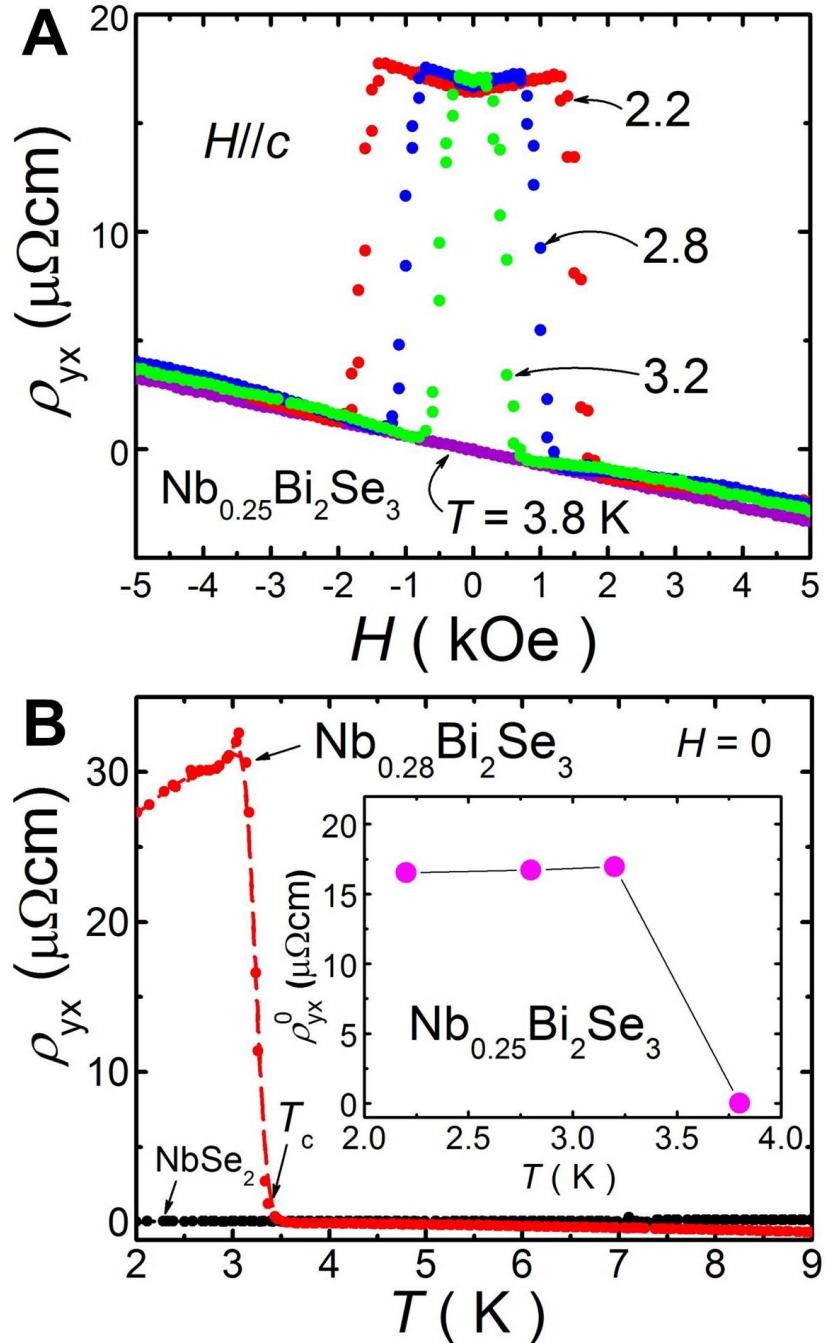
Fig. 4. Zero-field Hall effect in the superconductor. (A) Hall resistivity as a function of applied magnetic field for a $Nb_{0.25}Bi_2Se_3$ single crystal at different temperatures. The applied field is along the c-axis of the single crystal and the current is along the crystal ab-plane. (B) Zero-field Hall effect (see Supplementary Materials for detailed information) is observed at below T_c for $Nb_{0.28}Bi_2Se_3$ single crystal (red curve). As comparison, Hall resistivity of a type-II $NbSe_2$ superconductor which was measured simultaneously with the $Nb_{0.28}Bi_2Se_3$ shows no observed Hall effect below its T_c which is 7.2 K (black curve). The inset shows the zero-field Hall resistivity ρ^0_{yx}, the amplitude of the Hall resistivity in (A) at $H = 0$ plotted as a function of temperature.

field. In particular, ρ_{yx} is nonzero even in the absence of an external field. As the longitudinal resistance is zero in the same temperature and field ranges, the Hall resistance cannot be caused by flux flow. These observations indicate that the superconducting state itself breaks time-reversal invariance in $Nb_{0.25}Bi_2Se_3$. Time-reversal symmetry breaking superconductivity has attracted considerable attention recently in cuprates, heavy-fermion materials, and iron pnictides. An extensively discussed example is the chiral *p*-wave spin-triplet state suggested for Sr_2RuO_4 (*27*). Theoretical calculations show that impurity scattering in such *p*-wave spin-triplet superconductor can indeed lead to a nonzero spontaneous Hall resistivity (*28,29*). The sign of Hall conductivity in the superconducting phase of $Nb_{0.25}Bi_2Se_3$ is independent of external field (Fig. 4A). This indicates that the superconducting pairing is the main source of time-reversal symmetry breaking that leads to the spontaneous Hall effect.

Since the discovery of superconductivity in $Cu_xBi_2Se_3$ and $Sr_xBi_2Se_3$ (*30*), the possibility of odd-parity superconductivity in doped topological insulators has been widely investigated. However, the commonly explored pairing type is a time-reversal symmetric odd-parity state (*31*). In contrast, our results for $Nb_xBi_2Se_3$ support a pairing state that spontaneously breaks time-reversal symmetry, implying that the effects of Nb dopants go beyond a mere change of chemical potential. Further work will be necessary to identify the superconducting state beyond doubt, to establish a pairing mechanism and to explore the role played by the magnetism of the Nb ions. Our results open the exciting possibility that a variety of exotic superconducting phases may be realized in doped topological insulators.

ACKNOWLEDGEMENTS

SUPPLEMENTARY MATERIALS

Materials and Methods

1. Crystals Growth of Nb-doped Bi$_2$Se$_3$

A mixture of stoichiometric ratio of Nb (99.99%), Bi (99.999%) and Se (99.999+%) elements for Nb$_x$Bi$_2$Se$_3$ was heated up to 1100 ℃ for 3 days in sealed vacuum quartz tubes. The crystal growth took place in cooling from 1100 ℃ to the quenched temperature 600 ℃ at 0.1 ℃/min producing Nb$_x$Bi$_2$Se$_3$ tiny crystals with sizes ranging from 0.1 to 1 mm. The method was also used to grow Bi$_{2-x}$Nb$_x$Se$_3$ single crystals.

2. Crystals Growth of Bi$_2$Se$_3$

Se bleaching out of the Bi$_2$Se$_3$ crystal during crystal growth (*23*) can be prevented by following the two-step sealing crystal growth method. As reported, the *p*-type Bi$_2$Se$_3$ could be achieved if the volume of the reaction space was reduced (*32*). Therefore, the two-step sealing method can dramatically reduce the reaction volume for the crystal growth. First, a stoichiometric mixture of high purity elements of Bi (99.999%) and Se (99.999+%) in the ratio of 2:3 will be vacuum sealed in a Pyrex tube as shown in Fig. S1A. Second, the sealed Pyrex tube is then vacuum sealed in a bigger size quartz tube with a small amount of Se (Fig. S1B). The amount of Se can be estimated by using the ideal gas law in order to produce ∼ 4 atmospheric pressure in the quartz tube when the temperature reaches 800 ℃. At this temperature, the inner Pyrex tube is softened to be compressed into a small reaction volume by the Se-vapour pressure (Fig. S1C). The melt is kept at 800 ℃ overnight to ensure a homogenous reaction. The crystal growth takes place when the melt is cooled from 800 to 550 ℃ at the rate of 6 ℃ per hour. In this case, volume of the reaction

space is reduced and no Se is bleaching out of the crystal during the crystal growth process. Hence, less Se-vacancy defect can be obtained thereby eliminating the possibility of excess electrons which assures that the crystal will have a low carrier concentration.
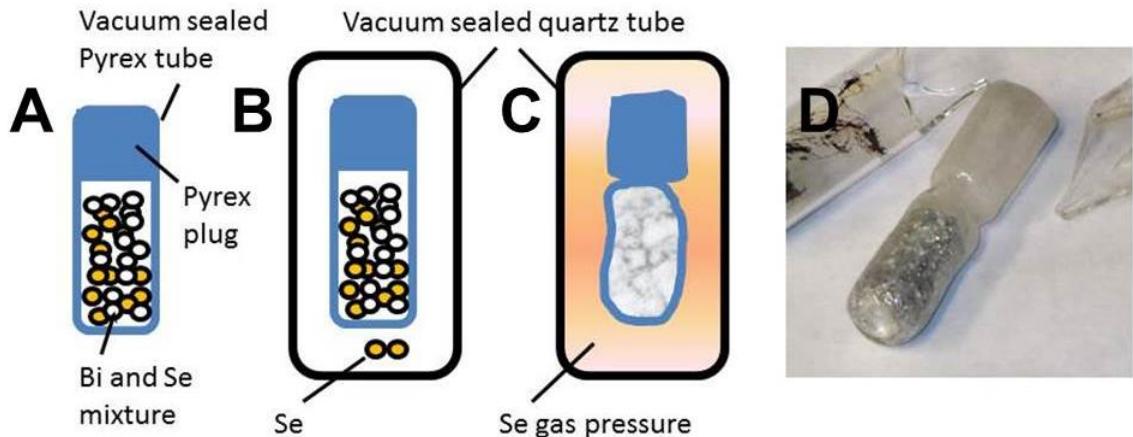
Fig. S1. Two-step sealing method. (A) Stoichiometric mixture of Bi and Se in the vacuum sealed tube. (B) The sealed Pyrex tube is sealed in a quartz tube with Se. (C) The two-step sealed tube is heated up to 800 °C. (D) The outcome of the two-step method.

3. Characterizations and Physical Property Measurements

Omicron LT-STM under ultra-high vacuum ($\sim 1 \times 10^{-11}$ mbar) was used for the STM imaging and spectroscopic experiments at 4.5 K cooled by liquid helium. The differential conductance measurements were carried out using the standard lock-in technique with transimpedance amplifier gain $R_{gain} = 3$ GΩ, AC modulation frequency $f = 455$ Hz and modulation amplitude $V_{mod} = 5$ mV. ARPES measurements were performed at the PGM beamline of the Synchrotron Radiation Center (SRC), Wisconsin using a Scienta R4000 analyzer with an energy resolution better than 5 meV and an angular resolution better than 0.2° (corresponding to a momentum resolution of $\Delta k \leq 0.009$ Å^{-1} at

photon energy $hv = 30$ eV). Physical properties were measured using a Quantum Design Physical Property Measurement System (PPMS). Electrical resistivity measurements were made on a rectangular sample of uniform thickness (approximate size $1 \times 1 \times 0.1$ mm^3) using a standard four-probe technique. A small direct current of 3 mA was applied to prevent the sample from electrical heating. The Hall resistivity ρ_{yx} was measured by a five-probe technique (see below), where the electrical current was applied in the ab plane. The contacts for ρ and ρ_{yx} were made by attaching Pt wires with room-temperature cure silver paint. The specific-heat c_p data were taken by a relaxation-time method using a commercial system; the addenda signal was measured before mounting the sample and was duly subtracted from the measured signal. The c_p measurement was done in zero field for the superconducting state and 5 kOe was applied along the c axis for the normal state, while the change of the addenda signal between the two was found to be negligible. The AC and DC magnetizations were measured with the PPMS.

4. Magnetization Measurements and Zero-Field Magnetization (ZFM)

All of the magnetic properties illustrated here were performed by using the AC Measurement System (ACMS) in the Quantum Design PPMS and its external magnetic field was generated by the superconducting solenoid. The magnetic behaviors in the superconducting regime of Nb$_x$Bi$_2$Se$_3$ show several surprising features. The most unusual aspect as shown in Fig. S2A is the appearance of a hysteresis loop below the lower critical field, $H_{c1\perp} \sim 23$ Oe. No hysteresis loop observed in Bi$_2$Se$_3$ indicating that the hysteresis loop of Nb$_x$Bi$_2$Se$_3$ is intrinsic and not due to a remnant or trapped field in the measurement system. For a magnetically reversible sample (or irreversible sample with a coercivity), its low field MH curve would show an inverted hysteresis loop if the remnant field produced

from the superconducting solenoid is present (or is larger than the coercivity). The inverted

hysteresis loop displays clockwise behavior in contrast to the generally observed counter-

clockwise hysteresis loop. The hysteresis loop in Fig. S2A depicts counter-clockwise

behavior and is not inverted hysteresis indicating the remnant field is smaller than the

coercivity field.
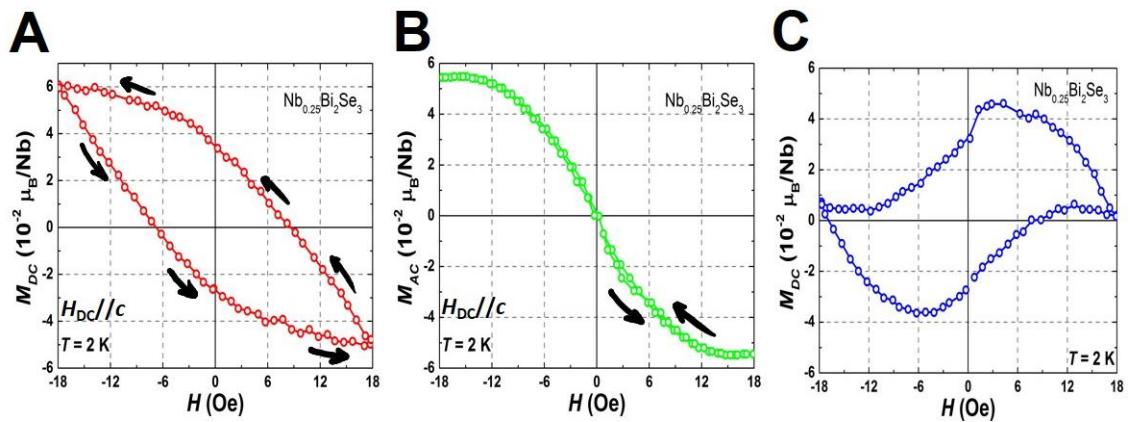
Fig. S2. Magnetization measurement. (A) DC magnetization measurement where the applied magnetic field is constant during the measurement. MH loop is clearly observed. (B) AC magnetization measurement where the applied magnetic field is oscillating with the frequency of 1000 Hz during the measurement to manifest the conventional superconductor Meissner effect. Arrows show ascending and descending field directions. (C) Hysteresis loop after the subtraction of AC magnetization measurement from the DC loop.

It is important to note that the magnetization data points in Fig. S2A are obtained

with constant external magnetic field (or called DC field magnetization measurement)

aligned parallel to c-axis of the crystal. However, there is another measurement option

available in ACMS where the external magnetic field is in the oscillation mode, so-called

AC magnetization measurement. In AC magnetization measurement, applied oscillating

magnetic field can manifests conventional superconductor Meissner effect but suppresses ferromagnetic ordering. Therefore, no hysteresis loop is observed in the AC field scanned measurement as illustrated in Fig. S2B. Interestingly, the hysteresis loop that might be due to ferromagnetism in the system is clearly observed after the AC field scanned data has been subtracted from the DC hysteresis loop. In other words, the DC magnetization loop is the combination signal of superconductivity and ferromagnetism ordered. That observation is not observed for fields parallel to the *ab*-plane.

To further prove that the hysteresis loop is indeed an intrinsic feature and associates with the superconducting state to form a symbiotic state, we performed the field-dependent DC magnetization measurements in the superconducting regime with different temperatures below T_c. Fig. S3 shows the low field hysteresis loops of $Nb_{0.25}Bi_2Se_3$ sample for *H*//*c*. In Fig S3A-D, the appearance of a nonzero magnetization below T_c in the absence of an applied magnetic field *H* or zero-field magnetization (ZFM) is observed. The hysteresis loop is getting smaller when the temperature is increased and the hysteresis loop vanishes at $T > T_c$.

From Fig. 2G in the main text, $Nb_{0.25}Bi_2Se_3$ superconductor is anisotropic due to the tendency of its vortex supercurrents to be on the *ab*-plane. Therefore, the symbiotic state of ferromagnetism and superconducting in the system produces an internal magnetic field either parallel or antiparallel to the *c*-axis which explains the ZFM is having an either positive or negative sign in its ascending and descending field braches. By plotting the magnitude of the ZFM in its descending field braches in a function of temperatures as shown in Fig. S3H, the ZFM is decreasing as the temperature increases and only presents in the superconducting state. This implies that the symbiosis state of ferromagnetism with

the superconductivity in the $Nb_xBi_2Se_3$ system. It is strongly believed that Nb magnetic moments are polarized by the superconductivity in the system.
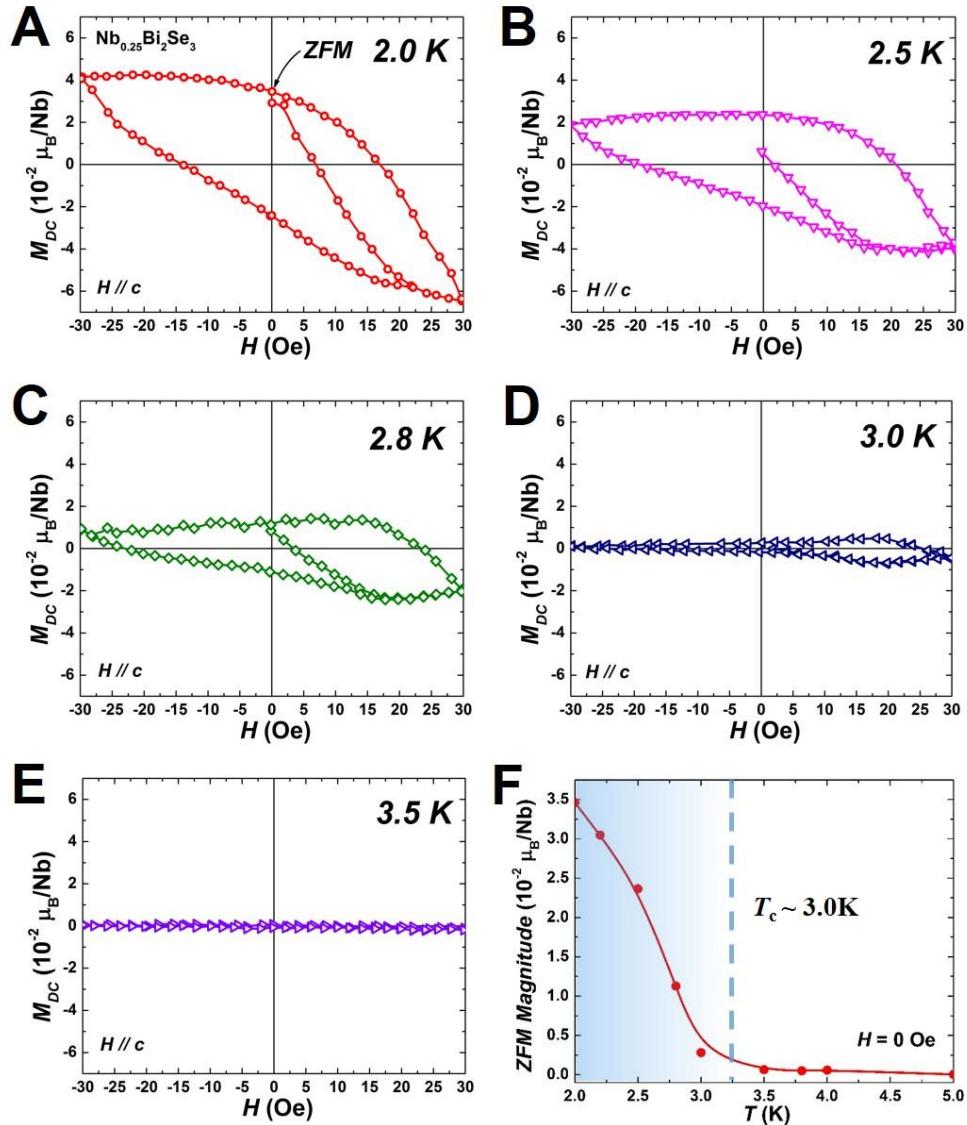
Fig. S3.   Zero-field Magnetization measurement. (A)-(E) MH loop at different temperatures. The hysteresis loop is only observed for temperatures below T_c. (F) ZFM magnitude as the function of temperatures. Nonzero magnetization is observed for temperature below T_c.

5. Zero-Field Hall Effect Measurements

A superconducting solenoid composed of a type II superconductor is used in the PPMS to produce the applied (or external) magnetic field H. The magnitude of the applied field is based only on the current generated in the magnet power supply but not determined by a field sensor such as a Hall sensor. Since a type II superconductor is used, a remnant or trapped flux can be retained after discharging the solenoid from a high field to zero magnet current at low temperatures (*33*). In order to completely eliminate the trapped flux, liquid helium was evacuated from the PPMS dewar and warmed the superconducting solenoid to room temperature for one week. The PPMS was then filled up with liquid helium with no current supplied to the superconducting solenoid for the zero-field Hall effect measurement.
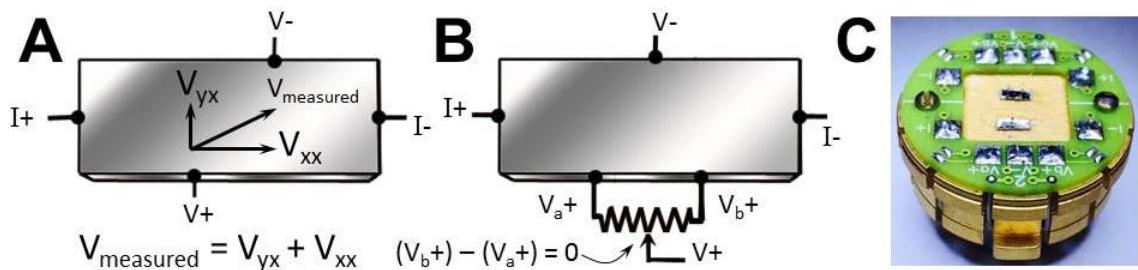
Fig. S4. Hall resistivity measurement. (A) Contact leads for four-wire Hall measurement on a sample bar. Offset V_{xx} is due to a longitudinal resistivity. (B) Offset nulling can be performed with five-wire Hall measurement. The Hall voltage V_{yx} can be obtained by measuring the voltage dropped between V- and V+. (C) The setup of the five-wire Hall measurement. The Hall measurements for two samples can be performed simultaneously.

The PPMS is equipped with AC Transport Measurement System and incorporates a precision current source (0.02 µA to 2 A) and a precision voltage detector (0.02 µV to

2 V) for the Hall effect measurement. The ACT can supply an AC bias current from 1 Hz up to 1 kHz and can, therefore, provide greater measurement sensitivity than DC instruments because signal filtering can be employed. The Hall coefficient R_h defined by $R_h = V_{yx}A/IlB$ can be obtained from measuring transverse voltage or Hall voltage V_{yx} at an applied magnetic field B. I/A is the current divided by the sample cross section area, and l is the separation of the transverse voltage leads. It can be shown that $R_h = (nq)^{-1}$, with n representing the number of charge carriers per unit volume in the sample, and q representing the charge of the carriers. To ensure a precise Hall voltage measurement, five-wire Hall measurement is used. This would dramatically reduce the contribution of the longitudinal voltage V_{xx} to the voltage measured $V_{measured}$ as shown in Fig. S4B. An external 100 Ω potentiometer is used in the five-wire Hall measurement to nullify the longitudinal voltage. Hence, the voltage measured between V+ and V- is a Hall voltage V_{yx} and Hall resistivity $\rho_{yx} = V_{yx}A/Il$ can be obtained. The nullifying resistance from the external potentiometer is a constant which does not depend on temperature and applied field. Figure S4C shows the set up for measuring two samples simultaneously. In the Hall effect measurements, nullifications of the longitudinal resistivity for $Nb_xBi_2Se_3$ and $NbSe_2$ were performed at 4 K and 8 K, respectively. The offset has been subtracted for the ρ_{yx} plotted as a function of field in Fig. 4A.

6. Computational Method

First-principles density-functional calculations were performed using highly-precise full-potential linearized augmented plane wave method (*34,35*) with the generalized gradient approximation (GGA) and GGA + U. Cut-offs for the basic functions, 16.0Ry, and potential representation, 81.0Ry, and expansion in terms of spherical

harmonics with $l \leq 8$ inside the muffin-tin spheres were used. Summations over the Brillouin zone were carried out using 14–63 special k points in the irreducible wedge. For every structure investigated, the internal positions of all atoms were optimized via the total energy and atomic forces minimization.

There are three different site locations for a single interstitial Nb atom in Bi_8Se_{12} that are namely between the two Se(1) layers at the internal position where $R_1 = (0, 0, 0.5)$, between Se(1) and Bi layers at $R_2 = (0.06, 0.06, 0.37)$, or between Bi and Se(2) layers at $R_3 = (-0.14, 0.36, 0.14)$. From the accurate total energy calculations for non-magnetic $Nb:Bi_8Se_{12}$, it is found that the R_1 site position for single Nb atom is the most favorable energetically with Nb in the R_2 or R_3 position being higher in energy by 545 meV or 970 meV, respectively. Such a strong preference for the Nb-intercalated bismuth selenide is in contrast to Cu in Bi_8Se_{12} (*17-19*). From additional calculations we find that although a single Cu atom also prefers to reside in position R_1, the total energy of Cu in the R_2 or R_3 position is higher by only 19 meV or 377 meV, respectively, suggesting that intra-layer Cu is likely to occur and may co-exist with Cu-intercalate.

In addition, Nb-intercalated Bi_8Se_{12} corresponds to a magnetic state, in marked contrast to $Cu:Bi_8Se_{12}$. For a single Nb atom in site position R_1, a ferromagnetic state is lower in energy by 55 meV as compared to the non-magnetic configuration. At the same time, the calculated total energy difference between the non-magnetic and ferromagnetic states is negligible for Nb in R_2 or R_3 positions (< 6 meV) and for Cu in any of the three site positions (< 0.5 meV). The local magnetic moment on Nb is expected from the partially occupied Nb d-states—in marked contrast to the fully occupied d-states of Cu. The differences in the electronic configuration of Nb and Cu give rise to fundamentally

different electronic properties of Nb and Cu-intercalated Bi_8Se_{12}. The calculated density of states (Fig. S5) reveals that the occupied Cu d-states are located within the valence band and do not alter the density of states in the conduction band. The latter suggests that addition of Cu resembles a rigid-band shift, i.e., Cu provides additional electrons to the bismuth selenide framework but itself does not participate in transport. In marked contrast to Cu, the partially occupied Nb d-states give significant contribution at the FL as shown in Fig. S5A. Furthermore, a comparison with the total density of states for undoped Bi_8Se_{12} where a rigid-band shift of the FL represents an addition of an extra electron (c.f., red line in Fig. S5A), reveals that the presence of Nb affects the total density of states at the bottom of the conduction band.

The partially occupied Nb d-states require that the effective on-site Coulomb interaction is taken into account (*36*). For U = 0, 1 eV, or 2 eV, our calculated magnetic moment on the Nb atom in the R_1 site location is 0.6, 1.3, or 1.5 μ_B, respectively. The value obtained for the U = 1 eV is in excellent agreement with the observed effective moment of 1.26 μ_B/Nb.

To shed light on the nature of magnetic interactions between the Nb atoms, a larger supercell of bismuth selenide, $Bi_{16}Se_{24}$, was considered to include two Nb atoms located in the R_1 site positions, i.e., within the same layer between the two Se(1) layers. Three atomic configurations for an intercalate Nb dimer with the Nb-Nb distance of 4.1, 7.2 and 8.3 Å were considered. For all Nb dimer configurations, an antiferromagnetic ground state was found with the total energy of the ferromagnetic state being higher by only 16–26 meV. The small energy difference between the ferromagnetic and antiferromagnetic

configurations of two intercalated Nb atoms is in accord with the experimental observations.
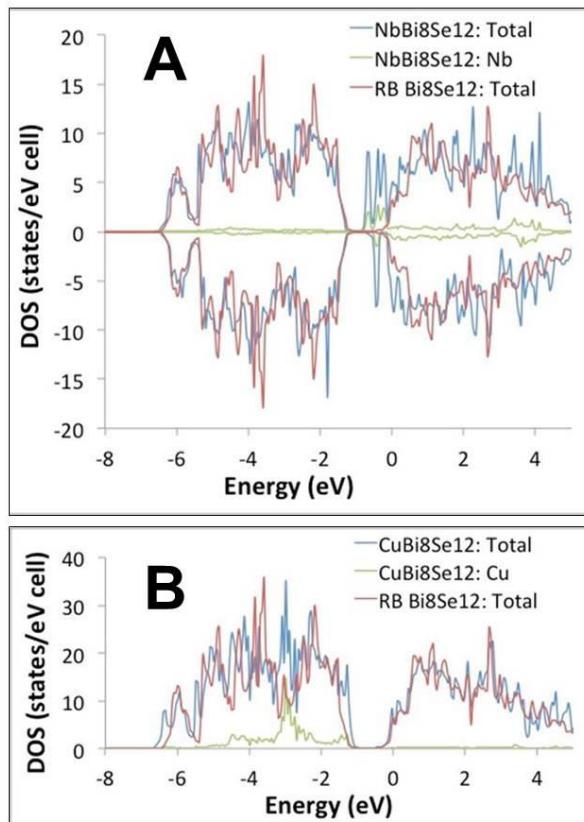
Fig. S5. DFT-GGA-calculated density of states (DOS) for (A) Nb-intercalated Bi_8Se_{12} and (B) Cu-intercalated Bi_8Se_{12}. The total and the partial (Nb or Cu) density of states are plotted with a blue and green line, respectively. For comparison, the density of states of undoped Bi_8Se_{12} where the FL is moved up into the conduction band via a rigid-band (RB) shift is plotted with a red line. The FL is at 0 eV in all plots.

REFERENCES

1. P. A. M. Dirac, *Proceedings of the Royal Society of London Series A* **117**, 610-624 (1928).

2. L. Fu, C. L. Kane & E. J. Mele, *Phys. Rev. Lett.* **98**, 106803 (2007).

3. J. E. Moore & L. Balents, *Phys. Rev. B* **75**, 121306(R) (2007).

4. D. Hsieh *et al.*, *Nature* **452**, 970-975 (2008).

5. P. Ponte & S.-S. Lee, *New J. Phys.* **16**, 013044 (2014).

6. P. Ghaemi & V. P. Nair, *Phys. Rev. Lett.* **116**, 037001 (2016).

7. J. Alicea, *Rep. Prog. Phys.* **75**, 076501-076537 (2012).

8. S. Bravyi & A. Kitaev, *Annals of Physics* **298**, 210-226 (2002).

9. A. P. Schnyder & P. M. R. Brydon, *J. Phys.: Condens. Matter.* **27**, 243201 (2015).

10. S. S. Saxena *et al.*, *Nature* **406**, 587-592 (2000).

11. D. Aoki *et al.*, *Nature* **413**, 613-616 (2001).

12. N. Huy *et al.*, *Phys. Rev. Lett.* **99**, 67006 (2007).

13. E. Majorana, *Nuovo Cimento* **5,** 171-184 (1937).

14. V. Mourik *et al.*, *Science* **336**, 1003-1007 (2012).

15. S. Nadj-Perge *et al.*, *Science* **346**, 602-607 (2014).

16. K. D. Nelson *et al.*, *Science* **306**, 1151-1154 (2004).

17. Y. S. Hor *et al.*, *Phys. Rev. Lett.* **104**, 057001 (2010).

18. M. Kriener *et al.*, *Phys. Rev. Lett.* **106**, 127004 (2011).

19. P. Das *et al.*, *Phys. Rev. B* **83**, 220513(R) (2011).

20. S. Urazhdin *et al.*, *Phys. Rev. B* **66**, 161306 (2002).

21. C. Mann *et al.*, *Nat. Commun.* **4**, 2277 (2013).

22. Y. Xia *et al.*, *Nat. Phys*. **5**, 398 (2009).

23. Y. S. Hor *et al.*, *Phys. Rev. B* **79**, 195208 (2009).

24. C. P. Bean, *Phys. Rev. Lett.* **8**, 250-253 (1962).

25. T. Moriya, (eds M. Cardora, P. Fulde & H. J. Queisser) Ch. 4 (*Springer*, *Berlin*, 1985).

26. S. Kobayaki *et al.*, *Phys. Rev. B* **66**, 214520 (2002).

27. A. P. Mackenzie & Y. Maeno, *Rev. Mod Phys.* **75**, 657 (2003).

28. J. Goryo, *Phys. Rev. B* **78**, 060501 (2008).

29. R. M. Lutchyn, P. Nagornykh & V. M. Yakovenko, *Phys. Rev. B* **80**, 104508 (2009).

30. Z. Liu *et al.*, *J. Am. Chem. Soc.* **137** (33), 10512-10515 (2015).

31. Liang Fu, *Phys. Rev. B* **90**, 100509(R) (2014).

32. H. Köhler and A. Fabricius, *Phys. Status Solidi B* **71**, 487 (1975).

33. G. Mastrogiacomo and J. F. Löffler, *Appl. Phys. Lett.* **92**, 082501 (2008).

34. E. Wimmer, H. Krakauer, M. Weinert and A. J. Freeman, *Phys. Rev. B* **24**, 864-875 (1981).

35. M. Weinert, E. Wimmer and A. J. Freeman, *Phys. Rev. B* **26**, 4571-4578 (1982).

36. E. Şaşıoğlu, C. Friedrich and S. Blügel, *Phys. Rev. B* **83**, 121101(R).

IV. ELECTRIC-FIELD EXFOLIATION OF LAYERED CRYSTALLINE MATERIALS

A. Mark[1], S. H. Lee[1], J. E. Medvedeva[1], E. W. Bohannan[2] and Y. S. Hor[1*]

[1]Department of Physics, Missouri University of Science and Technology, Rolla, MO 65409

[2]Graduate Center for Material Research, Missouri University of Science and Technology, Rolla, MO 65409

ABSTRACT

Layered materials in two-dimensional systems, such as Bi_2Se_3, exhibit many intriguing physical properties. They have the potential to be used in the fabrication of next generation miniature electronic devices. However, it has been difficult to obtain nanostructure crystalline flakes without using a long and tedious process to fabricate nanostructures directly from precursor materials. Here we demonstrate a method of exfoliating layered crystalline materials utilizing an electric field. The process is capable of separating ultrathin flakes from several as-grown layered bulk crystals. The method is simple, effective, and does not require advanced equipment used in previous methods due to direct exfoliation of bulk materials rather than attempting to coerce structures to form during crystal growth. The nanostructures that are extracted using this method are demonstrated to be flat, freestanding, and relatively large. These qualities are highly desirable for utilization in electronic devices and study its novel physics phenomena that can arise in two-dimensional quantum systems.

INTRODUCTION

Two-dimensional systems such as graphene, transition metal dichalcogenides (TMDs), and topological insulators are promising materials for fabrication into faster, smaller and better electronic devices. The electronic properties of monoatomic layers of the materials have generated a tremendous amount of attention for both fundamental physics studies and technological application (1–7). However, the lack of a simple and effective method for producing monoatomic layered nanocrystalline materials hamper those interesting studies and technology development. Current existing methods in fabricating the two-dimensional monoatomic materials involve either expensive and tedious process such as molecular beam epitaxy (MBE) (3,8,9) or inexpensive but unclean mechanical exfoliation (10) e.g., Scotch tape method (1,7). For Bi_2Se_3, a topological insulator, nanoscale crystalline flakes are highly demand, but it is difficult to produce a high quality nanocrystalline sample. The current thin flakes of Bi_2Se_3 fabricated via various methods was usually less than a micron sized (8,10–12) and have many areas with secondary quintuple layers randomly oriented onto the substrate surface in the MBE method (7,10). To facilitate both fundamental physics study and technological applications, it is advantageous to discover a new method to mass-produce clean ultrathin material reliably. Therefore, the electric-field exfoliation method is invented for the purpose.

Layered materials consist of pseudo-two-dimensional sheets weakly bonded by the van der Waals force to form a three-dimensional structure. Ultrathin flakes can, therefore, be exfoliated via the electric field if the exfoliation energy is matched with the interlayer binding energy. The exfoliation energy is nearly equivalent, about a factor of 1.18, to the cleavage energy that use to break the van der Waals interactions and thus separate a

crystalline layer along the basal plane. The exfoliation energy used is linearly proportional to the square of the electric field, thus the exfoliation energy is controllable.

In this work, we demonstrated the electric-field exfoliation method to exfoliate nanoscale-sized of Bi_2Se_3 flakes from the as-grown bulk crystal and directly deposited onto the desired substrate. We further extend the method to graphene, demonstrating that it can be generalized to layered crystalline materials. The simple and effective method of obtaining clean ultrathin material from the as-grown layered bulk crystals is assembled from a simple apparatus as schematically illustrated in Fig. 1.
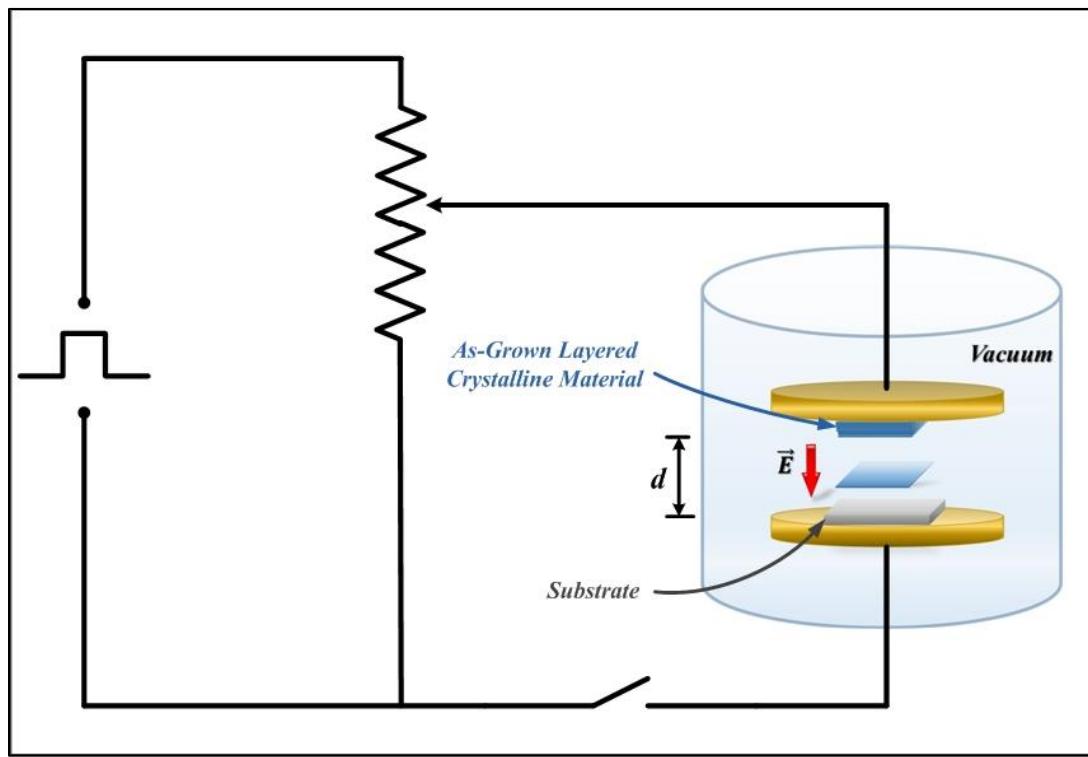
Figure 1. The experimental setup for the electric-field exfoliation (EFX) method to exfoliate the nanolayered crystalline materials from the bulk crystals. A second DC pulse ranging from 50 V to 300 V was applied across the air-gap capacitor plates during the exfoliation process.

RESULTS AND DISCUSSION

Bi$_2$Se$_3$ has a layered hexagonal structure as shown in the inset of Fig. 2. The unit cell consists of three Se-Bi-Se-Bi-Se quintuple layers and each quintuple layer is separated by 2.5 Å van der Waals gaps. The crystal typically cleaves between the weakly couple neighboring Se layers. From the density-functional total energy calculations on Bi$_2$Se$_3$, the result indicates that the basal plane cleavage energy of an ideal single quintuple layer per unit area is $\epsilon_{QL} = 0.40$ J/m^2. For a desired 1µm^2 surface area of the flake, 4×10^{-11} J of total cleavage energy E_{QL} is needed in order to separate it from the as-grown bulk layered crystal. Fig. 2 shows the calculated cleavage energy and its corresponded cleavage stress as a function of cleavage separation in (0001) Bi$_2$Se$_3$. The cleavage stress is the derivative of the cleavage energy.
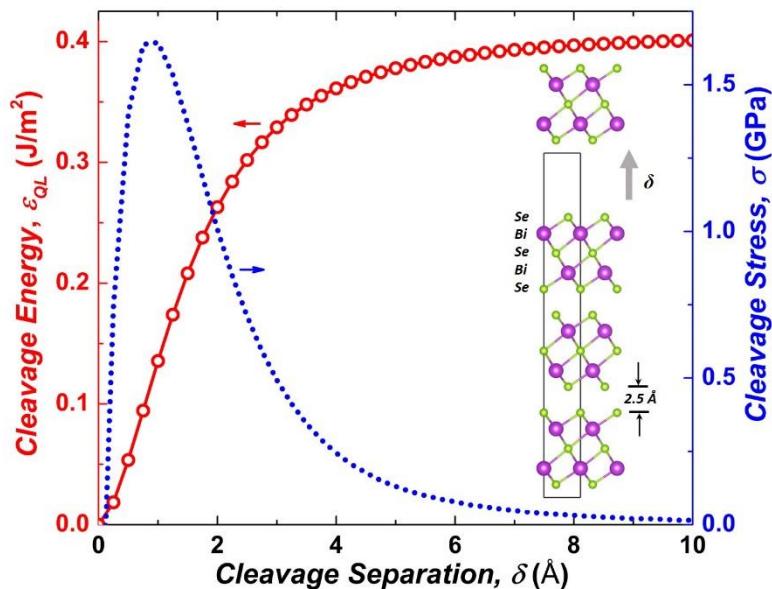
Figure 2. Calculated cleavage energy (circles, solid line) and cleavage stress (dotted line) as a function of cleavage separation in (0001) Bi$_2$Se$_3$. The inset illustrates the size view of the Se-Bi-Se-Bi-Se quintuple layer Bi$_2$Se$_3$ model structure. Each quintuple layers are separated by 2.5 Å van der Waals gaps.

The electric field magnitude can be tuned through the simple relation of $E = V/d$ where V is the applied voltage across the plates and d is the plate spacing. Therefore, the energy density of the electric field can be expressed as $\eta = \frac{1}{2}\varepsilon_o E^2 = \frac{\varepsilon_o V^2}{2d^2}$. Due to the total energy of the field, E_n can be determined from the volume of the exfoliation region, which is bounded by the crystal sides, E_n then is equal to $\eta A d = \frac{\varepsilon_o V^2 A}{2d}$ where A is the area of the crystal. As compared to the equation of E_n with the needed E_{QL} to exfoliate a single quintuple layer of Bi_2Se_3, the essential voltage that is require across the plates is 95 V if the plate spacing d is exactly 1mm.

Ultrathin layers of flakes were exfoliated by applying a short DC pulse in the range of 50 V to few hundred volts across a small air-gap capacitor. The electric field was adjusted to match the binding energy of the crystalline layer determined through the computational calculations above. The region of interest for resulting nanocrystallite structures was then identified with an optical microscope before visualizing by an atomic force microscope (AFM) to determine the topography and height of the exfoliated flakes. All procedures are performed under the standard laboratory environment. More details of the electric-field exfoliation method are described below. Fig. 3 (a) shows the AFM micrograph for Bi_2Se_3 flakes that obtained by this method with 100 V of applied voltage. The results of this procedure were atomically flat freestanding thin flakes. Many of the Bi_2Se_3 flakes were found to have deposited in nanoribbon structures along with the thin flakes prevalent around the region of interest on the glass substrate. Within experimental resolution, the length of the nanoribbon structure flake shows in Fig. 3 (a) is over 13 µm with the surface area exceeding 13 µm². In general, the thicknesses of the flakes ranging from 3 nm to 600 nm depend on the parameters used during the exfoliation. The AB-line

scan profile is shown in Fig. 3 (c). The thickness of flakes is increasing as the electric field increases. However, the flatness of the flake is invariant with respect to the electric field. The flatness of the samples was determined using the roughness parameter R_a defined as $R_a = \frac{1}{n}\sum_{i=1}^{n}|y_i|$ where y_i is the deviation of the ith data point on the surface from the average height. Flakes deposited using the electric field were found to be significantly flatter than those deposited through other methods, such as mechanical exfoliation using adhesives. Nanoscale thickness of Bi_2Se_3 flakes are also observed with the used of Si wafer as a substrate. It is implied that the mechanism of the exfoliation is nearly insensitive to the dielectric constant of the substrates. For applications, the desired substrates can be directly placed into the exfoliator to avoid the tedious transferring process that is typically involved when studying these materials (13–17).

We further demonstrate the use of this method with the fabrication of nanocrystalline structures from graphene. An AFM micrograph and its line scan profile for graphene with a thickness of 0.61 nm are presented in Fig. 3 (b) and (d), respectively. The image reveals that the edges of the graphene flake are thicker as compares to the interior and there are few tiny thick flakes stacked on the graphene. The resulting flakes of graphene are distinctly different from other existing methods. For example, in mechanical exfoliation method, e.g., Scotch tape, the graphene is not in the freestanding crystal structure, but instead, have few-layer graphene to compose the flake. Due to the surface areas of the used highly ordered pyrolytic graphic (HOPG) are small and the cleavage energy of graphene is 0.36 J/m^2, which is lower than Bi_2Se_3 and therefore 50 V of essential voltage is applied for fabricating the graphene instead of 100 V for Bi_2Se_3. All of the layered materials possess a different interlayered binding energy that causes the

determination of the correct electric field become a challenging task. The correct electric field is essential and without it, no ultrathin crystal is obtained.
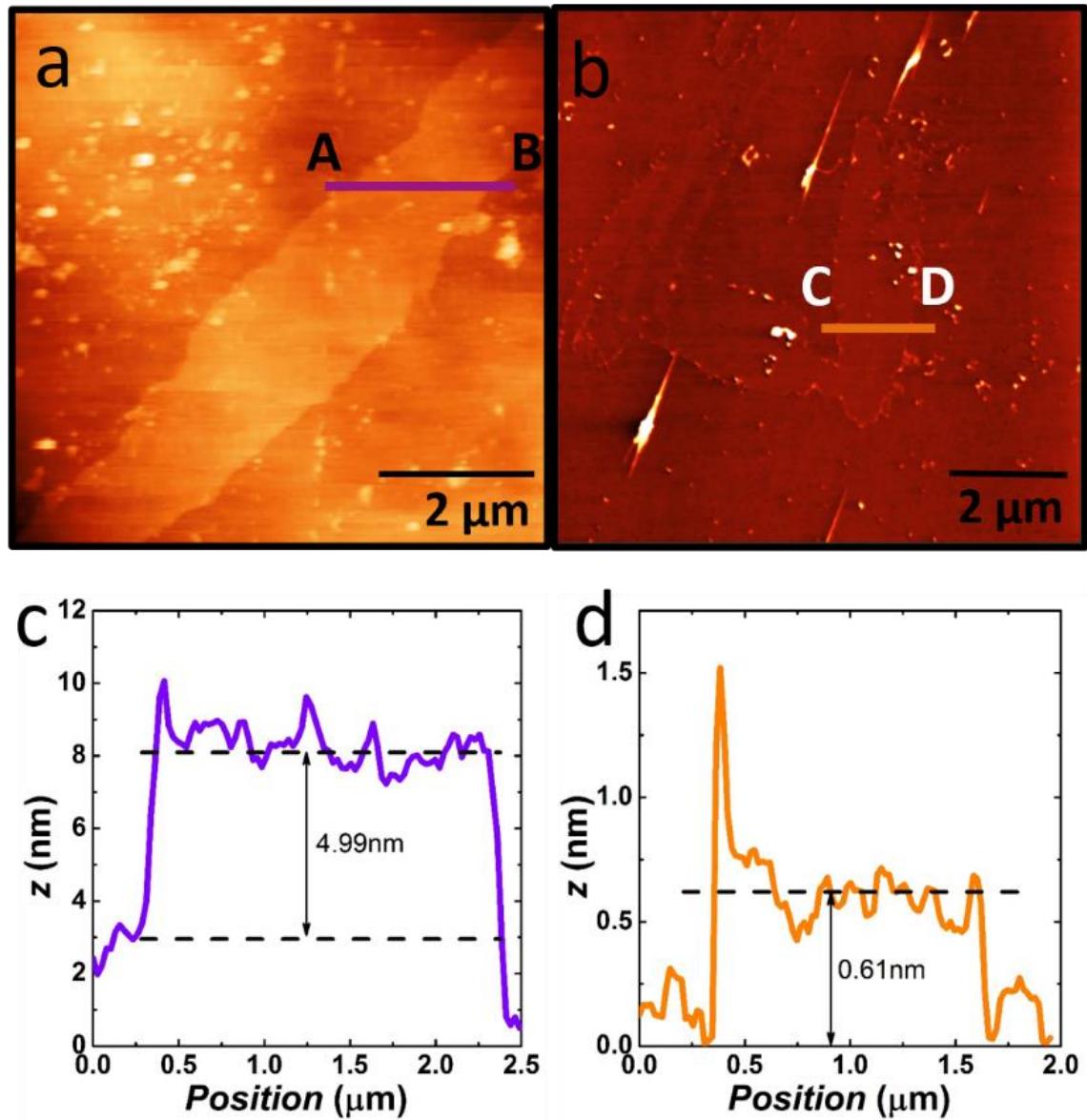
Figure 3. AFM micrographs of (a) Bi_2Se_3 nanoribbon exfoliated onto glass with 100 V of applied voltage. (b) graphene that exfoliated onto the Si substrate. (c) From the AB-line scan of the post-processing micrograph, the thickness of the Bi_2Se_3 nanoribbon is found to be 4.99 ± 0.50 nm. (d) The thickness of the graphene flake indicates in panel (b) is 0.61 nm.

CONCLUSION

Electric field exfoliation is a simple and effective method to fabricate clean two-dimensional samples of layered materials from the bulk crystals. The method is nearly insensitive to the dielectric constant of the used substrates and by a proper tuning of the electric field resulted in thin atomically flat freestanding crystals for most tested layered materials. Moreover, the nanostructure of flakes that were directly deposited on the desired substrate is free from chemical or adhesive residue, providing a clean sample to study the novel physics phenomena that abundant in two-dimensional quantum systems.

MATERIALS AND METHODS

Bulk bismuth selenide (Bi_2Se_3) was synthesized by the modified-Bridgman method. Commercial highly ordered pyrolytic graphic (HOPG) was used in this study. The resulting ingots were broken up into small crystals along the basal plane. The high quality layered geometry of crystalline materials allows the manual separation of crystals into thin layers ranging from 0.2 mm to 0.5 mm and could then be cut into small flakes with a surface area smaller than 1 mm^2. The crystals adhered with a conducting silver paste to one of the brass plates in a custom-built capacitor. An atomically flat substrate, such as silicon wafer, was then adhered to the other capacitor plate. The plate spacing, d was adjusted to 1 mm. The capacitor assembly was then placed in a vacuum chamber with the pressure in the range of microTorr. A regulated voltage source was connected to the capacitor and a short DC pulse ranging from 50 V to 300 V was applied across the plates. A diagram of the apparatus used and its setup is illustrated in Fig. 1. The topography and height of the exfoliated flakes were characterized by tapping mode atomic force microscopy under ambient condition.

Density-functional total energy calculations were performed using Vienna *ab* initio simulation package (VASP) (18,19) employing the generalized gradient approximation in the Perdew-Burke-Ernerhof (GGAPBE) form (20) and the projector augment wave method (21,22) to determine the cleavage energy and cleavage stress in (0001) Bi_2Se_3. A dispersion correction of the total energy (DFT-D3 method) (23) was used to simulate the long-range van der Waals interaction. A plane-wave energy cut-off of 500eV was used. The Brillouin zone was sampled with a mesh of $8 \times 8 \times 4$ k-points, centered at Γ point. The same calculation is also performed on graphene and it is found that 0.36 J/m^2 of cleavage energy is needed, which is in agreement with the literature (24). The structure of Bi_2Se_3 was plotted using VESTA (25).

ACKNOWLEDGEMENTS

AUTHOR CONTRIBUTIONS

ACM and SHL made an equal contribution to the study. YSH conceived and directed the project from conception to production. ACM and SHL constructed the electric-field exfoliation system. SHL performed the bulk single crystal growth of Bi_2Se_3. SHL, EWB, and ACM conducted the AFM measurements. JEM carried out the computational studies. All authors contributed to the writing of the manuscript. The process described in this work will be deposited for patent application.

REFERENCES

1. Novoselov, K. S. *et al.* Electric field effect in atomically thin carbon films. *Science* **306,** 666 (2004).

2. Geim, A. K. & Novoselov, K. S. The rise of graphene. *Nat. Mater.* **6,** 183 (2007).

3. Ugeda, M. M. *et al.* Characterization of collective ground states in single-layer NbSe$_2$. *Nat. Phys.* **12,** 92 (2016).

4. Huang, C. *et al.* Lateral heterojunctions within monolayer MoSe$_2$–WSe$_2$ semiconductors. *Nat. Mater.* **13,** 1096 (2014).

5. Chang, C.-Z. *et al.* High-precision realization of robust quantum anomalous Hall state in a hard ferromagnetic topological insulator. *Nat. Mater.* **14,** 473 (2015).

6. Chang, C.-Z. *et al.* Experimental observation of the quantum anomalous Hall effect in a magnetic topological insulator. *Science* **340,** 167 (2013).

7. Novoselov, K. S. *et al.* Two-dimensional atomic crystals. *Proc. Natl. Acad. Sci. U. S. A.* **102,** 10451–3 (2005).

8. Zhang, G. *et al.* Quintuple-layer epitaxy of thin films of topological insulator quintuple-layer epitaxy of thin films of topological insulator Bi$_2$Se$_3$. *Appl. Phys. Lett* **95,** 53114 (2009).

9. Yu, Y., Sun, W.-T., Hu, Z.-D., Chen, Q. & Peng, L.-M. Oriented Bi$_2$Se$_3$ nanoribbons film: Structure, growth, and photoelectric properties. *Mater. Chem. Phys.* **124,** 865 (2010).

10. Cho, S., Butch, N. P., Paglione, J. & Fuhrer, M. S. Insulating behavior in ultrathin bismuth selenide field effect transistors. *Nano Lett* **11,** 1925 (2011).

11. He, L. *et al.* Epitaxial growth of Bi$_2$Se$_3$ topological insulator thin films on Si (111). *J. Appl. Phys* **109,** 103702 (2011).

12. Min, Y. *et al.* Quick, Controlled synthesis of ultrathin Bi$_2$Se$_3$ nanodiscs and nanosheets. *J. Am. Chem. Soc.* **134,** 2872 (2012).

13. Meitl, M. A. *et al.* Transfer printing by kinetic control of adhesion to an elastomeric stamp. *Nat. Mater.* **5,** 33 (2006).

14. Reina, A. *et al.* Transferring and identification of single- and few-layer Graphene on arbitrary substrates. *J. Phys. Chem. C* **112,** 17741 (2008).

15. Song, L., Ci, L., Gao, W. & Ajayan, P. M. Transfer printing of graphene using gold film. *ACS Nano* **3,** 1353 (2009).

16.   Smythe, E. J., Dickey, M. D., Whitesides, G. M. & Capasso, F. A technique to transfer metallic nanoscale patterns to small and non-planar surfaces. *ACS Nano* **3,** 59 (2009).

17.   Schneider, G. F., Calado, V. E., Zandbergen, H., Vandersypen, L. M. K. & Dekker, C. Wedging transfer of nanostructures. *Nano Lett.* **10,** 1912 (2010).

18.   Kresse, G. & Furthmüller, J. Efficiency of ab-initio total energy calculations for metals and semiconductors using a plane-wave basis set. *Comput. Mater. Sci.* **6,** 15 (1996).

19.   Kresse, G. & Furthmü, J. Efficient iterative schemes for ab initio total-energy calculations using a plane-wave basis set. *Phys. Rev. B* **54,** 11169 (1996).

20.   Perdew, J. P., Burke, K. & Ernzerhof, M. Generalized gradient approximation made simple. *Phys. Rev. Lett.* **77,** 3865 (1996).

21.   Blöchl, P. E. Projector augmented-wave method. *Phys. Rev. B* **50,** 17953 (1994).

22.   Kresse, G. & Joubert, D. From ultrasoft pseudopotentials to the projector augmented-wave method. *Phys. Rev. B* **59,** 1758 (1999).

23.   Grimme, S. Semiempirical GGA-type density functional constructed with a long-range dispersion correction. *J. Comput. Chem.* **27,** 1787 (2006).

24.   Wang, W. *et al.* Measurement of the cleavage energy of graphite. *Nat. Commun.* **6,** 7853 (2015).

25.   Momma, K. *et al. VESTA 3* for three-dimensional visualization of crystal, volumetric and morphology data. *J. Appl. Crystallogr.* **44,** 1272 (2011).

SECTION

5. CONCLUSIONS AND OUTLOOK

In this dissertation, the magnetism of Bi_2Se_3 topological insulator (TI) with various transition metals intercalated into the van der Waals gaps as well as the Dirac surface state have been studied. The intercalation of transition metals not only successfully alters the magnetism of the host system from diamagnetism to either paramagnetic or ferromagnetic ordered, but also induces superconductivity into the system. The findings of TIs that have coexistence of either magnetism, superconductivity, or both are extremely important to the fundamental physics community as well as future applications of quantum computation and spintronic device, a next-generation electronic component.

In Paper I, antiferromagnetic TI by intercalated Fe atom into the Bi_2Se_3 quintuple layers have been synthesized. The antiferromagnetic transition temperature is ~100 K, which is considered high T_N in the magnetic TI. In addition, it is also a metamagnetic system, where the system can be driven from antiferromagnetism to ferromagnetism by a small external magnetic field at about 400 Oe. We have identified that there is no gap at the Dirac surface state of antiferromagnetic TI from the angle-resolved photoemission spectroscopy (ARPES) measurements. This observation verified the theoretical prediction where the product of the broken time-reversal symmetry (TRS) and the broken translational symmetry is preserved in antiferromagnetic TI and leads to a topological invariant. From the angle and temperature-dependent Shubnikov-de Haas oscillations (SdHO), quantum oscillations in longitudinal magnetoresistance measurements, the Fermis surface is two-dimensional (2D). We further deduced the quantum mobility to $\mu_q = 816$ cm^2/Vs and

a π phase shift for the 2D conduction channels. We inferred that the phase shift π is a direct consequence of Berry's phase associated with the massive Dirac fermions in this Fe-doped Bi_2Se_3. We performed Hall measurement on the materials and the quantum Hall effects are observed. The analyzed data reveals that the origin of the 2D-like electronic transport is from many parallel 2D conduction channels.

In Paper II, we have successfully intercalated Mn atom into Bi_2Se_3 quintuple layers by the modified Bridgman method and paramagnetism is induced. The ARPES measurements confirm that the magnetic TI coexistence with topological surface states without energy gap opening for Mn doping into the Bi_2Se_3 due to the symmetry property of paramagnetism. From the analyzed SdHO in longitudinal magnetoresistance measurements, we found that the quantum mobility of the carriers and the phase shift in $Mn_xBi_2Se_3$ are 750 cm^2/Vs and 1.2π, respectively. The phase shift near π reveals the existence of Dirac fermions in this system. However, the observation of the thickness dependent quantum Hall effect suggests that each quintuple layer of $Mn_xBi_2Se_3$ acts as 2D conduction channels.

The intercalation of transition metals into the host TI successfully induced magnetism and superconductivity. In Paper III, we experimentally demonstrated that intercalation of Nb in Bi_2Se_3 TI can turn the TI into an exotic bulk type-II superconductor with a critical temperature of $T_c = 3.2$K while the Dirac surface dispersion in its normal state is still preserved. From the DC susceptibility measurement, Nb-ions are in fact paramagnetic above Tc with the effective moment of 1.26 μ_B/Nb. This paramagnetic behavior was confirmed by *ab-initio* calculations. As compared with Cu-doped Bi_2Se_3, a candidate of topological superconductor, the $Cu_xBi_2Se_3$ system remains diamagnetic at all

temperatures. The onset of remnant or hysteretic magnetization in magnetization measurement of $Nb_xBi_2Se_3$ below T_c also suggests spontaneous time-reversal symmetry breaking in the superconducting state. It is possible that the superconductivity could be of p-wave type, or contains other chiral quasiparticles.

Since the origin of the quantum Hall effect in the $Fe_xBi_2Se_3$ and $Mn_xBi_2Se_3$ systems is from the bulk acting as many 2D conduction channels, the idea of utilizing electric-fields to exfoliate nanostructure flakes from the bulk layered crystalline materials is implemented and presented in Paper IV. This simple and effective method to obtain clean ultrathin materials from the as-grown layered bulk crystals is assembled from a simple apparatus. The exfoliator results in atomically flat freestanding thin flakes. This method is capable of obtaining a clean sample from different layered crystalline materials provided that the correct electric-field is applied to match the exfoliation energy with the interlayered binding energy.

Future work in magnetic TIs will continue to focus on fabricating devices from clean, thin-flakes by using the electric-field exfoliation method to study and manipulate the surface transport. We strongly believe that the realization of the integer quantum Hall effect and even the fractional quantum Hall effect are possible by using this approach. Besides the surface transport study, a method to synthesis a strong magnetic TI with high transition temperatures, and a low concentration of magnetic dopant while sustaining the host TI band structure and carrier density is desired. Lots of fascinating phenomena and technological applications can be achieved once the desired magnetic TIs are synthesized.

For Nb-doped Bi_2Se_3, the onset of hysteretic magnetization below T_c suggests spontaneous TRS breaking in the superconducting state. It is possible that the

superconductivity could be of *p*-wave type. The compound of $Nb_xBi_2Se_3$ studied in this dissertation was synthesized by the modified Bridgman method. Due to the refractory, Nb is hard to blend into the melt of Bi_2Se_3, and only part of the resultant ingot has the superconductivity and the magnetism signals. Furthermore, the synthesized crystals are usually about 1 mm^2. In order to verify its *p*-wave type superconductivity, homogeneous and large crystals of $Nb_xBi_2Se_3$ are necessary. This can be done by exploring an alternative growth method to improve the quality of the crystals. Czochralski and the physical vapor transport (PVT) crystal growth system with a higher heating temperature and rotation option may address the refractory issue of Nb and allow it to blend better into the melt of Bi_2Se_3 and grow homogenous, large crystals of $Nb_xBi_2Se_3$.

In addition, the experimental probe is essential to study its onset magnetism in the superconducting state. Muon spin relaxation (μSR), as a highly sensitive, real-space probe is the ideal technique to study the onset of magnetic order and superconductivity in this material. The local nature of the probe will allow us to determine the homogeneity or spatial extent of this coexistence, as well as look for signatures of spontaneous time-reversal symmetry breaking from small ordered moments.

In summary, we have experimentally demonstrated that intercalation of Fe and Mn in Bi_2Se_3 TI can induce antifferomagnetism and paramagnetism, respectively. Shubnikov-de Haas oscillations and the quantum Hall effect are observed in both of the magnetic TIs. However, those observed multilayered quantum Hall effects suggest that the origin of the quantum oscillations are not due to the surface state but rather from each parallel quintuple layers in bulk. Therefore, the electric-field exfoliation method is invented for the purpose of observing integer quantum Hall effect or even fractional quantum Hall

effect from the surface state. On the other hand, superconductivity also can be induced by intercalation of Nb in Bi_2Se_3. In addition to its superconductivity, $Nb_xBi_2Se_3$ also depicts paramagnetism. Not only do the magnetism and superconductivity coexist, but they also mutually assist each other to give rise to a state that could be described as a symbiosis of the two phases. The emergence of the symbiotic state can have an exotic phenomenon and provide novel materials to open a new door for future research.

BIBLIOGRAPHY

[1]   W. Kohn, Rev. Mod. Phys. **71**, S59 (1999).

[2]   M. L. Cohen, Phys. Rev. Lett. **101**, 250001 (2008).

[3]   L. Fu, C. L. Kane, and E. J. Mele, Phys. Rev. Lett. **98**, 106803 (2007).

[4]   X.-L. Qi, T. L. Hughes, and S.-C. Zhang, Phys. Rev. B **78**, 195424 (2008).

[5]   S.-C. Zhang, Physics (College. Park. Md). **1**, 6 (2008).

[6]   J. E. Moore, Nature **464**, 194 (2010).

[7]   M. Z. Hasan and C. L. Kane, Rev. Mod. Phys. **82**, 3045 (2010).

[8]   X.-L. Qi and S.-C. Zhang, Rev. Mod. Phys. **83**, 1057 (2011).

[9]   Y. Ando, J. Phys. Soc. Japan **82**, 102001 (2013).

[10]   D. Hsieh, Y. Xia, D. Qian, L. Wray, J. H. Dil, F. Meier, J. Osterwalder, L. Patthey, J. G. Checkelsky, N. P. Ong, A. V. Fedorov, H. Lin, A. Bansil, D. Grauer, Y. S. Hor, R. J. Cava, and M. Z. Hasan, Nature **460**, 1101 (2009).

[11]   Y. L. Chen, J. G. Analytis, J.-H. Chu, Z. K. Liu, S.-K. Mo, X. L. Qi, H. J. Zhang, D. H. Lu, X. Dai, Z. Fang, S. C. Zhang, I. R. Fisher, Z. Hussain, and Z.-X. Shen, Science **325**, 178 (2009).

[12]   D. Hsieh, Y. Xia, D. Qian, L. Wray, F. Meier, J. H. Dil, J. Osterwalder, L. Patthey, A. V Fedorov, H. Lin, A. Bansil, D. Grauer, Y. S. Hor, R. J. Cava, and M. Z. Hasan, Phys. Rev. Lett. **103**, 146401 (2009).

[13]   S. Kim, M. Ye, K. Kuroda, Y. Yamada, E. E. Krasovskii, E. V. Chulkov, K. Miyamoto, M. Nakatake, T. Okuda, Y. Ueda, K. Shimada, H. Namatame, M. Taniguchi, and A. Kimura, Phys. Rev. Lett. **107**, 56803 (2011).

[14]   P. Roushan, J. Seo, C. V Parker, Y. S. Hor, D. Hsieh, D. Qian, A. Richardella, M. Z. Hasan, R. J. Cava, and A. Yazdani, Nature **460**, 1106 (2009).

[15]   Y. S. Hor, A. Richardella, P. Roushan, Y. Xia, J. G. Checkelsky, A. Yazdani, M. Z. Hasan, N. P. Ong, and R. J. Cava, Phys. Rev. B **79**, 195208 (2009).

[16]   K. Zhao, Y.-F. Lv, S.-H. Ji, X. Ma, X. Chen, and Q.-K. Xue, J. Phys. Condens. Matter **26**, 394003 (2014).

[17]   L. A. Wray, S.-Y. Xu, Y. Xia, D. Hsieh, A. V Fedorov, Y. S. Hor, R. J. Cava, A. Bansil, H. Lin, and M. Zahid Hasan, Nat. Phys. **7**, 32 (2011).

[18] Y. L. Chen, J.-H. Chu, J. G. Analytis, Z. K. Liu, K. Igarashi, H.-H. Kuo, X. L. Qi, S. K. Mo, R. G. Moore, D. H. Lu, M. Hashimoto, T. Sasagawa, S. C. Zhang, I. R. Fisher, Z. Hussain, and Z. X. Shen, Science **329**, 659 (2010).

[19] X.-L. Qi, R. Li, J. Zang, and S.-C. Zhang, Science **323**, 1184 (2009).

[20] T. Yokoyama, Y. Tanaka, and N. Nagaosa, Phys. Rev. B **81**, 121401(R) (2010).

[21] R. Yu, W. Zhang, H.-J. Zhang, S.-C. Zhang, X. Dai, and Z. Fang, Science **329**, 61 (2010).

[22] C.-Z. Chang, J. Zhang, X. Feng, J. Shen, Z. Zhang, M. Guo, K. Li, Y. Ou, P. Wei, L.-L. Wang, Z.-Q. Ji, Y. Feng, S. Ji, X. Chen, J. Jia, X. Dai, Z. Fang, S.-C. Zhang, K. He, Y. Wang, L. Lu, X.-C. Ma, and Q.-K. Xue, Science **340**, 167 (2013).

[23] Y. Okada, C. Dhital, W. Zhou, E. D. Huemiller, H. Lin, S. Basak, A. Bansil, Y.-B. Huang, H. Ding, Z. Wang, S. D. Wilson, and V. Madhavan, Phys. Rev. Lett. **106**, 206805 (2011).

[24] J. Zhang, C.-Z. Chang, P. Tang, Z. Zhang, X. Feng, K. Li, L. Wang, X. Chen, C. Liu, W. Duan, K. He, Q.-K. Xue, X. Ma, and Y. Wang, Science **339**, 1582 (2013).

[25] T. Schlenk, M. Bianchi, M. Koleini, A. Eich, O. Pietzsch, T. O. Wehling, T. Frauenheim, A. Balatsky, J.-L. Mi, B. B. Iversen, J. Wiebe, A. A. Khajetoorians, P. Hofmann, and R. Wiesendanger, Phys. Rev. Lett. **110**, 126804 (2013).

[26] J. Zaanen, Science **323**, 888 (2009).

[27] L. Fu and C. L. Kane, Phys. Rev. Lett. **100**, 96407 (2008).

[28] Y. S. Hor, P. Roushan, H. Beidenkopf, J. Seo, D. Qu, J. G. Checkelsky, L. A. Wray, D. Hsieh, Y. Xia, S.-Y. Xu, D. Qian, M. Z. Hasan, N. P. Ong, A. Yazdani, and R. J. Cava, Phys. Rev. B **81**, 195203 (2010).

[29] R. J. Cava, H. Ji, M. K. Fuccillo, Q. D. Gibson, Y. S. Hor, J. Xiong, N. P. Ong, A. Yazdani, R. J. Cava, M. H. Berntsen, O. Tjernberg, T. Story, J. H. Dil, A. Marcinkova, E. Morosan, Q. Gibson, R. Sankar, F. C. Chou, R. J. Cava, A. Bansil, and M. Z. Hasan, J. Mater. Chem. C **1**, 3176 (2013).

[30] K. v. Klitzing, G. Dorda, and M. Pepper, Phys. Rev. Lett. **45**, 494 (1980).

[31] D. J. Thouless, M. Kohmoto, M. P. Nightingale, and M. den Nijs, Phys. Rev. Lett. **49**, 405 (1982).

[32] R. B. Laughlin, Phys. Rev. B **23**, 5632(R) (1981).

[33] J. E. Avron, R. Seiler, and B. Simon, Phys. Rev. Lett. **51**, 51 (1983).

[34] M. V. Berry, Proc. R. Soc. London A Math. Phys. Eng. Sci. **392**, 45 (1984).

[35] B. Simon, Phys. Rev. Lett. **51**, 2167 (1983).

[36] C. L. Kane and E. J. Mele, Phys. Rev. Lett. **95**, 226801 (2005).

[37] C. L. Kane and E. J. Mele, Phys. Rev. Lett. **95**, 146802 (2005).

[38] B. A. Bernevig and S.-C. Zhang, Phys. Rev. Lett. **96**, 106802 (2006).

[39] B. A. Bernevig, T. L. Hughes, and S.-C. Zhang, Science **314**, 1757 (2006).

[40] M. König, S. Wiedmann, C. Brüne, A. Roth, H. Buhmann, L. W. Molenkamp, X. Qi, and S. Zhang, Science **318**, 766 (2007).

[41] M. König, M. Baenninger, A. G. F. Garcia, N. Harjee, B. L. Pruitt, C. Ames, P. Leubner, C. Brüne, H. Buhmann, L. W. Molenkamp, and D. Goldhaber-Gordon, Phys. Rev. X **3**, 21003 (2013).

[42] J. E. Moore and L. Balents, Phys. Rev. B **75**, 121306(R) (2007).

[43] R. Roy, Phys. Rev. B **79**, 195322 (2009).

[44] L. Fu and C. L. Kane, Phys. Rev. B **76**, 45302 (2007).

[45] D. Hsieh, D. Qian, L. Wray, Y. Xia, Y. S. Hor, R. J. Cava, and M. Z. Hasan, Nature **452**, 970 (2008).

[46] H. Zhang, C.-X. Liu, X.-L. Qi, X. Dai, Z. Fang, and S.-C. Zhang, Nat. Phys. **5**, 438 (2009).

[47] Y. Xia, D. Qian, D. Hsieh, L. Wray, A. Pal, H. Lin, A. Bansil, D. Grauer, Y. S. Hor, R. J. Cava, and M. Z. Hasan, Nat. Phys. **5**, 398 (2009).

[48] Y. Jiang, Y. Wang, M. Chen, Z. Li, C. Song, K. He, L. Wang, X. Chen, X. Ma, and Q.-K. Xue, Phys. Rev. Lett. **108**, 16401 (2012).

[49] C.-L. Song, Y.-P. Jiang, Y.-L. Wang, Z. Li, L. Wang, K. He, X. Chen, X.-C. Ma, and Q.-K. Xue, Phys. Rev. B **86**, 45441 (2012).

[50] J.-M. Zhang, W. Zhu, Y. Zhang, D. Xiao, and Y. Yao, Phys. Rev. Lett. **109**, 266405 (2012).

[51] C.-Z. Chang, W. Zhao, D. Y. Kim, H. Zhang, B. A. Assaf, D. Heiman, S.-C. Zhang, C. Liu, M. H. W. Chan, and J. S. Moodera, Nat. Mater. **14**, 473 (2015).

[52] C.-Z. Chang and M. Li, J. Phys. Condens. Matter **28**, 123002 (2016).

[53] X. Kou, S.-T. Guo, Y. Fan, L. Pan, M. Lang, Y. Jiang, Q. Shao, T. Nie, K. Murata, J. Tang, Y. Wang, L. He, T.-K. Lee, W.-L. Lee, and K. L. Wang, Phys. Rev. Lett. **113**, 137201 (2014).

[54] J. G. Checkelsky, R. Yoshimi, A. Tsukazaki, K. S. Takahashi, Y. Kozuka, J. Falson, M. Kawasaki, and Y. Tokura, Nat. Phys. **10**, 731 (2014).

[55] G. Xu, J. Wang, C. Felser, X.-L. Qi, and S.-C. Zhang, Nano Lett. **15**, 2019 (2015).

[56] A. Stern and N. H. Lindner, Science **339**, 1179 (2013).

[57] E. Majorana, Nuovo Cim. **14**, 171 (1937).

[58] Y. S. Hor, A. J. Williams, J. G. Checkelsky, P. Roushan, J. Seo, Q. Xu, H. W. Zandbergen, A. Yazdani, N. P. Ong, and R. J. Cava, Phys. Rev. Lett. **104**, 57001 (2010).

[59] D. Shoenberg, *Magnetic Oscillations in Metals* (Cambridge University Press, 1984).

[60] D.-X. Qu, Y. S. Hor, J. Xiong, R. J. Cava, and N. P. Ong, Science **329**, 821 (2010).

[61] J. G. Analytis, R. D. McDonald, S. C. Riggs, J.-H. Chu, G. S. Boebinger, and I. R. Fisher, Nat. Phys. **6**, 960 (2010).

[62] Z. Ren, A. A. Taskin, S. Sasaki, K. Segawa, and Y. Ando, Phys. Rev. B **82**, 241306 (2010).

[63] A. A. Taskin, Z. Ren, S. Sasaki, K. Segawa, and Y. Ando, Phys. Rev. Lett. **107**, 16801 (2011).

[64] A. A. Taskin, S. Sasaki, K. Segawa, and Y. Ando, Phys. Rev. Lett. **109**, 66803 (2012).

[65] J. Xiong, Y. Luo, Y. Khoo, S. Jia, R. J. Cava, and N. P. Ong, Phys. Rev. B **86**, 45314 (2012).

[66] H. Cao, J. Tian, I. Miotkowski, T. Shen, J. Hu, S. Qiao, and Y. P. Chen, Phys. Rev. Lett. **108**, 216803 (2012).

[67] G. P. Mikitik and Y. V. Sharlai, Phys. Rev. Lett. **82**, 2147 (1999).

[68] J. Xiong, A. C. Petersen, D. Qu, Y. S. Hor, R. J. Cava, and N. P. Ong, Phys. E **44**, 917 (2012).

[69] Z. Ren, A. A. Taskin, S. Sasaki, K. Segawa, and Y. Ando, Phys. Rev. B **85**, 155301 (2012).

[70] Y. Yan, L.-X. Wang, X. Ke, G. Van Tendeloo, X.-S. Wu, D.-P. Yu, and Z.-M. Liao, Sci. Rep. **4**, 3817 (2014).

[71] L. Fang, Y. Jia, D. J. Miller, M. L. Latimer, Z. L. Xiao, U. Welp, G. W. Crabtree, and W.-K. Kwok, Nano Lett. **12**, 6164 (2012).

[72] T.-C. Hsiung, D.-Y. Chen, L. Zhao, Y.-H. Lin, C.-Y. Mou, T.-K. Lee, M.-K. Wu, and Y.-Y. Chen, Appl. Phys. Lett. **103**, 163111 (2013).

[73] E. H. Hall, Source Am. J. Math. **2**, 287 (1879).

[74] E. H. Hall, Philos. Mag. Ser. 5 **12**, 157 (1881).

[75] N. Nagaosa, J. Sinova, S. Onoda, A. H. MacDonald, and N. P. Ong, Rev. Mod. Phys. **82**, 1539 (2010).

[76] R. E. Prange and S. M. Girvin, *The Quantum Hall Effect* (Springer New York, New York, NY, 1990).

[77] M. Onoda and N. Nagaosa, Phys. Rev. Lett. **90**, 206601 (2003).

[78] C.-X. Liu, X.-L. Qi, X. Dai, Z. Fang, and S.-C. Zhang, Phys. Rev. Lett. **101**, 146802 (2008).

[79] A. A. Taskin, S. Sasaki, K. Segawa, and Y. Ando, Adv. Mater. **24**, 5581 (2012).

[80] A. Koma, J. Cryst. Growth **201**, 236 (1999).

[81] X. Chen, X.-C. Ma, K. He, J.-F. Jia, and Q.-K. Xue, Adv. Mater. **23**, 1162 (2011).

[82] J. Zhang, C.-Z. Chang, Z. Zhang, J. Wen, X. Feng, K. Li, M. Liu, K. He, L. Wang, X. Chen, Q.-K. Xue, X. Ma, and Y. Wang, Nat. Commun. **2**, 574 (2011).

[83] H. Köhler and A. Fabbicius, Phys. Status Solidi **71**, 487 (1975).

VITA

Seng Huat Lee was born in Johor Bahru, Malaysia. In August 2008, he received his Bachelor of Science (B. S.) with Honors in Applied Physics from the Faculty of Science at University of Malaya, Malaysia. After graduated from the Bachelor degree, he worked as a research assistant in the Plasma Technology Research Center, University of Malaya, Malaysia. In August 2012, he received his Master of Science (M. S.) in Plasma Physics from the Faculty of Science at University of Malaya, Malaysia. During his Master degree program, he received a fellowship and a research grant from the University of Malaya to support his research.

In 2011, he joined the group of Dr. Yew San Hor at the Missouri University of Science and Technology (Missouri S&T) to work on the projects of topological insulators. In December 2017, he received his Ph.D. in Physics from Missouri S&T. During his Ph.D. career, he published three peer-reviewed journal papers and received three times of the graduate teaching award from Physics Department, Missouri S&T to honor the outstanding accomplishments. Based on his research, he also received travel grants from the Missouri S&T.